

UNIVERSITY OF BIRMINGHAM

INVESTIGATING THE EFFICACY OF A NOVEL MICROFLUIDICS-BASED BIOPRINTING SYSTEM TO CONSTRUCT BLOOD VESSEL MIMICS FOR TISSUE ENGINEERING

By Nazia Zeb

A thesis submitted to the University of Birmingham for the degree of

MSc by Research in Dentistry

School of Dentistry

College of Medical and Dental Sciences

University of Birmingham

April 2024

UNIVERSITY OF
BIRMINGHAM

University of Birmingham Research Archive

e-theses repository

This unpublished thesis/dissertation is copyright of the author and/or third parties. The intellectual property rights of the author or third parties in respect of this work are as defined by The Copyright Designs and Patents Act 1988 or as modified by any successor legislation.

Any use made of information contained in this thesis/dissertation must be in accordance with that legislation and must be properly acknowledged. Further distribution or reproduction in any format is prohibited without the permission of the copyright holder.

Abstract

The shortage of bone tissue donors despite the rising cases of bone fracture incidences, as well as complications with current transplant methods, has spurred intense research into tissue engineering as a promising alternative. However, existing tissue engineering strategies face critical limitations, especially in supplying physiologically relevant levels of oxygen and nutrients to cells within the bone tissue scaffolds. To address this issue, a novel microfluidics-based chip for 3D-printing vascular structures was developed. The purpose of this research project was to investigate the efficacy of this novel microfluidic-based chip for fabricating hollow cell-compatible fibres, which are structurally adjustable, durable and can be perfused to mimic physiological blood flow for tissue engineering purposes.

The range of hollow core-shell fibres that can be generated with a defined width and geometry by changing the extrusion flow rates of core solutions, between 125-2000 $\mu l.min^{-1}$, was demonstrated. Straight, wavy and helical core shapes were generated that have the potential to be used for recapitulating different flow rates found physiologically.

To optimise the printing conditions and materials for cell biocompatibility - cytotoxicity, cell adhesion and cell morphology were assessed. This revealed that 10 wt% (100 mg/ml) calcium chloride bath solution provides optimal cell viability as well as structural integrity of the 2 wt% (20 mg/ml) alginate fibres. Gelatine blended with alginate at 1:1 concentration supported cell adhesion while ensuring core-shell fibres could be formed. However, with the optimisation of printing conditions, such as

temperature regulation, gelatine with higher concentrations can be used for enhancing cell adhesion.

Furthermore, the impact of the extrusion method, material composition and prolonged culture on viability of cells encapsulated in fibres with different structures, alongside the influence of storage and incubation conditions on fibre degradation and morphology was evaluated. The results demonstrated that fibres degrade over time when cultured in cell culture media for 28 days at 37 °C. This suggested the optimisation of shell material to improve the mechanical stability of fibres in culture is needed for future studies.

Finally, the hollow core-shell fibres were perfused using gravity and cannulation to confirm the structural integrity and uniformity of the fibre's core for replicating blood flow. The cannulation method and loading of fibres in channels to create a set-up that can potentially be used for generating vascularised bone tissue were explored.

From this project, it can be concluded that, although the materials used for fabricating the fibre need optimisation, the novel microfluidic chip has shown great potential to create a variety of core-shell fibres to mimic human blood vessels for vascularised bone tissue engineering.

To my parents

Acknowledgements

Foremost I would like to thank my supervisors, Dr. Gowsihan Poologasundarampillai and Dr. Amirpasha Moetazedian for all their valuable guidance, support, and patience throughout my undergraduate and postgraduate projects. I am equally thankful to Dr. Malgorzata Wiench and Dr. Samuel Moxon, whose guidance has been instrumental during my master's project. My supervisors' encouragement, constructive feedback, and commitment to excellence have helped me broaden my perspective and refine my research skills.

I would like to show my appreciation to Frankie Lewns, Sandeep Shirgill (for helping me with the Fiji macro), Louise Longhurst and Dunia Khalil for their support during my project. My heartfelt gratitude to all my colleagues at the School of Dentistry, for their help, multiple coffee runs, fun lab events and for constantly reminding me that science is as much about resilience as it is about results. Here's to my lab mates who made my master's journey bearable and fun. May our pipettes never break, our results always be statistically significant, and our laughter never cease.

I am truly grateful to my family for their comfort, encouragement, and love. Particularly my parents, for their sacrifices and guidance which have been the cornerstone of my journey, shaping me into the person I am today.

Finally, but most importantly, I am deeply grateful to Allah, the Most Merciful, All-Knowing and Wise, for the gift of intellect and providing me with the opportunities to utilise my knowledge and skills to make a positive impact on the world around me. *Alhamdulillah* (All praise be to Allah) for His countless blessings and for the journey that lies ahead.

List of conference contributions

1. **Zeb N**, Moetazedian A, Moxon S, Wiench M.1, Cox L, Grover L, Poologasundarampillai G. Investigating the efficacy of a novel bioprinting system, using microfluidic devices, to construct vascularised bone tissue. UKSB Conference, Ulster University, Belfast. 2023 (**Poster**).

2. **Zeb N**, Moetazedian A, Moxon S, Wiench M.1, Cox L, Grover L, Poologasundarampillai G. 3D-printed blood vessel models. Research Poster Competition, University of Birmingham, Birmingham. 2023 (**Poster**).

3. **Zeb N**, Moetazedian A, Moxon S, Wiench M.1, Cox L, Grover L, Poologasundarampillai G. A novel bioprinting system for constructing blood vessel mimics with the potential for reducing animal use in research. Midlands 3Rs Symposium, NC3Rs, University of Birmingham, Birmingham. 2023 (**Poster & oral presentation**).

Table of Contents

ABSTRACT II

ACKNOWLEDGEMENTS V

LIST OF CONFERENCE CONTRIBUTIONS VI

LIST OF TABLES XI

LIST OF FIGURES XII

LIST OF ABBREVIATIONS XXII

1. INTRODUCTION 1

1.1. Research background and significance 2

1.2. Bone tissue 2
- **1.2.1. Types of bones** 3
- **1.2.2. Layers of bone tissue** 4
- **1.2.3. Composition of the bone matrix** 7
- **1.2.4. Cellular components of bone** 8
- **1.2.5. Current bone transplantation strategies** 8
- **1.2.6. Bone replacement using tissue engineering** 9
- **1.2.7. A current challenge in bone tissue engineering** 10
- **1.2.8. Vascularised bone tissue** 11

1.3. Vasculature: an unmet need 12
- **1.3.1. Vessel formation** 13
- **1.3.2. Angiogenesis** 13
- **1.3.3. Role of oxygen levels in vessel formation** 14
- **1.3.4. Types of blood vessels** 15
- **1.3.5. Structure of blood vessels** 16
- **1.3.6. Endothelial barrier formation** 19
- **1.3.7. Biochemical gradients** 19
- **1.3.8. Types of flow in the blood vasculature** 20
- **1.3.9. Current 3D artificial blood vessels** 21

1.4. Additive manufacturing 23
- **1.4.1. Types of additive manufacturing** 24
- **1.4.2. Material extrusion additive manufacturing** 25
- **1.4.3. Scaffold material** 26

1.4.4. Microfluidics-based devices for 3D bioprinting of blood vessel mimics 27
1.4.5. Coaxial printing 27
1.4.6. A novel microfluidic-based 3D-printing system 29

1.5. Summary **32**

1.6. Aim and objectives **33**

2. MATERIALS AND METHODS **35**

2.1. Materials **36**

2.2. Methods **37**
2.2.1. Preparation of solutions to generate and perfuse fibres 37
2.2.2. Production of core-shell alginate fibres 39
2.2.2.1. Extrusion of core-shell fibres 39
2.2.2.2. Width measurements 41
2.2.3. Standard tissue culture techniques 43
2.2.3.1. Cells and culture medium 43
2.2.3.2. Cell passage 43
2.2.3.3. Cell count 44
2.2.3.4. Cryopreservation and thawing of cells 45
2.2.4. Effect of bath $CaCl_2$ concentration on cell viability 46
2.2.4.1. Fibre production 46
2.2.4.2. Live/Dead assay 47
2.2.4.3. Width measurements 51
2.2.5. Effect of polymer composition on fibre formation - blends with gelatine 52
2.2.5.1. Cell attachment and morphology test 52
2.2.5.2. Viability and morphological analysis 53
2.2.5.3. Extrusion of fibres 55
2.2.5.4. Width measurements 56
2.2.6. Prolonged (28-day) culture and storage of fibres 57
2.2.6.1. Preparation of cell-encapsulated fibres 57
2.2.6.2. Cell-free core-shell alginate fibres for different culture conditions 58
2.2.6.3. Cell viability and morphological analysis of the cell-encapsulated fibres 60
2.2.6.4. Observation of the fibres' stability 60
2.2.6.5. Width measurements of fibres 60
2.2.7. Perfusion of core-shell fibres 61
2.2.8. Statistics 63

3. FABRICATION OF BIOMIMETIC CORE-SHELL FIBRES **64**

3.1. Introduction **65**

3.2. Results **67**
3.2.1. Effect of extrusion flow rate on core-shell alginate fibres' geometry 3.2.1.1. Core-shell alginate fibres with a range of core geometry can be generated 67

3.2.1.2. Extrusion flow rate of core solution impacts the width of fibre's core and shell ... 71
3.2.1.3. Impact of Qshell/Qcore on fibre's Wcore/Wshell and helical pitch ... 75
3.2.2. Testing different concentrations of $CaCl_2$ in bath solution ... 78
3.2.2.1. Fibre width decreases with increasing $CaCl_2$ concentration ... 78
3.2.2.2. Impact of $CaCl_2$ concentration on cell viability and morphology ... 80
3.2.3. Changing the shell's polymer composition to promote cell attachment ... 85
3.2.3.1. Impact of increasing the gelatine concentration on viability, spreading area and amount of cells attached ... 85
3.2.3.2. Impact of increasing the gelatine concentration on fibre's structure ... 92

3.3. Discussion ... **97**
3.3.1. Effect of extrusion flow rate on core-shell alginate fibres' geometry ... 97
3.3.1.1. Printing process ... 97
3.3.1.2. Fibre's structure ... 98
3.3.2. Testing different concentrations of $CaCl_2$ in bath solution ... 103
3.3.2.1. Fibre's structure ... 103
3.3.2.2. Cell viability ... 104
3.3.2.3. Cell morphology ... 105
3.3.3. Changing the shell's polymer composition to promote cellular biocompatibility ... 106
3.3.3.1. Cell viability ... 107
3.3.3.2. Cell attachment ... 108
3.3.3.3. Cell area ... 109
3.3.3.4. Fibre's structure ... 109

3.4. Limitations of the study ... **111**

3.5. Summary ... **114**

4. EFFECT OF PROLONGED CULTURE ON CELL VIABILITY AND FIBRE DEGRADATION ... 115

4.1. Introduction ... **116**

4.2. Results ... **118**
4.2.1. Testing different types of fibres ... 118
4.2.1.1. Viability and morphology of cells embedded in fibres for a 28-Day culture ... 118
4.2.1.2. Effect of culture time on fibres' morphology ... 126
4.2.2. Testing different incubation and storage conditions ... 133
4.2.2.1. Effect of storage conditions on fibre's morphology ... 133
4.2.2.2. Effect of storage conditions on fibre's core and shell ... 139

4.3. Discussion ... **145**
4.3.1. Testing different types of fibres ... 145
4.3.1.1. Cell viability and morphology ... 145
4.3.1.2. Fibre morphology and structure ... 147
4.3.2. Testing different incubation and storage conditions ... 148
4.3.2.1. Fibre morphology and structure ... 149

4.3.2.2. Cause of fibre degradation 150

4.4. Limitations of the study **152**

4.5. Summary **154**

5. PERFUSION OF FIBRES TO MIMIC BLOOD FLOW **155**

5.1. Introduction **156**

5.2. Results **157**
5.2.1. Perfusion test 157
5.2.1.1. Fibres printed using varying extrusion flow rates of core solution 157
5.2.1.2. Fibres printed using varying gelatine concentrations 160
5.2.2. Cannulation and set-up of fibre on a chip 162
5.2.2.1. Cannulation of fibres 162
5.2.2.2. Setting up channels with fibres 163

5.3. Discussion **164**
5.3.1. Perfusion test 164
5.3.1.1. Fibres printed using varying core flow rates 164
5.3.1.2. Fibres printed using varying gelatine concentrations 164
5.3.1.3. Future directions 165
5.3.2. Cannulation and set-up of fibre on a chip 166
5.3.2.1. Cannulation of fibres 167
5.3.2.2. Setting up channels with fibres 168
5.3.2.3. Future directions 168

5.4. Limitations of the study **170**

5.5. Summary **170**

6. CONCLUSIONS **172**

6.1. Major outcomes **173**

6.2. Future work **175**

7. LIST OF REFERENCES **178**

8. APPENDICES **195**

List of Tables

Table 1. 1: Overview of the blood vessel diameter for different sections of the vasculature tree. The diameter of the blood vessel varies depending on the age, sex and exercise level of an individual (76,78–82,84,85). 16

Table 1. 2: Previous work has shown that perfusable hollow fibres can be fabricated with a range of core widths, using different extrusion set-ups. 28

Table 2. 1: Extrusion pump settings used for the syringes when printing core-shell fibres. 39

Table 2. 2: Extrusion flow rates of solutions used for printing core-shell alginate fibres. 41

Table 2. 3: List of $CaCl_2$ bath solutions, in supplemented cell culture media, tested for cell viability. 46

Table 2. 4: List of different compositions of alginate-gelatine blends tested for investigating cell response to the material. 52

Table 2. 5: Different concentrations of gelatine was mixed with sodium alginate to make alginate-gelatine blends. 56

Table 2. 6: Types of cell-encapsulated fibres tested for prolonged 28-day cell culture and the composition of materials that were used for each fibre. 57

Table 2. 7: The composition of incubation medium and temperatures that were used for testing the stability of core-shell alginate fibre over a 28-day period. 59

Table 2. 8: The composition of core-shell alginate fibre for testing its stability over a 28-day period. 59

List of Figures

Figure 1. 1: Types of bones. There are various types of bones in the human body. These include flat, short, irregular, long and sesamoid bone (10–12). Created with BioRender.com. 4

Figure 1. 2: Periosteum and Endosteum. Bone is made up of layers called periosteum and endosteum. Periosteum is the outer layer, composed of fibrous and cellular components, and surrounds the layer called endosteum. Endosteum contains the bone matrix and multiple cells (e.g., osteoclasts, osteocytes, osteogenic cells and osteoblasts) (19). 5

Figure 1. 3: Compact and spongy bone. There are multiple layers of bone, containing various cellular (e.g., osteocytes) and structural (e.g., lamella and lacuna) components. Compact bone is made up of circular units called osteons, which are heavily innervated and vascularised through channels called Haversian canal. Spongy bone tissue makes up the internal structure of the bone and houses the bone marrow (24).....6

Figure 1. 4: Overview of bone tissue engineering. Tissue engineering involves fabricating a scaffold made of a variety of materials, cells and growth factors to induce bone regeneration (48).....10

Figure 1. 5: Angiogenesis process. Sprouting of blood vessels, regulated by growth factors such as VEGF, ensure adequate oxygen is supplied to all cells. In response to low oxygen level (hypoxia) stimulus, ECs sprout towards the area of hypoxia, forming a new branch of blood vessel. Matrix metalloproteinases (MMPs) degrade the basement membrane (BM) allowing the ‘tip cell’ to lead a stalk of ECs towards the hypoxic area (72).....14

Figure 1. 6: Structure and components of blood vessels. This diagram illustrates the different sizes of blood vessels in the human body with different wall structures. Main vessel types include large vessels (arteries and veins), small vessels (arterioles and venules) and capillaries. A range of cells and components provide support to the blood vessels, such as fibroblasts and elastic lamina (76). 17

Figure 1. 7: Vessel wall layers. Blood vessels are made up of three main layers: tunica adventitia, tunica media and tunica intima (91). 19

Figure 1. 8: Additive manufacturing process. A simplified diagram to illustrate the key difference between traditional manufacturing process and additive manufacturing. Traditional manufacturing process involves machining to create a desired product, while creating large waste from raw material. Whereas AM uses

filaments as raw material to precisely create 3D structures with minimum waste (104).....24

Figure 1. 9: Main types of additive manufacturing. The diagram shows the three main types of printing methods used for fabricating tissue mimics in regenerative medicine. These include **a**) laser-assisted, **b**) inkjet and **c**) material extrusion (108). 25

Figure 1. 10: A novel microfluidic-based extrusion device for constructing blood vessel mimics. A) Bioinks are extruded through the microfluidic-based nozzle into a $CaCl_2$ bath, forming helical core-shell fibres. **B**) The chip has the potential to be incorporated with a range of mixer channels for various studies. **C**) Flow focusing **D**) channels allow the extrusion of multiple materials at once. Channel sizes are 400 µm for core and 1000 µm for shell. Figure provided by Moetazedian et al. (2023) (110).31

Figure 2. 1: Printing process of the core-shell fibres using the novel microfluidic chip. The Pluronic solution was extruded from the inner channel of the microfluidic chip, while sodium alginate was extruded from the outer channel, into the bath solution. The samples were imaged using a microscope. Created in BioRender.com. 40

Figure 2. 2: Width and helical pitch measurements of core-shell fibre. Figure shows a core-shell fibre demonstrating how the helical pitch and width (W) measurements for each parameter were taken. 42

Figure 2. 3: Siphoning method to perfuse fibres. The diagram illustrates the set-up for perfusing fibres with blue dye, using the siphoning method. 61

Figure 3. 1: Photographic images of the fibre extrusion process using the novel microfluidic chip. Ai-iii) Timelapse images of the fibre extrusion process. **B)** Image demonstrating that a very long fibre could be printed in one go. Yellow and blue dyes were used for visualisation of the fibres. Scale bar: 5 cm. 69

Figure 3. 2: Photographic images demonstrating fibres with a range of core structures that can be printed by changing the ratio between shell and core extrusion flow rates. A) Keywords to describe the structure of the fibre. Green lines indicate the shell of the fibre and blue lines highlight the core of the hollow hydrogel fibre. **Bi & ii)** Fibres with a straight core. **C)** Wavy core shapes. **D)** Fibres with a range of helical core shapes that are loosely and densely packed inside the fibre. The range of flow rates used for printing these fibres for the shell was kept constant at 2000 $\mu l.min^{-1}$ while the flow rate of core was decreased from 2000-125 $\mu l.min^{-1}$. Scale bar: 500 µm. 71

Figure 3. 3: Photographic images demonstrating the structure of fibres, as seen without a microscope. The demonstrated fibres were extruded using core flow rates of **A)** 2000 µl.min^{-1}, **B)** 1500 µl.min^{-1}, **C)** 1000 µl.min^{-1}, **D)** 500 µl.min^{-1}, **E)** 250 µl.min^{-1}, **F)** 125 µl.min^{-1} with a constant shell flow rate of 2000 µl.min^{-1}. Hollow alginate fibres could be printed with a range of core structures by changing the ratio of extrusion flow rates between shell and core. Specific areas of the fibres were zoomed in (x4) (**A-Fii**) from the original images (**A-Fi**), to clearly show the structure of the core. However, core of the fibres could be observed clearly with the naked eye as well. Scale bar: 5 mm. 72

Figure 3. 4: Changes in the width of shell and core, of the alginate hollow fibre, in response to increase in the extrusion flow rate of core solution. Ai-vi) Phase-contrast images of the extruded core-shell fibres for each core flow rate, while the shell flow rate was kept constant at 2000 µl.min^{-1}. Scale: 500 µm. **B)** As the flow rate of core was increased from 125 µl.min^{-1} - 2000 µl.min^{-1}, shell width gradually decreased from 1345.10 ± 191.17 µm to 1062.07 ± 143.20 µm while the core width increased from 336.83 ± 26.95 µm to 684.14 ± 98.87 µm. Linear regression for core reported Y = 0.1768*X + 322.2. Data is shown as mean ± SD of three independent experiments. N = 3. 74

Figure 3. 5: W_{core}/W_{shell} of hollow alginate hydrogel fibres in response to increase in the extrusion flow rates (Q) ratio of shell and core solutions. The flow rate of the shell was kept constant at 2000 µl.min^{-1} while the flow rate of core decreased from 2000-125 µl.min^{-1}. W_{core}/W_{shell} (thickness of the fibre's wall) decreased from 0.65 ± 0.097 to 0.27 ± 0.05, as the Q_{shell}/Q_{core} (ratio between shell and core flow rate) increased from 1 to 16. Data is shown as mean ± SD of three independent experiments. N = 3. 76

Figure 3. 6: Helical pitch of fibre's core in response to increase in the extrusion flow rates (Q) ratio of shell and core solutions. The flow rate of the shell was kept constant at 2000 µl.min^{-1} while the flow rate of core decreased from 2000-125 µl.min^{-1}. There was no distinct trend in the effect of Q_{shell}/Q_{core} on the helical pitch of fibre's core. Data are shown as mean ± SD of three independent experiments, representative of pooled measurements from multiple samples to account for measurements taken at random locations of each sample. N = ranges between 28 – 76. 77

Figure 3. 7: Impact of $CaCl_2$ concentration on the width of the cell-encapsulated alginate fibres' shell. The extrusion flow rates used for alginate was 2000 µl.min^{-1} through a plastic tube, without the microfluidic chip, into the $CaCl_2$ bath solution at 2, 4 and 10 wt%. The concentration of alginate was kept constant at 2 wt%. **A i-iii**) Phase-contrast images of fibres, visually demonstrating their size in comparison to each other. Scale bar: 500 µm. **B)** A line graph illustrating the relationship between bath $CaCl_2$ concentration and the width of the fibre. Linear regression reported Y = -

19.34*X + 1414. Data are shown as mean ± SD of three independent experiments. N = 3. 79

Figure 3. 8: Effect of bath $CaCl_2$ concentration on the viability of cells encapsulated in alginate fibres. The viability of cells (3T3s) embedded in solid alginate fibres was measured 24 hours after incubation, following bathing in different concentrations of $CaCl_2$ (2, 4 and 10 wt%) in water. The solid fibres without core were extruded at flow rate of 2000 µl.min^{-1}. Raw data were collected as confocal Z-stack images at random locations in the fibre samples, following a Live/Dead assay. **A - C i**) Phase-contrast images of cells encapsulated in alginate fibres. Scale bar: 500 µm. **A - C ii - iv**) Live (green) and dead (red) stained cells, encapsulated in the alginate fibres. Scale bar: 100 µm. **D)** Data are shown as mean ± SD of three independent experiments, representative of pooled measurements. This method was chosen to minimize bias and to get a more reliable p-value (see **section 2.2.4.2.**). A non-parametric one-way ANOVA on skewed data, followed by a multiple comparisons test among test groups 2 wt% (n=28), 4 wt% (n=29) and 10 wt% (n=30) was carried out ($p \leq 0.05$). Statistical analysis revealed significant differences in cell viability amongst the different $CaCl_2$ concentrations ($p < 0.05$). Cell viability was highest for 10 wt% $CaCl_2$ group (86.6 ± 7.072%), followed by 4 wt% $CaCl_2$ (80.61 ± 12.12%), and then 2 wt% group having the least cell viability of all three groups (69.03 ± 11.34%). ** $p \leq 0.01$ and **** $p \leq 0.0001$. Non-significant results ($p > 0.05$) are not labelled on the graph. 82

Figure 3. 9: Impact of different concentrations of $CaCl_2$ in bath solution on cell morphology. The extrusion flow rates used for alginate (2 wt%) was 2000 µl.min^{-1} through a plastic tube, without the microfluidic chip, into the $CaCl_2$ bath solution at 2, 4 and 10 wt%. Live/Dead stain was carried out after 24 hours of culture. Live (green) and dead (red) stained 3T3 cells, are shown encapsulated in the alginate fibres printed in **A)** 2 wt%, **B)** 4 wt% and **C)** 10 wt% $CaCl_2$ bath solution, with a rounded morphology. Scale bar: 100 µm. **D)** The relationship between bath $CaCl_2$ concentration and the mean spreading area of a cell (cell area; µm^2), encapsulated in the alginate fibre, 24 hours after culture is shown. Measurements for samples were collected as fluorescent images at random locations of the fibre samples, following a Live/Dead assay. Data are shown as mean ± SD of three independent experiments, representative of pooled averaged measurements from multiple images of samples (see **section 2.2.4.2.)**. Statistical analysis using a non-parametric one-way ANOVA, on skewed data, followed by a Dunn's multiple comparisons test between test groups revealed no significant differences in spreading area of a cell amongst the different $CaCl_2$ concentrations ($p > 0.05$). N = 9. 84

Figure 3. 10: Phase-contrast and confocal microscopy images of cells cultured on different concentrations of alginate-gelatine blends. Cells (3T3s) were cultured on alginate-gelatine blends composed of different concentrations of gelatine

(0, 2, 6 and 10 wt%) for 24 hours, followed by a Live/Dead staining. **A-E (i)** show light microscope images of cells in each experimental group, 24 hours after culture, to demonstrate cell presence before Live/Dead assay was carried out. **A-E (ii-iv)** show confocal images illustrating cell morphology and numbers in comparison to the Negative control group. Scale bars: 100 μm. 86

Figure 3. 11: Impact of gelatine concentration in the alginate-gelatine blend on cell viability and attachment. 3T3s were seeded on top of alginate-gelatine blends consisting of alginate (2 wt%) with different final concentrations of gelatine (2, 6, and 10 wt%). The test group of 0 wt% was used a positive control with no gelatine added. For Negative control, cells were seeded directly on the cell culture dish. The (**A**) viability (%) and (**B**) the percentage of cells attached to the test material (compared to Negative control; cell attachment (%)) were measured after 24 hours of culture. Measurements for samples were collected as fluorescent images at random locations of the samples, following a Live/Dead assay. Data are shown as mean ± SD of three independent experiments, representative of pooled averaged measurements from multiple images of samples (see **section 2.2.5.2.**). **A**) One-way ANOVA, followed by a Tukey's multiple comparisons test among Negative (n=35), 0 wt% (n=3), 2 wt% (n=21), 6 wt% (n=25) and 10 wt% (n=45), was carried out ($p \leq 0.05$). Alginate-only group (0 wt%) had a cell viability of 0 ± 0% which was expected due to no cells left in the samples (**B**). Cell viability for 2 wt% gelatine group was 4.3% lower compared to Negative control, however, it was not significantly different ($p = 0.5$). Cell viability for 6 wt% gelatine group was significantly lower by 8.82% compared to Negative control ($p = 0.0072$). Cell viability for 10 wt% gelatine group was significantly lower by 7.64% compared to Negative control ($p = 0.0067$). **B**) Statistical analysis using a non-parametric one-way ANOVA, on skewed data, followed by a Dunn's multiple comparisons test among 0 wt% (n=3), 2 wt% (n=23), 6 wt% (n=23) and 10 wt% (n=41) was carried out ($p \leq 0.05$). Only 10 wt% group had a significantly higher number of cells attached compared to 2 wt% group by 150.07% ($p = 0.0357$). No significant difference was observed between 6 wt% and other alginate-gelatine blend groups. There was large variation in data as represented by large error bars. * $p \leq 0.05$, ** $p \leq 0.01$, **** $p \leq 0.0001$. Non-significant results ($p > 0.05$) are not labelled on the graph. wt% on the graphs refer to gelatine concentration in the alginate-gelatine blend. 89

Figure 3. 12: Impact of gelatine concentration in the alginate-gelatine blend on spreading area of cells. 3T3s were seeded on top of alginate-gelatine blends consisting of alginate (2 wt%) with different final concentrations of gelatine (2, 6, and 10 wt%). The test group of 0 wt% was used as a positive control with no gelatine added to alginate. The Negative group refers to negative control where cells were seeded directly on the cell culture dish. The mean spreading area of a cell (cell area; μm^2), seeded on top of these polymer blends was measured after 24 hours of culture. Measurements for samples were collected as fluorescent images at random

locations of the samples, following a Live/Dead assay. Data are shown as mean ± SD of three independent experiments, representative of pooled averaged measurements from multiple images of samples (see **section 2.2.5.2.**). One-way ANOVA with Tukey's multiple comparisons test between Negative (n=9), 0 wt% (n=9), 2 wt% (n=9), 6 wt% (n=9) and 10 wt% (n=7) was carried out ($p \leq 0.05$). Statistical analysis revealed that only 10 wt% group had significantly different spreading area of cells compared to the ones in Negative group by 35.20% ($p = 0.0402$). * $p \leq 0.05$, ** $p \leq 0.01$, **** $p \leq 0.0001$. Non-significant results ($p > 0.05$) are not labelled on the graph. wt% on the graph refers to gelatine concentration in the alginate-gelatine blend. 91

Figure 3. 13: Impact of gelatine concentration on the structure of alginate-gelatine hollow fibres. Core-shell fibres with different concentrations of gelatine were printed. The final concentration of gelatine, 0, 2, 4 and 10 wt%, in the alginate-gelatine blend fibres were tested, while the final concentration of alginate was kept constant at 2 wt%.The extrusion flow rates used for materials in this study were 2000 $\mu l.min^{-1}$ for the shell and 1500 $\mu l.min^{-1}$ for the core, into the 10 wt% $CaCl_2$ bath solution. **Ai – iv)** Phase-contrast images of core-shell fibres' structure. Fibres printed with 10 wt% gelatine (iv) did not have a distinct core. Scale bar: 500 µm. **B)** Relationship between gelatine concentration and the width of shell (green) and core (blue). **C)** Relationship between gelatine concentration and W_{core}/W_{shell} (i.e., fibre's wall thickness). Values are expressed as mean ± SD. n=3. 94

Figure 3. 14: Impact of gelatine concentration on the helical pitch of core-shell fibres' core. Core-shell fibres with different concentrations of gelatine were printed. The final concentration of gelatine, 0, 2, 6 and 10 wt%, in the alginate-gelatine blend fibres were tested, while the final concentration of alginate was kept constant at 2 wt%. The extrusion flow rates used for materials in this study were 2000 $\mu l.min^{-1}$ for the shell and 1500 $\mu l.min^{-1}$ for the core, into the 10 wt% $CaCl_2$ bath solution. Data are shown as mean ± SD of three independent experiments, representative of pooled measurements from multiple samples to account for measurements taken at random locations of each sample. N = ranges between 3 – 71. 96

Figure 4. 1: Confocal microscopy analysis of cells embedded in solid alginate fibres. 3T3s embedded within solid alginate fibres are presented, with each row representing a specific day of culture: Day 1 (i), 7 (ii), 14 (iii), 21 (iv) and 28 (v). Each column displays different confocal imaging channels: **A**) both red and green channels, **B**) green channel (alive cells) only, and **C**) red channel (dead cells) only. The contrast in red channels (**C**) was enhanced by 0.35 saturation using Fiji software. Scale: 100 µm. 120

Figure 4. 2: Confocal microscopy analysis of cells embedded in core-shell alginate fibres. 3T3s embedded within core-shell alginate fibres are presented, with

each row representing a specific day of culture: Day 1 (i), 7 (ii), 14 (iii), 21 (iv) and 28 (v). Each column displays different confocal imaging channels: **A**) both red and green channels, **B**) green channel (alive cells) only, and **C**) red channel (dead cells) only. The contrast in red channels (**C**) was enhanced by 0.35 saturation using Fiji software. Scale: 100 µm. 121

Figure 4. 3: Confocal microscopy analysis of cells embedded in core-shell alginate-gelatine blend fibres. 3T3s embedded within core-shell alginate-gelatine fibres are presented, with each row representing a specific day of culture: Day 1 (i), 7 (ii), 14 (iii), 21 (iv) and 28 (v). Each column displays different confocal imaging channels: A) both red and green channels, B) green channel (alive cells) only, and C) red channel (dead cells) only. The contrast in red channels (C) was enhanced by 0.35 saturation using Fiji software. Scale: 100 µm. 122

Figure 4. 4: The viability of 3T3s embedded in different types of fibres and cultured for 28 days. The types of cell-encapsulated fibres tested were: (**A**) solid and (**B**) core-shell fibres composed of 2 wt% alginate only and (**C**) core-shell fibres made of 2 wt% alginate and 2 wt% gelatine blends. Extrusion flow rates used were 2000 µl.min^{-1} for shell (**A-C**) and 1500 µl.min^{-1} for core (**B-C**). Measurements for samples were collected as confocal Z-stack images at random locations in the sample, following a Live/Dead assay. Data are shown as mean ± SD of one independent experiment, representative of pooled measurements from multiple samples. Statistical analysis using a parametric and non-parametric one-way ANOVA — on normally distributed and skewed data, respectively — followed by a multiple comparisons test between Groups at a specific timepoint (Day) and between Days for each group ($p \leq 0.05$) was carried out. * $p \leq 0.05$ and ** $p \leq 0.01$. Non-significant results ($p > 0.05$) are not labelled on the graph. N = ranges between 3 - 11..... 125

Figure 4. 5: Phase-contrast images of temporal changes in three different types of fibres. The types of cell-encapsulated fibres tested were: (**A**) solid and (**B**) core-shell fibres composed of 2 wt% alginate only and (**C**) core-shell fibre made of 2 wt% alginate and 2 wt% gelatine blends. Fibres were cultured in supplemented DMEM, which was changed regularly. Images represent multiple fibres that were printed specifically for the day the images were taken. Each row within the figure represents a specific day of culture (Day 1, 7, 14, 21 and 28) for all three groups, allowing for a visual comparison of fibre's morphology over time. Extrusion flow rates used were 2000 µl.min^{-1} for shell (**A-C**) and 1500 µl.min^{-1} for core (**B-C**). Scale bar: 500 µm. 127

Figure 4. 6: The width of different fibres' shell is influenced by culture for 28 days. The types of cell-encapsulated fibres tested were: (**A**) solid and (**B**) core-shell fibres composed of 2 wt% alginate only and (**C**) core-shell fibres made of 2 wt% alginate and 2 wt% gelatine blends. Extrusion flow rates used were 2000 µl.min^{-1} for shell (**A-C**) and 1500 µl.min^{-1} for core (**B-C**). Width measurement data for all fibres' shell size are presented in the green graph (**Ai – Ci**) and core size measurements for

core-shell fibres are presented in blue graphs (**Bii and Cii**). Day 0 represents the measurements taken of the fibres' structure on the day it was printed for the corresponding Day bar it is presented with. Data are shown as mean ± SD of one independent experiment, representative of pooled measurements from multiple samples. Statistical analysis using a two-tailed parametric and non-parametric t-test — on normally distributed and skewed data, respectively — between Day 0 and the corresponding day was carried out ($p \leq 0.05$). * $p \leq 0.05$, ** $p \leq 0.01$, *** $p \leq 0.001$, **** $p \leq 0.0001$. Non-significant results ($p > 0.05$) are not labelled on the graph. N = ranges between 3-16 for shell, and 3-13 for core. 130

Figure 4. 7: The W_{core}/W_{shell} of different fibres when cultured for 28 days. The types of cell-encapsulated fibres presented are: (**A**) core-shell fibres composed of 2 wt% alginate only and (**B**) fibres made of 2 wt% alginate and 2 wt% gelatine blends. Extrusion flow rates used were 2000 $\mu l.min^{-1}$ for shell and 1500 $\mu l.min^{-1}$ for core. Day 0 represents the measurements taken of the fibres' structure on the day it was printed for the corresponding Day bar it is presented with. Data are shown as mean ± SD of one independent experiment, representative of pooled measurements from multiple samples. Statistical analysis using a two-tailed parametric and non-parametric t-test — on normally distributed and skewed data, respectively — between Day 0 and the corresponding day was carried out ($p \leq 0.05$). Non-significant results ($p > 0.05$) are not labelled on the graph. N = ranges between 3-13..... 132

Figure 4. 8: Camera photos of alginate core-shell fibres cultured in various conditions for a 28-day period. Alginate fibres printed under the same conditions were tested in various cell culture conditions. Cell culture conditions tested were: (**A**) supplemented DMEM with FBS at 37 °C, (**B**) supplemented DMEM without FBS at 37 °C, (**C**) RO water at 37 °C, and (**D**) RO water at 4 °C. Media was changed regularly. Each image represents an individual fibre that was printed specifically for the day the images were taken. Each row within the figure represents a specific day when images were acquired (Day 1, 7, 14, 21 and 28) for all groups, allowing for a visual comparison of fibre's morphology over time. For groups **A – C** on Day 21 and Day 28, infection occurred so the images could not be taken clearly without the lid for those time points. White dotted line is used to highlight the fibres that were not clearly visible. Scale bar: 5 mm. 135

Figure 4. 9: Phase-contrast images of temporal changes in core-shell alginate fibres cultured under various conditions. Alginate fibres printed under the same conditions were tested in various cell culture conditions. Cell culture conditions tested were: (**A**) supplemented DMEM with FBS at 37 °C, (**B**) supplemented DMEM without FBS at 37 °C, (**C**) RO water at 37 °C, and (**D**) RO water at 4 °C. Media was changed regularly. Each image represents an individual fibre that was printed specifically for the day the images were taken. Each row within the figure represents a specific day when images were acquired (Day 1, 7, 14, 21 and 28) for all groups, allowing for a

visual comparison of fibre's morphology over time. For groups **A – C** on Day 21 and Day 28, infection occurred so the images could not be taken for those time points. Scale bar: 500 μm. 138

Figure 4. 10: Temporal changes in core-shell alginate fibres' shell and width size when cultured under various conditions for 28 days. Alginate fibres printed under the same conditions were tested in various cell culture conditions. Cell culture media and conditions tested were: (**A**) supplemented DMEM with FBS at 37 °C, (**B**) supplemented DMEM without FBS at 37 °C, (**C**) RO water at 37 °C, and (**D**) RO water at 4 °C. Media was changed regularly. Extrusion flow rates used were 2000 μl.min^{-1} for shell and 1500 μl.min^{-1} for core. Width measurement data for all fibres' shell size are presented in the green graph (**Ai – Di**) and core size measurements for core-shell fibres are presented in blue graphs (**Aii – Dii**). Day 0 represents the measurements taken of the fibres' structure on the day it was printed for the corresponding Day bar it is presented with. Data are shown as mean ± SD of one independent experiment, representative of pooled measurements from multiple samples. Missing data for Day 21 and Day 28 for groups **A-C** are due to the loss of samples to infection. Statistical analysis using a two-tailed parametric and non-parametric t-test — on normally distributed and skewed data, respectively — between Day 0 and the corresponding day was carried out ($p \leq 0.05$). * $p \leq 0.05$, ** $p \leq 0.01$, *** $p \leq 0.001$, **** $p \leq 0.0001$. Non-significant results ($p > 0.05$) are not labelled on the graph. N = ranges between 8-11. 141

Figure 4. 11: Temporal changes in core-shell alginate fibres' W_{core}/W_{shell} when cultured under various conditions for 28 days. Alginate fibres printed under the same conditions were tested in various cell culture conditions. Cell culture media and conditions tested were: (**A**) supplemented DMEM with FBS at 37 °C, (**B**) supplemented DMEM without FBS at 37 °C, (**C**) RO water at 37 °C, and (**D**) RO water at 4 °C. Media was changed regularly. Extrusion flow rates used were 2000 μl.min^{-1} for shell and 1500 μl.min^{-1} for core. Day 0 represents the measurements taken of the fibres' structure on the day it was printed for the corresponding Day bar it is presented with. Data are shown as mean ± SD of one independent experiment, representative of pooled measurements from multiple samples. Missing data for Day 21 and Day 28 for groups **A-C** are due to the loss of samples to infection. Statistical analysis using a two-tailed parametric and non-parametric t-test — on normally distributed and skewed data, respectively — between Day 0 and the corresponding day was carried out ($p \leq 0.05$). * $p \leq 0.05$, ** $p \leq 0.01$, *** $p \leq 0.001$, **** $p \leq 0.0001$. Non-significant results ($p > 0.05$) are not labelled on the graph. N = ranges between 8-11. 144

Figure 5. 1: Perfusion test of alginate core-shell fibres. Time-lapse images demonstrating blue dye flowing through the core of hollow alginate fibres. Fibres

were perfused using the siphoning method, with one end in a tube containing blue dye, while the other end of the fibre was in a petri dish containing water. Fibres extruded using core flow rates of **A)** 125 µl.min^{-1}, **B)** 250 µl.min^{-1}, **C)** 500 µl.min^{-1}, **D)** 1000 µl.min^{-1}, **E)** 1500 µl.min^{-1}, **F)** 2000 µl.min^{-1} were tested, with a constant shell flow rate of 2000 µl.min^{-1}. **A – F (i)** show phase-contrast images of core-shell fibres' structure, while the corresponding camera images **(ii & iv)** for each group show the before and after perfusion of these fibres with blue dye. Close-up of each perfused fibre is also provided **(iv)**. Scale bar: 500 µm for **A – F (i)**, and 5 mm for **A – F (ii-iv)**. 159

Figure 5. 2: Perfusion of alginate-gelatine core-shell fibres. Core-shell fibres with different concentrations of gelatine (2 wt% to 10 wt%) in an alginate-gelatine blend were printed and perfused. Alginate concentration was kept as 2 wt%. **A - D (i)** show phase-contrast images of core-shell fibres' structure, while the corresponding camera images **(ii & iii)** for each group show the before and after perfusion of these fibres with blue dye. Close-up of each perfused fibre is also provided in **A-C (iv)**. Fibres printed with 10 wt% gelatine did not have a core and thus could not be perfused as shown in **D (ii-iv)**. Scale bar: 500 µm for **A-D (i)**, and 5 mm for **A - C (ii-iv)**. 161

Figure 5. 3: Cannulation of a core-shell fibre. The fibre with a core size of 500 µm (±50 µm) was cannulated with a 30G needle and perfused with blue dye mixed in water. Black arrow indicates the order of images. Yellow arrows indicate the flow of dye through the fibre's core and yellow circle highlights the bubbles released from the open end of the fibre, indicating the flow of dye through the fibre. Scale: 50 mm. .. 162

Figure 5. 4: Photographic images of fibre set up in a channel slide. A core-shell fibre was threaded through the channel of an ibidi slide with ends coming out of the two channels. The polymer coverslip stuck to the bottom-side of the ibidi slide pressed and flattened the fibre against the channel. 30 wt% Pluronic solution in the channels was not strong enough to hold the fibre in place for cannulation with a needle. Scale: 1 cm. 163

List of Abbreviations

2D	Two-Dimensional
3D	Three-Dimensional
3D-printing	Three-Dimensional printing
3T3	Murine 3T3 fibroblasts
ABS	Acrylonitrile butadiene styrene
AM	Additive Manufacturing
BM	Basement membrane
Ca^{2+}	Calcium ion
$CaCl_2$	Calcium chloride
Calcein-AM	Calcein acetoxymethyl ester
CONVEX	Continuously Varied extrusion
DMEM	Dulbecco's Modified Eagle's Medium – high glucose
DMSO	Dimethyl sulfoxide
DNA	Deoxyribonucleic acid
ECM	Extracellular Matrix
ECs	Endothelial cells
EtD-1	Ethidium homodimer-1
FBS	Foetal bovine serum
FITC-BSA	Fluorescein isothiocyanate-labelled bovine serum albumin
G	Gauge
Hif-1a	Hypoxia-inducible factor 1-alpha
HUVEC	Human umbilical vein endothelial cell
HUVSMC	Human umbilical vein smooth muscle cell

ISO	International Organization for Standardization
MEAM	Material Extrusion Additive Manufacturing
ml	Millilitre
mm	Millimetre
MMPs	Matrix metalloproteinases
MSCs	Mesenchymal stem cells
PBS	Phosphate buffered saline
PDMS	Polydimethylsiloxane
PVA	Polyvinyl alcohol
RGD	Arginine–glycine–aspartic acid
RO	Reverse osmosis
S1P	Sphingosine-1-Phosphate
SD	Standard deviation
SEM	Scanning electron microscope
SMC	Smooth muscle cell
Trypsin-EDTA	Trypsin-ethlyenediaminetetraacetic acid
UV	Ultraviolet
VEGF	Vascular endothelial growth factor
Wt%	Weight %
µm	Micrometres

1. Introduction

1.1. Research background and significance

Over the past several years, bone fracture incidences have increased worldwide due to various reasons such as aging population and bone-related conditions (1,2). As of 2019, approximately 178 million people have suffered from bone fractures (1). By 2025, hip fractures are predicted to increase by 310% for men and by 240% for women (3,4). Therefore, it is imperative to develop bone therapeutics to address a substantial number of individuals that are predicted to be affected in the future, as underscored by these statistics.

1.2. Bone tissue

Bone is an essential, hard and highly specialized connective tissue that serves multiple functions in the human body. These include structural and mechanical support, protection of vital organs, site of blood cell production (haematopoiesis) and reservoir for minerals (5,6). Bone tissue has a complex anatomy, consisting of various shapes, layers, cells, mineral composition, networks of nerves, blood and lymph vessels (5,7,8). Bone tissue is usually effective in remodelling and repairing itself after injury. However, damage to any of the bone components can result in various complications, including lack of structural stability, limb movement, and risk of damage to vital organs (9). Therefore, it is crucial to understand the complex

anatomy of bone tissue and provide therapeutics for healing bone injuries and disorders to prevent further health complications.

1.2.1. Types of bones

There are various types of bones in the human body, including long, short, flat, sesamoid and irregular bones (**Figure 1.1**) (10,11). Long bones such as the femur (thigh bone) and humerus (upper arm bone), are longer than they are wide (12). They primarily support the body's weight and movement. Short bones such as the carpals (wrists) and tarsals (ankles) are compact and cuboidal in shape. These are important for enabling fine motor skills. Flat bones are characterized by their thin and flat shape. These bones provide attachment support for muscles and protect the vital organs. For instance, the sternum and ribcage protect the heart and lungs (13). Flat bones contain the red bone marrow, in addition to the tip of long bones, where red blood cells are formed (14–16). Sesamoid bones are primarily found near joints and within tendons (13). They have a round pebble-like shape, such as the patella (kneecap) which enables tendons to glide smoothly during limb movement. Irregular bones don't belong in the previous categories as they have complex shapes which are unique to their functions. These include the vertebra which supports the spinal cord and skull which surrounds the brain (17). Cooperatively, these bones provide structure, mechanical support, protection, blood cell production and mineral storage.

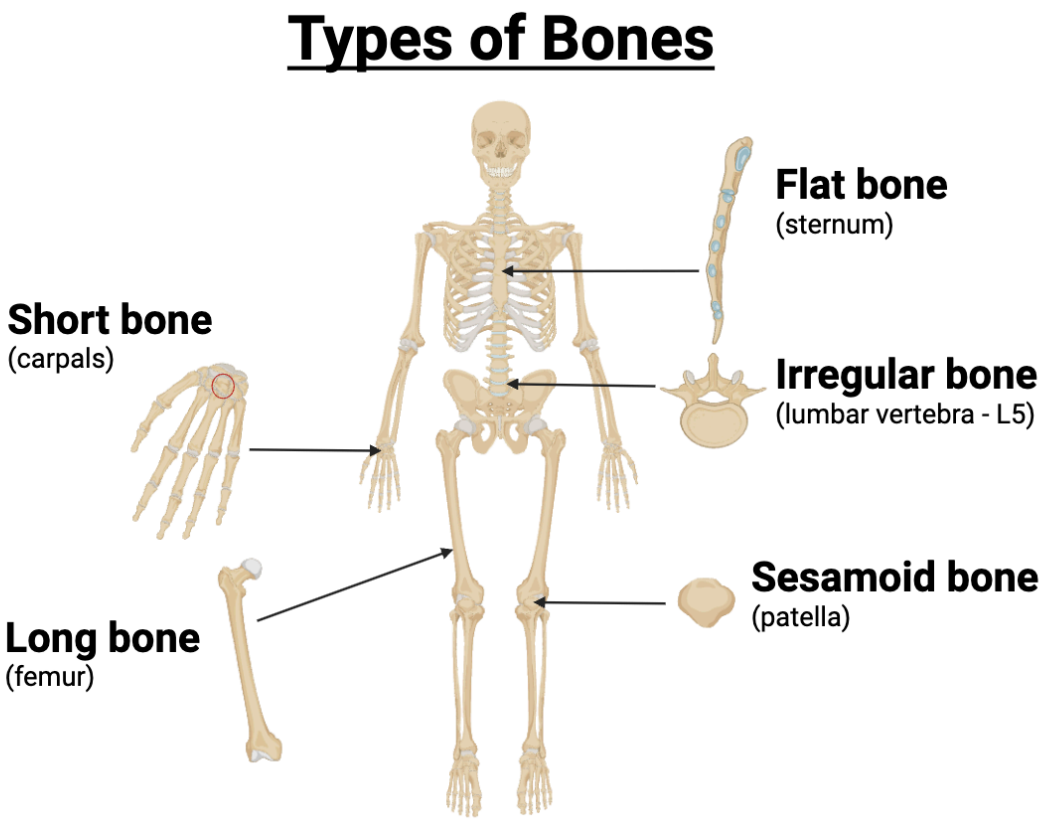


Figure 1. 1: Types of bones. There are various types of bones in the human body. These include flat, short, irregular, long and sesamoid bone (10–12). Created with BioRender.com.

1.2.2. Layers of bone tissue

The bone is composed of various layers of tissues that work together to create a strong, durable skeletal system (**Figure 1.2 & 1.3**). These primarily include periosteum, endosteum, compact bone and spongy bone (18).

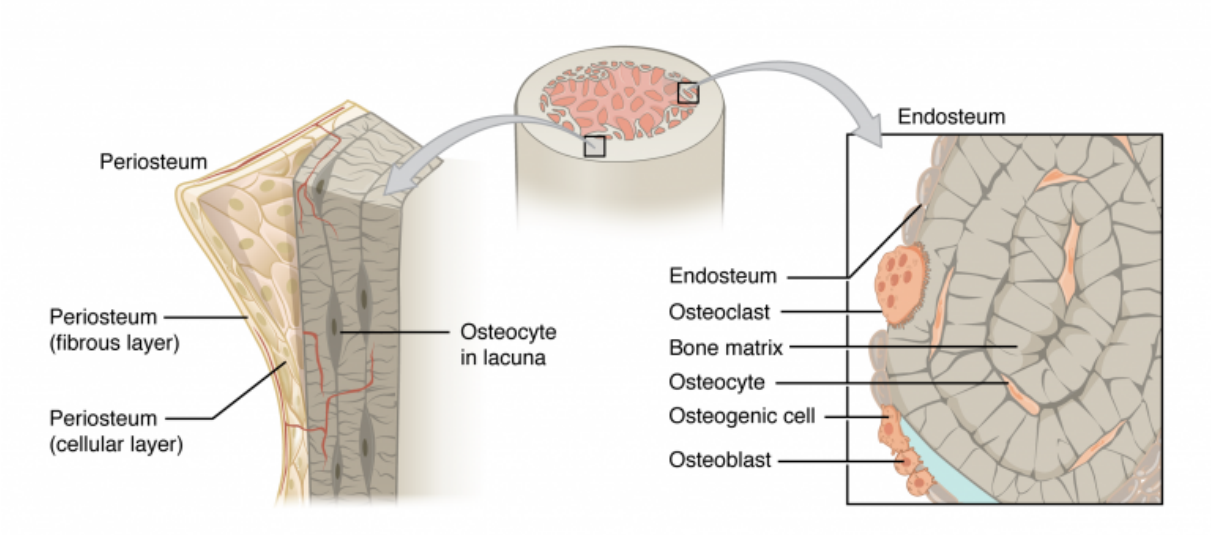


Figure 1. 2: Periosteum and Endosteum. Bone is made up of layers called periosteum and endosteum. Periosteum is the outer layer, composed of fibrous and cellular components, and surrounds the layer called endosteum. Endosteum contains the bone matrix and multiple cells (e.g., osteoclasts, osteocytes, osteogenic cells and osteoblasts) (19).

A periosteum is a dense and highly vascularized layer of connective tissue that covers the bone's surface (**Figure 1.2**) (14). It has two layers, fibrous and osteogenic, which play a key role in bone growth, repair, and overall health by supplying blood to the bone tissue (20). Fibrous layer provides support in terms of attachment between tendons and ligaments and is dense (21). Osteogenic layer contains cells such as osteocytes, osteoblasts and osteoclasts, which facilitate the regeneration and remodelling of bone tissue throughout life (18). The periosteum serves as a passageway for blood vessels entering the bone through the Volkmann's canals (14).

Endosteum is a layer of connective tissue that lines the inner surface of the bone's wall (**Figure 1.2**) (18). It is rich in fine blood vessels and surrounds the Haversian canal and other internal cavities of the bone. It is primarily composed of osteoblasts and single bone-lining cells (22). Osteoblasts are normally flattened and

are surrounded by type III collagen (8). Upon activation, these cells transform into a cuboidal shape and begin depositing a fresh layer of unmineralized bone matrix (10,22,23). Upon mineralization, this layer transforms into inner circumferential lamella (18).

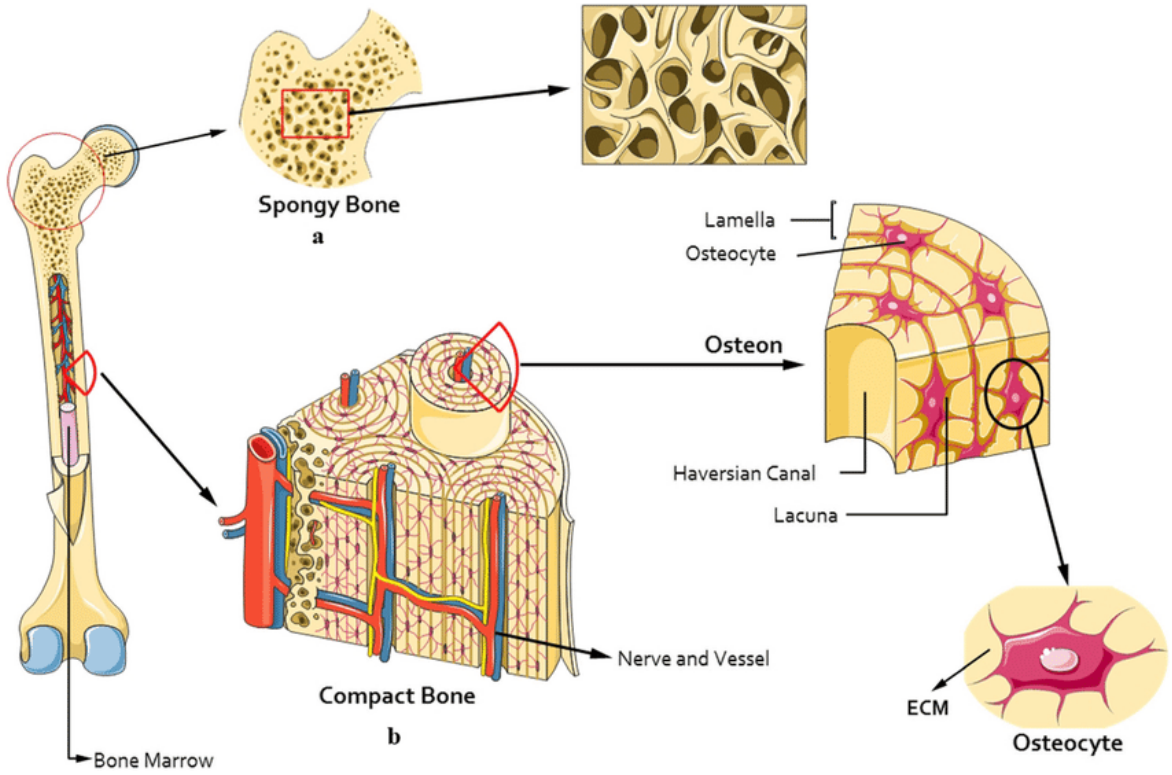


Figure 1. 3: Compact and spongy bone. There are multiple layers of bone, containing various cellular (e.g., osteocytes) and structural (e.g., lamella and lacuna) components. Compact bone is made up of circular units called osteons, which are heavily innervated and vascularised through channels called Haversian canal. Spongy bone tissue makes up the internal structure of the bone and houses the bone marrow (24).

The outer layer of the bones is composed of compact bone, also known as cortical bone, which is responsible for the rigidity of the bone due to its high density (**Figure 1.3**) (25). Compact bone is comprised of osteons, which are concentric layers of calcified matrix or lamellae (14,22). These lamellae surround a central

channel called Haversian canal, which contains the blood vessels, lymph vessels and nerves (19,25). While Haversian canals run longitudinally along the bone's axis, Volkmann's canals extend perpendicularly, linking the blood vessels of different osteons and the periosteum (14,25). These blood vessels play a crucial role in the maintenance of bone tissues by providing oxygen and removing waste amongst other functions.

Spongy bone, also known as cancellous or trabecular bone, is mainly found in the ends of the long bones and makes up the interior of some bones such as the pelvis or vertebrae (**Figure 1.3**) (26). Compared to compact bone, spongy bones are lighter and less dense as they are made up of a network of rod-like structures called trabeculae which provide structural support while minimizing the weight (10). Porous, lattice-like trabeculae structure of the spongy bones contain the bone marrow, which is richly supplied with blood vessels and is primarily responsible for the production of blood cells (haematopoiesis) (14).

1.2.3. Composition of the bone matrix

The bone matrix is composed of organic and inorganic materials. Organic component constitutes 30% of the bone matrix and it is mainly composed of collagen fibers (23). Collagen fibers provide tensile strength and elasticity, allowing bones to absorb impact without breaking (25,26). Additionally, various proteins and glycoproteins are present in the organic matrix which help form and maintain the bone tissue (27). Inorganic component constitutes 70% of the bone matrix and is primarily made up of hydroxyapatite (23). Hydroxyapatite is a crystalline form of

calcium phosphate and provides bone with a hardness and ability to endure compressive forces (19,28). The fine balance between the organic and inorganic components of the bone matrix is essential in ensuring the bones are strong yet not brittle, for maintaining the correct structural role of bones in the body (28).

1.2.4. Cellular components of bone

There are four main types of cells in the bone tissue: osteoprogenitor cells, osteoblasts, osteocytes, and osteoclasts (**Figure 1.2 & 1.3**) (24). Osteoprogenitor cells are the stem cells that differentiate into osteoblasts (23). They are located in the outer fibrous layer of bone (periosteum) and inner layer (endosteum) (18). Osteoblasts are bone-forming cells that secrete organic components, such as collagen, which are then mineralized to form bone (23). Osteocytes, derived from osteoblasts, are mature bone cells responsible for the exchange of minerals and are located within the bone matrix, in small cavities called lacunae (**Figure 1.3**) (10). Osteocytes communicate with other osteocytes through tiny channels called canaliculi for maintenance of bone tissue (29). Osteoclasts are large multinucleated cells that resorb bone tissue. They play a crucial role in calcium homeostasis, bone remodelling and repair through the breakdown of bone matrix (23).

1.2.5. Current bone transplantation strategies

Although bone tissue is constantly regenerated throughout an individual's lifespan, bone defects as a result of infection, trauma, or tumour removal do not heal

properly (7–9). This can result in a non-healing or non-union fractures, often due to lack of angiogenesis at the site of injury (32–35). Current gold standard for treatment of bone defect is autologous bone grafts, which involves replacement of defected bone tissue with a healthy bone tissue from the same individual (36). However, they are associated with donor site morbidity and limited tissue available for grafts (35,36). On the other hand, allogenic grafts can be utilised which involves the use of tissue from another individual (donor) (36). While allogenic grafts offer advantages, such as eliminating the need for further surgery to harvest healthy tissue from the patient (host), they are also associated with further complications such as a limited supply of organ donors, risk of infection and rejection by the host body in response to a transplanted tissue (37–40).

1.2.6. Bone replacement using tissue engineering

Promising novel technologies have been designed, based on tissue engineering, which target the angiogenic process in bone healing combining both mechanical and biological factors (30,41–43). These include scaffolding materials made of synthetic and naturally derived materials, seeded with stem cells and growth factors to promote bone regeneration (**Figure 1.4**) (44–46). Tissue engineering provides various advantages over current bone transplant methods. It allows fabrication of tailored scaffolds that can be customised using materials, cells and growth factors to elicit specific healing responses, thus reducing complications and

improving outcomes (44,47). By closely mimicking the natural bone structure, tissue-engineered constructs provide enhanced biological compatibility and reduce the risk of rejection by host's system (44).

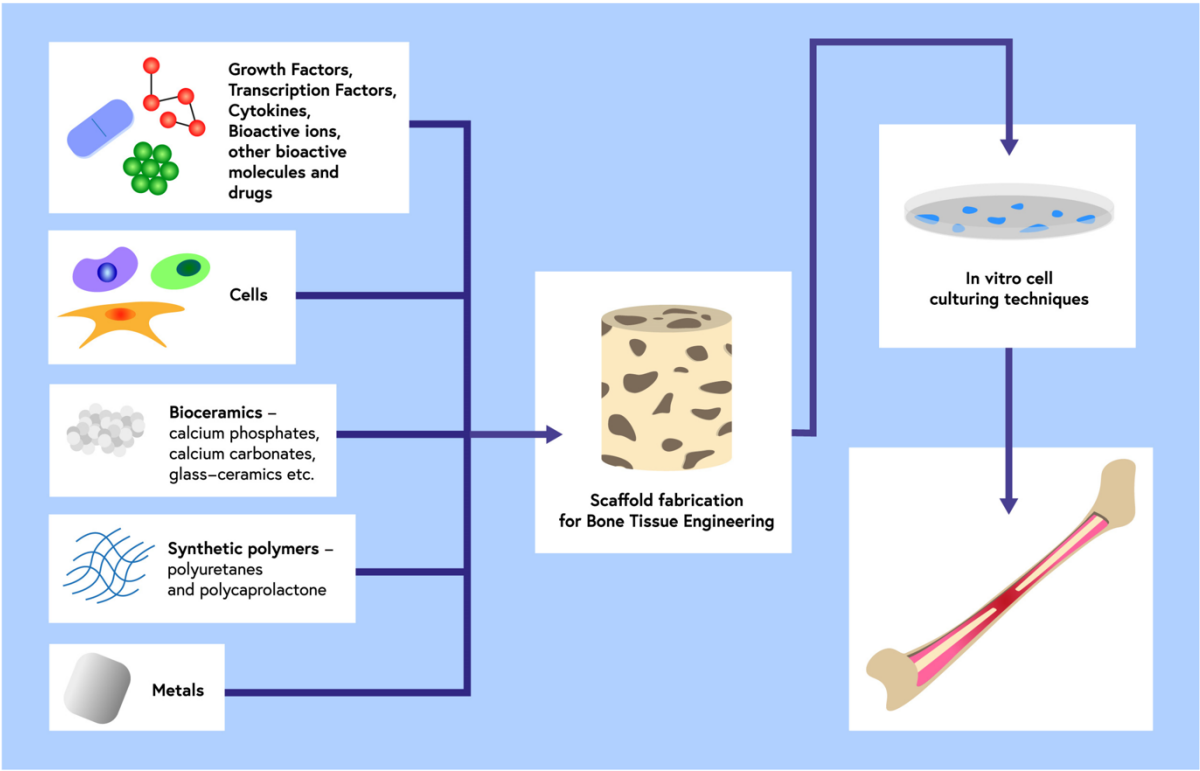


Figure 1. 4: Overview of bone tissue engineering. Tissue engineering involves fabricating a scaffold made of a variety of materials, cells and growth factors to induce bone regeneration (48).

1.2.7. A current challenge in bone tissue engineering

Although there are many methods developed to generate bone tissue, there is still a challenge to keep the cells in that artificially constructed tissue viable and functioning while it is being printed, transplanted and as it integrates into the host

tissue (49). Therefore, a mode of transporting gases and nutrients, through incorporation of vasculature into the scaffold, is crucial for the physiology and viability of cells in that tissue and it can potentially speed up the integration of an implanted tissue (37,44,49). Thus, the development of perfusable vascular conduits can facilitate the success of organ transplantation (39,49).

1.2.8. Vascularised bone tissue

Vascular-like structures, that mimic *in vivo* blood vessels, can be created using tissue engineering methods for vascularization and perfusion of 3D-printed bone scaffolds. Tissue engineering is a promising field in the context of fabricating blood vessel mimics to facilitate the growth and function of transplanted bone tissue organs (50). To achieve this, several strategies are being explored such as the use of synthetic and protein-based polymers (e.g., collagen, fibrin), and 3D bioprinting techniques (51,52). These strategies utilise self-assembled vascular networks, cell-encapsulated hydrogels, cross-linking of polymers to enhance mechanical and biological functions, and decellularised native tissues (51). However, there is still a lack of an anatomically accurate blood vessel model that can perform the physiological functions of a human blood vessel (53–55). This chapter will focus on understanding the importance of vasculature in the body, its characteristics, and current methods of artificially fabricating the human vasculature for use in tissue engineering for regenerative medicine.

1.3. Vasculature: an unmet need

Human vasculature is essential for the human body as it adapts throughout life according to the specific needs of tissue physiology as well as during disease (55). Tissues are highly vascularised to allow the gas exchange (such as oxygen and carbon dioxide), removal of waste and to transport important components to cells for tissue maintenance such as nutrients and growth factors (49,56). The distance between the cells and capillaries in a tissue is 100–200 μm to maintain the gradients for gases, and an increase in this distance can be detrimental to the cells out of the range of capillaries (50,57,58). Therefore, it is very important for the artificially engineered tissues to be vascularised properly to ensure every cell is sufficiently provided with oxygen and nutrients to remain viable.

Blood vessels play a key role in facilitating the interaction of different organs in the body, for example, in hormonal and growth factor transport (59). Due to the lack of tools to recapitulate the human vasculature *in vitro* because of its complex structure and functions, it has been a challenge to recreate the vasculature *in vitro* for disease modelling and tissue engineering for regenerative medicine (60). There are different strategies proposed to vascularise artificially engineered tissue (37,61). For instance, one approach is to introduce growth factors which can be released upon implantation to trigger angiogenesis in a controlled manner in the host tissue. The other is to bio-print the vessels and integrate those into the engineered tissue. Both methods are used in drug development to create viable vascularised tissues for testing new therapies (37).

1.3.1. Vessel formation

Neovascularisation is the formation of new blood vessels, which plays a key role in normal physiology as well as the progression of diseases such as cancer (62). Initial blood vessel formation in a developing embryo, known as vasculogenisesis, helps with providing oxygen, nutrients, and growth factors to growing tissues and organs (56,62). Angiogenesis is the process of blood vessel formation from pre-existing vessels in areas where there is a lack of oxygen and can happen following vasculogenisesis as well as throughout the life of an individual (61,62).

1.3.2. Angiogenesis

Angiogenesis plays a key role in tissue regeneration following damage to the tissue caused by an injury (62). The formation of new blood vessels supports the regrowth of lost tissue. There are many studies carried out to understand this underlying mechanism of blood vessels formation and its role in disease progression (62,63). However, the gap in knowledge for our understanding of vasculature still remains, that needs to be addressed to facilitate the treatment of diseases (62,64).

Angiogenesis has been one of the popular research topics since the discovery of a network formation by the endothelial cells (ECs) (65). Early studies include using tumour cells by Folkman & Haudenschild in 1980, aortic ring assay, organ culture assays in Matrigel (65–67). Currently, there has been an increase in 3D fabrication of tube structures to mimic the blood vessel models by either seeding the hydrogels with cells or perfusing the cells through the fibres (60,63,68).

1.3.3. Role of oxygen levels in vessel formation

The levels of oxygen the cells are exposed to in a tissue plays a huge role in their activity, such as in oxidative metabolism (69). Oxidative stress caused by high levels of oxygen can damage cellular DNA and affect cell viability (70). On the other hand, cells release hypoxia-inducible factor 1-alpha (Hif-1a) in response to hypoxia (lack of oxygen) which results in the upregulation of vascular endothelial growth factor (VEGF) (62,71). VEGF promotes the stalk formation from local blood vessels by acting on ECs, which elongate to form a blood vessel which stretches from the original vessel, that the growth factors acted on, to the hypoxic cells in the tissue (**Figure 1.5**) (62).

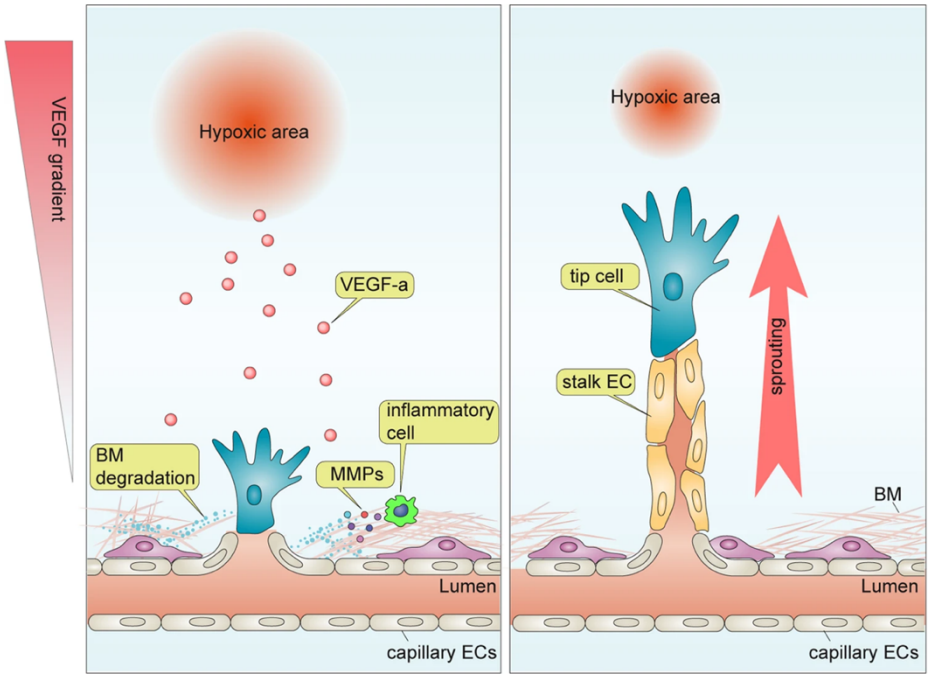


Figure 1. 5: Angiogenesis process. Sprouting of blood vessels, regulated by growth factors such as VEGF, ensure adequate oxygen is supplied to all cells. In response to low oxygen level (hypoxia) stimulus, ECs sprout towards the area of hypoxia, forming a new branch of blood vessel. Matrix metalloproteinases (MMPs) degrade the basement membrane (BM) allowing the 'tip cell' to lead a stalk of ECs towards the hypoxic area (72).

In addition to tissue engineering, developing 3D blood vessels mimics can help with studies such as ischemia/reperfusion injury where the flow of oxygen can be controlled by regulating the perfusion of media through the tubes (73,74).

1.3.4. Types of blood vessels

The vasculature tree consists of a hierarchical network of continuous series of blood vessels that range in size and structure, as presented in **Table 1.1** and **Figure 1.6 & 1.7** (37,56,75,76). Each section of the vasculature tree plays a specific role in the transport of blood and its constituents. There are three main types of blood vessels in the human body, including arteries, capillaries and veins. Aorta and vena cava are the major blood vessels in the body; however, smaller blood vessels will be given focus in this project due to their relevance in bone tissue engineering for regenerative medicine (77,78).

Arteries are the major sized blood vessels, ranging from 0.6 mm to 10 mm, that transport blood away from the heart towards other organs and tissues (76,79). Arterioles are the smaller branches of arteries ranging from 7 μm to 300 μm, that connect the arteries to capillaries (76,79–81). Capillaries are the smallest blood vessels, ranging from 4 μm to 10 μm (76,79,82). These vessels form an extensive network, called capillary bed, in the tissues and are the main site of gas, nutrient and waste exchange between the tissue and blood. Venules are the smaller veins, ranging from 20 μm to 25 μm, that transport the blood away from the capillary beds (76,79,83). Veins ranging from 0.4 mm to 16 mm, take blood back to the heart, via the vena cava.

Table 1. 1: Overview of the blood vessel diameter for different sections of the vasculature tree. The diameter of the blood vessel varies depending on the age, sex and exercise level of an individual (76,78–82,84,85).

Vessel type	Diameter (mm)
Aorta	~ 30
Vena cava	12 – 20
Arteries	0.6 – 10
Veins	0.4 – 16
Arterioles	0.007 – 0.3
Venules	0.02 – 0.025
Capillaries	0.004 – 0.01

1.3.5. Structure of blood vessels

The structure of each section of the vasculature, particularly the wall of the blood vessels, facilitates its function (**Figure 1.6 & 1.7**). These include the wall's thickness, the layers that make up the vessel wall, endothelial lining and presence of valves for some sections of the vasculature tree.

Arteries have large, thick and elastic walls, that help them withstand the high pressures of blood that is ejected from the heart (56). The elastic ability of the arteries' wall helps them recoil after the contraction (systole) phase of the heart cycle. The three layers of arteries are tunica adventitia, tunica media and tunica intima (84). Tunica adventitia is the outer most layer of the artery. It is a connective tissue made up of collagen and elastic fibbers, which anchor the artery to its surrounding tissues. Tunica media is the middle layer of artery (83). It is made up of smooth muscle cells (SMCs) and elastic fibers that help the vessel wall to contract (vasoconstriction) and relax (vasodilation) for blood pressure regulation. The innermost layer is called the

tunica intima, and it is made up of a single layer of endothelial cells and a very thin subendothelial layer (83). This layer helps reduce friction of blood flow.

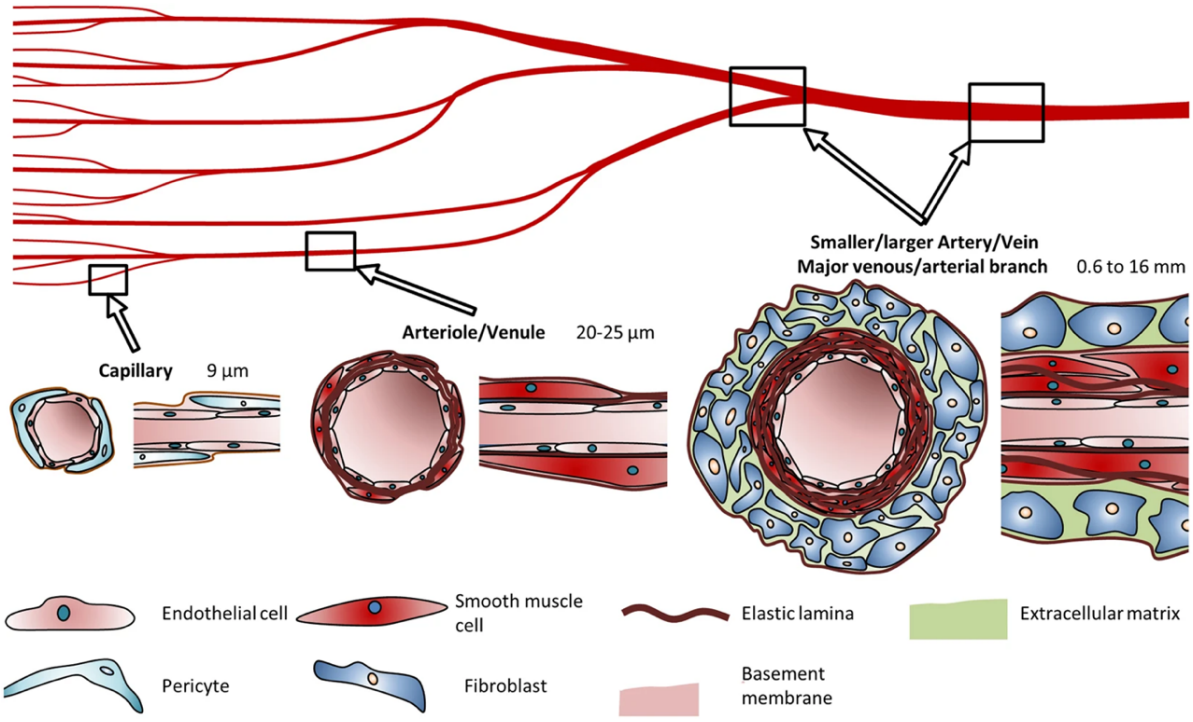


Figure 1. 6: Structure and components of blood vessels. This diagram illustrates the different sizes of blood vessels in the human body with different wall structures. Main vessel types include large vessels (arteries and veins), small vessels (arterioles and venules) and capillaries. A range of cells and components provide support to the blood vessels, such as fibroblasts and elastic lamina (76).

Veins have larger diameters than arteries, however the wall is less thick due to reduced pressure of blood (85). Veins are also made up of the three layers like arteries (86). However, the tunica adventia is much thicker compared to arteries with more collagen and elastin fibers (83,85). The tunica media is thinner due to less SMCs present (83,87). The tunica intima contains valves, in addition to endothelial cells, that prevent the back flow of blood (56). This is particularly useful in legs where

the blood is transported against gravity towards the heart. Valves are also present in some venules (88).

Arterioles have similar wall structure to arteries, except the tunica media layer is much thinner, and the elastic fibers are reduced (75). Blood flow and blood pressure is primarily regulated by arterioles through the vasoconstriction and vasodilation mechanism (56). This mechanism is controlled in response to various stimuli, such as nervous signals, hormones, and local chemical factors (89).

Venules are smaller in diameter compared to veins and have thinner walls (56). These walls are made up of thin tunica media and a tunica adventitia. Thin walls of the venules, with only a few layers of SMCs, allow them to easily become permeable, for instance during inflammation (90).

Capillary walls are made of a single layer of endothelial cells, a thin basement membrane (83). The lack of other components, such as SMCs and elastic fibres, allow easy exchange of gases, nutrients, and waste products between blood and the surrounding tissues through diffusion (56). The wall of capillaries varies depending on the tissue they are in (83). For example, bone marrow has sinusoidal capillaries which have large gaps between the endothelial cells (82). These gaps allow easier passage for larger molecules like proteins and cells.

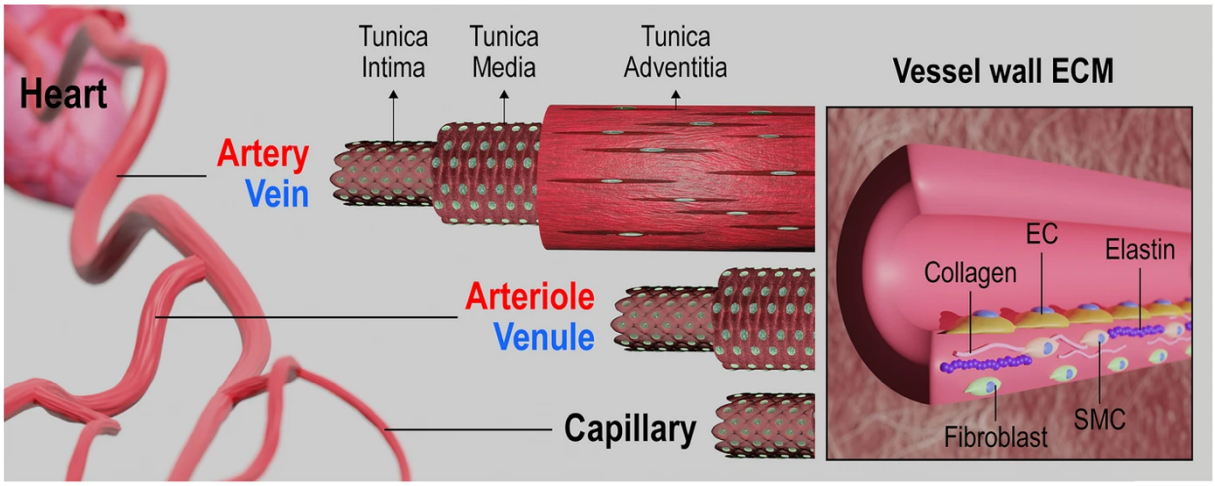


Figure 1. 7: Vessel wall layers. Blood vessels are made up of three main layers: tunica adventitia, tunica media and tunica intima (91).

1.3.6. Endothelial barrier formation

Endothelial barrier formation is an important thing to study while developing new blood vessel models (65). This is because the endothelial permeability plays a key role in maintaining tissue homeostasis for the transport of gasses, nutrients, ions and other key materials across the blood vessel wall, into and out of the tissue (65,92). Additionally, the correct permeability of the endothelium is crucial for the inflammation response because when the immune cells are recruited to the site of injury, they can easily permeate through the endothelial barrier as it becomes looser (92).

1.3.7. Biochemical gradients

ECs undergo temporal growth factor regulation in response to the biochemical gradients in the extracellular matrix (ECM) (65). These gradients, either uniform or

distributed in varying degrees, play a key role in angiogenesis. For instance, VEGF through the action of and in addition to other growth factor plays an important role in micro vessel formation in the hypoxic tissue (71). Sphingosine-1-Phosphate (S1P), alongside VEGF, plays an important role in initiating the morphological changes of the ECs *in vivo* (93).

1.3.8. Types of flow in the blood vasculature

Blood flow has been reported to play a key role in ECs', lining the vascular walls, morphology and migration (55,94). There are two main types of flow in the vasculature, laminar and disturbed flow (94). Laminar flow is the parallel flow of blood through a straight blood vessel or tube and causes uniform stress across the blood vessel walls. Disturbed flow, on the other hand, causes high shear stress on the wall it hits, and the stress is random throughout the vessel. Disturbed flow is found in structures such as bifurcations of vessels and aortic arches (95). The constant flow of fluid through the lumen of blood vessel, layered with ECs, will cause the cells to grow, spread and line the inner wall of the channel forming an endothelial barrier (92). Due to the uniform distribution of the stress on the vessel wall at the locations of laminar flow, ECs are aligned along the direction of the flow. As for the locations with the disturbed flow, there are increased chances of developing atherosclerotic plaques due to high stress on the blood vessel walls (55). Another flow is called swirling blood flow, or helical flow, that has protective effects against cardiovascular conditions such as atherosclerosis and can be found in some blood vessels in the body (96). Therefore, recapitulating the different types of blood flow in an *in vitro*

vasculature model can provide a variety of research to be conducted beyond regenerative medicine, such as for disease modelling and testing new therapeutic agents in pharmaceutical industry.

1.3.9. Current 3D artificial blood vessels

There has been some development in current tissue engineering methods of different sized blood vessels with co-cultured cells.

Melchiorri et al. (2016) generated vasculature mimics with inner diameters of 1 mm and wall thicknesses of 150 μm using a biodegradable material called poly(propylene fumarate) (PPF) (97). Human umbilical vein endothelial cells (HUVECs) and human umbilical vein smooth muscle cells (HUVSMCs) were cultured on these scaffolds, which showed sufficient cell attachment and viability. The vascular graft remained unobstructed and functional within rodent models following surgical implantation in the venous system. Additionally, Gao et al. (2017) developed 3D alginate scaffolds with diameter of 832 μm, which is a relevant size to a small arterial vessel (98). The printed scaffolds were mechanically stable and biocompatible, as shown by culture with mouse fibroblasts. Co-culture of vessel-related cell lines, i.e., fibroblasts, SMCs, and HUVECs in the vasculature mimics demonstrated adherence to the material, spreading and formation of cellular junctions.

Vascular scaffolds, around the size of arterioles and venules, were created by Song et al. (2021) (99). Electrospun fibrous membranes were rolled around a glass

rod to fabricate scaffolds with inner diameter of 2.68 ± 0.08 mm and outer diameter of 3.89 ± 0.04 mm. Up to 14 days of *in vitro* studies showed good cell adhesion, proliferation and morphology using the A7r5 SMCs. Perfusion of the fibres with media (to mimic blood flow), and co-culture of vascular cells was not shown in this study.

Sarveswaran et al. (2016) used live cell lithography technique to engineer perfusable microvessels that replicate the sinusoidal or fenestrated capillaries found *in vivo* (58). *Bona fide* capillary, with a lumen size as narrow as 5 μm, was reported to be created through precise assembly and co-culture of human microvascular endothelial cells, human pericytes from the placenta, and human neonatal fibroblasts in a hydrogel material. Although revolutionary, only sinusoidal capillaries could be created. A mechanism to create a wide range of capillaries that recapitulate the capillary structure found *in vivo*, such as continuous, fenestrated, and discontinuous capillaries is still in demand.

When designing the blood vessel mimics, it is important to recapitulate the structure of the blood vessels as closely as possible to the one *in vivo* (100). For instance, vascular conduits were designed with rectangular-shaped tubes instead of circular-shaped tubes in previous studies by Yang et al. (2011) (101). Leucocytes were shown to distribute differently in the rectangle channel which was not the same as those *in vivo*, as observed in channels with circular cross-section.

1.4. Additive manufacturing

Additive manufacturing (AM), also known as 3D-printing, is popular in the field of tissue regeneration research (102). It is a manufacturing process that involves creating desired 3D models using a layer-by-layer approach, as opposed to traditional manufacturing processes that involve mining or cutting away of material from a solid mass of block (**Figure 1.8**) (103,104). With AM, complex geometries can be created with a potential for customisation and rapid prototyping, while minimising material waste.

In healthcare, AM gives users the ability to create personalised implants for each patient, without additional moulding, and the composition of the ink materials can be customised depending on the desired properties of the final product (102,105). For example, temperature or pH responsive inks can be used, or hydrogel with low or high porosity can be used in different areas of the product (106,107). This allows the users to put materials with specific properties where they are needed most in the 3D model (105).

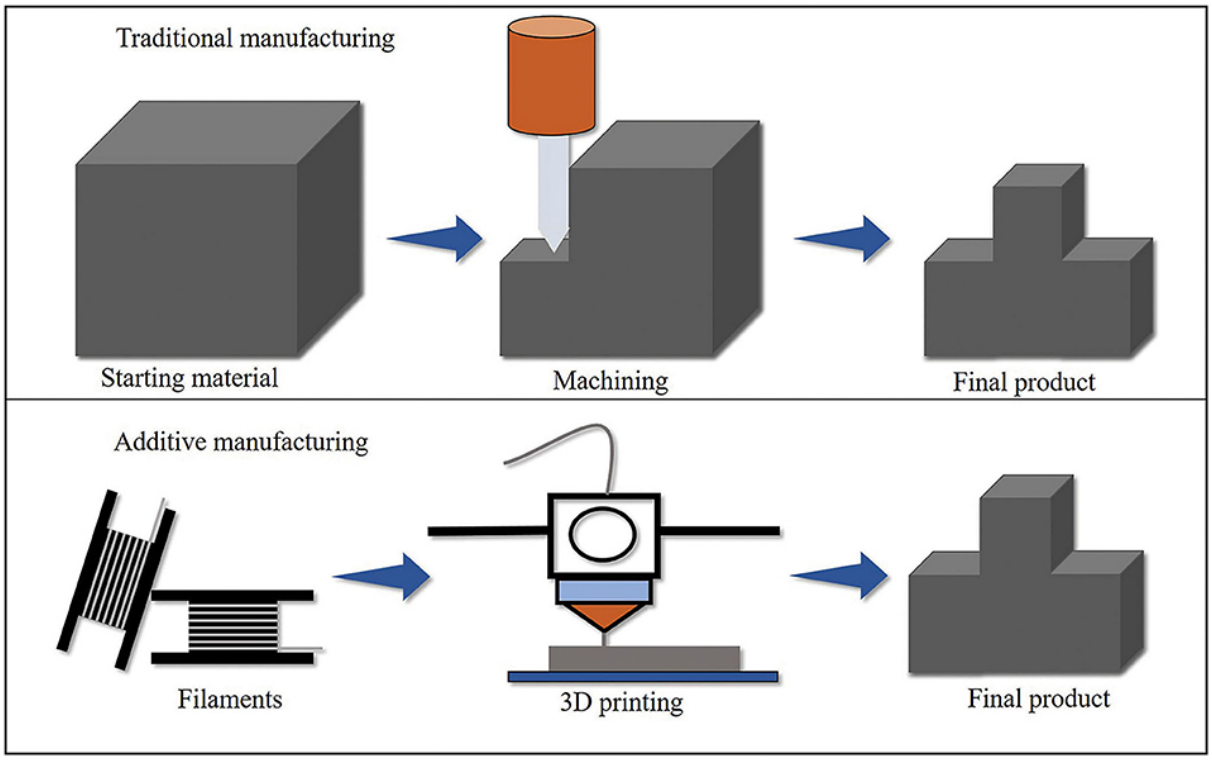


Figure 1. 8: Additive manufacturing process. A simplified diagram to illustrate the key difference between traditional manufacturing process and additive manufacturing. Traditional manufacturing process involves machining to create a desired product, while creating large waste from raw material. Whereas AM uses filaments as raw material to precisely create 3D structures with minimum waste (104).

1.4.1. Types of additive manufacturing

There are different types of commonly used AM methods, such as laser-assisted, inkjet and material extrusion (**Figure 1.9**). In laser-assisted printing, laser pulses are concentrated on to a donor slide which absorbs the energy to propel droplets of hydrogel onto the printing platform. Inkjet printing involves ejecting droplets of polymers using thermal or electrical (piezoelectric) energy through a nozzle (108). Material extrusion involves the extrusion of materials, such as hydrogel precursors, through a nozzle in the form of filament or beads (105,108).

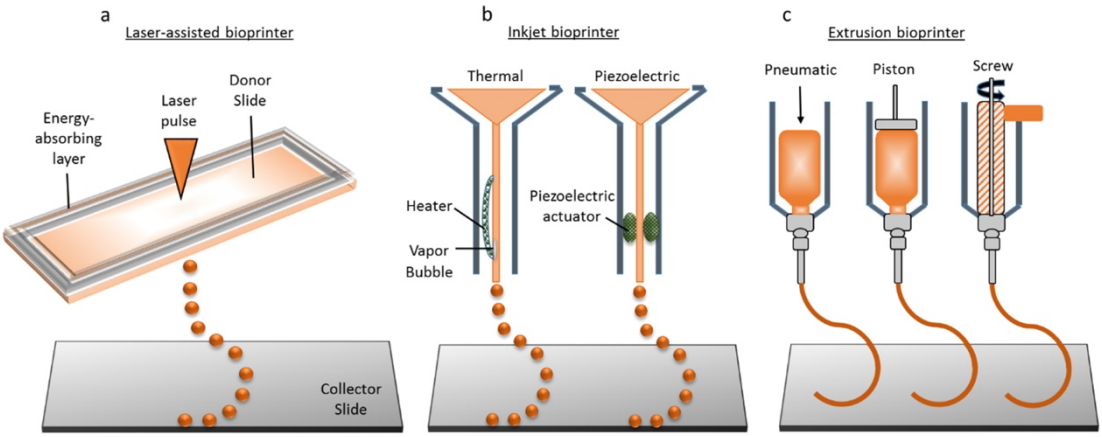


Figure 1. 9: Main types of additive manufacturing. The diagram shows the three main types of printing methods used for fabricating tissue mimics in regenerative medicine. These include **a**) laser-assisted, **b**) inkjet and **c**) material extrusion (108).

1.4.2. Material extrusion additive manufacturing

Material extrusion additive manufacturing (MEAM) is a commonly used method of AM in tissue engineering (109). Common examples of MEAM involve dispensing material through a syringe or a heated nozzle (105). Hutmacher introduced MEAM for fabricating scaffold for tissue engineering in 2000, which involved the extrusion of filaments in a precise order in a layer-by-layer manner (109). Tissue scaffolds can be printed with the desired amount of porosity to allow the cells embedded in the scaffolds to receive nutrients and oxygen for growth and to allow the ingrowth of the host's blood vessels into the scaffold for its integration with the host tissue (109). For this project, MEAM (or extrusion-based printing) will be used, to extrude materials through a microfluidic-based device, due to its versatility, affordability, and a wider selection of materials (110).

1.4.3. Scaffold material

The scaffold material (bioink) is the primary component of tissue engineering (38,111). It must be biocompatible so that it does not cause any harm to the embedded cells as well as the host's local tissue (112). Scaffolding materials provide physical support to the cells and other constituents, if any, and their characteristics can be fine-tuned to give desired outcomes (38,113). For instance, properties of the biomaterials can be functionalised to induce angiogenesis (38,114). The biomaterials used for the fabrication of vascular conduits should be biocompatible and be mechanically stable once the gel is formed, however, not too stiff that it can reduce the permeability of fibres' walls. The second key constituent of tissue engineering is the cells which will form the desired tissue (38). These include the ECs, SMCs or mesenchymal stem cells (MSCs). The third key aspect of the tissue engineering is the signalling mechanisms, either by the material itself (intrinsically) or the addition of growth factors and drugs (exogenously) (38,115).

Alginate is a naturally derived polysaccharide from marine algae and is used in the food industry as an ingredient in foods and beverages, to control blood sugar and insulin levels, and to create edible food coatings and films (116,117). Alginate hydrogels are widely used in the biomedical field, either on their own or in combination with other materials, to enhance the delivery of bioactive substances, drugs, tissue regeneration, wound healing, 3D-printing and *in vitro* modelling (116,118). In this project, the potential of alginate hydrogel to create blood vessel mimics will be assessed and the areas of improvement for the material will be identified.

1.4.4. Microfluidics-based devices for 3D bioprinting of blood vessel mimics

Microfluidics is the term used for controlling and manipulating fluids at a microscale level, through channels or devices with dimensions ranging from μm to mm (119). Microfluidic-based devices are popular across many fields, including tissue engineering and 3D-printing (120). A 3D-printing nozzle, with microfluidic-based channels, can be used to precisely control and deposit multiple biomaterials for fabrication of tissue mimics (121).

Hollow tubes as vascular mimics can be 3D-printed using microfluidic-based devices (49,68,122,123). There are different methods of fabricating microfluidic-based devices which include soft lithography, micro moulding, micromachining or milling and 3D-printing (62). Soft Lithography uses UV and thermal curing to produce a microfluidic device. Soft lithography is commonly used because of its affordability, ease of design and adaptability (124). Although the microfluidic devices manufactured using PDMS, that use photo or soft lithographic processes, are well established, they have drawbacks (110). These drawbacks include the high costs of raw materials, time-consuming steps and difficulty to automate the process (110,124).

1.4.5. Coaxial printing

Coaxial printing involves concentric deposition of two or more solutions through a nozzle to create tubular structures (125). There are many coaxial extrusion printing

devices being researched currently that fabricate hollow perfusable fibres for vascular mimics, with a range of core/lumen sizes (**Table 1.2**). However, the fabrication methods used are complicated and, for some, only straight core fibres have been generated.

Table 1. 2: Previous work has shown that perfusable hollow fibres can be fabricated with a range of core widths, using different extrusion set-ups.

Authors	Core width (μm)	Fibre width (μm)	Extrusion nozzle size	Extrusion rate	Materials used	Cell lines used
X. Dai et al, 2017. (126)	242.89 - 527.49	870	Outer nozzle: 1250 μm Centre nozzle: 510 μm	Shell: 0.25 – 0.5 ml min−1 Core: 0.05– 0.1 ml min−1	Alginate: 3wt% Gelatin: 5wt% $CaCl_2$: 3wt% Fibrinogen: 3wt%	GSC23 HMSCs
V. T. Duong et al.,2020. (68)	230	850-890	580 μm	Shell: 0.7 ml min−1 Core: 0.01 ml min−1, 0.1 ml min−1	Type I collagen: 3mg ml−1 Alginate: 1.8wt% NaCl: 145 mM $CaCl_2$: 100 mM	HUVECs HASMCs
W. Jia et al., 2016. (127)	400 - 1000	500 – 1500	Internal needles: 27G - 30G External needles: 18G - 25G	Internal Channels (shell): 0.035 ml min−1 External channels (core): 0.07 ml min−1	Alginate: (1, 2, and 3wt%) GelMA: (5 and 7wt%) PEGTA: (1, 2, and 3wt%) $CaCl_2$: 0.3M	HUVECs HMSCs
W. Liu et al., 2018. (128)	469 - 723	-	Internal needles: 28G External needles: 23G	0.2-0.9 ml min−1	Alginate: (1wt%) GelMA: (1.0, 1.5, and 2.0wt%) $CaCl_2$: 1wt% and 6wt%	HUVECs MDA-MB-231 MCF7 NIH/3T3

Y. Yu et al., 2022. (129)	785	1668	Internal pipes: 600 μm External pipe: 2200 μm	Internal pipe: 0.03, 0.04, 0.05 mm s−1 External pipe: 25, 30, 35 PSI	Alginate: 1–4wt% Type I collagen: 1wt% $CaCl_2$: 1–4 wt%	HepG2 Min6
M. Mao et al., 2021. (130)	224.5 - 361.57	440 - 561.42	19G & 26G	Shell: 0.025 ml/min - 0.05 mL h-1 Core: 0.0067 ml min−1 - 0.01167 ml min−1	Alginate: 0.3 wt% Type I collagen: 0.3wt% $CaCl_2$: 3wt%	HUVECs H9C2
V. T. Duong et al., 2019. (123)	150-230	570-610	1160μm	Core: 0.12 ml min−1, Shell: 0.25 ml min−1 and 0.3 ml min−1	Alginate: 0.5 wt%, 1.5 wt% $CaCl_2$: 200 mM	NIH/3T3
V. T. Duong et al., 2018. (49)	200	340	580μm	Core: 0.12 ml min−1 Shell: 0.25 ml min−1	Alginate: 1.5 wt% $CaCl_2$: 200 mM	NIH/3T3
G. Gao et al, 2018. (131)	853-247	-	14G/18G 17G/21G 19G/25G	-	Alginate: 2wt% VdECM: 3wt% $CaCl_2$: 0.1M	HUVECs hAECs Human HL-60

1.4.6. A novel microfluidic-based 3D-printing system

Researchers at the School of Dentistry have developed a new microfluidic-based device (fluidic chip or microfluidic chip), that can help overcome current challenges with printing vascular models for research and tissue engineering (110).

The fluidic chip made of PDMS is used for coaxial extruding of hollow hydrogel fibres with a shell (i.e., wall) and core (i.e., lumen) (**Figure 1.10**).

An acrylonitrile butadiene styrene (ABS) channel, printed using the Continuously Varied extrusion (CONVEX) method, is used as a mould to create a PDMS chip. Once the PDMS sets, the ABS channels are removed from the chip by dissolving them in acetone, leaving behind hollow channels, from which the solutions are extruded using extrusion pumps. The channels are reported to have a very low surface roughness from the inside which is very important to make sure the fluids can flow through easily and to avoid cells and materials getting accumulated in the rough edges of the channels from the inside (110,132). Additionally, the microfluidic-based chip overcomes low optical transparency and low-resolution limitations that were reported with previous systems, as well as a leak-free and seamless structure, with an improved surface finish (110).

The preliminary studies have shown the potential of this novel device to produce straight, wavy, and helical channels, similar to those found *in vivo*. Additionally, the chip shows potential to create a variety of blood vessel mimics with varying wall thickness, just by changing the flow rate of solutions through the inner channel. In this project, the novel microfluidic-based chip will be tested to observe its potential to create blood vessel mimics and identify areas of improvement to the printing process.

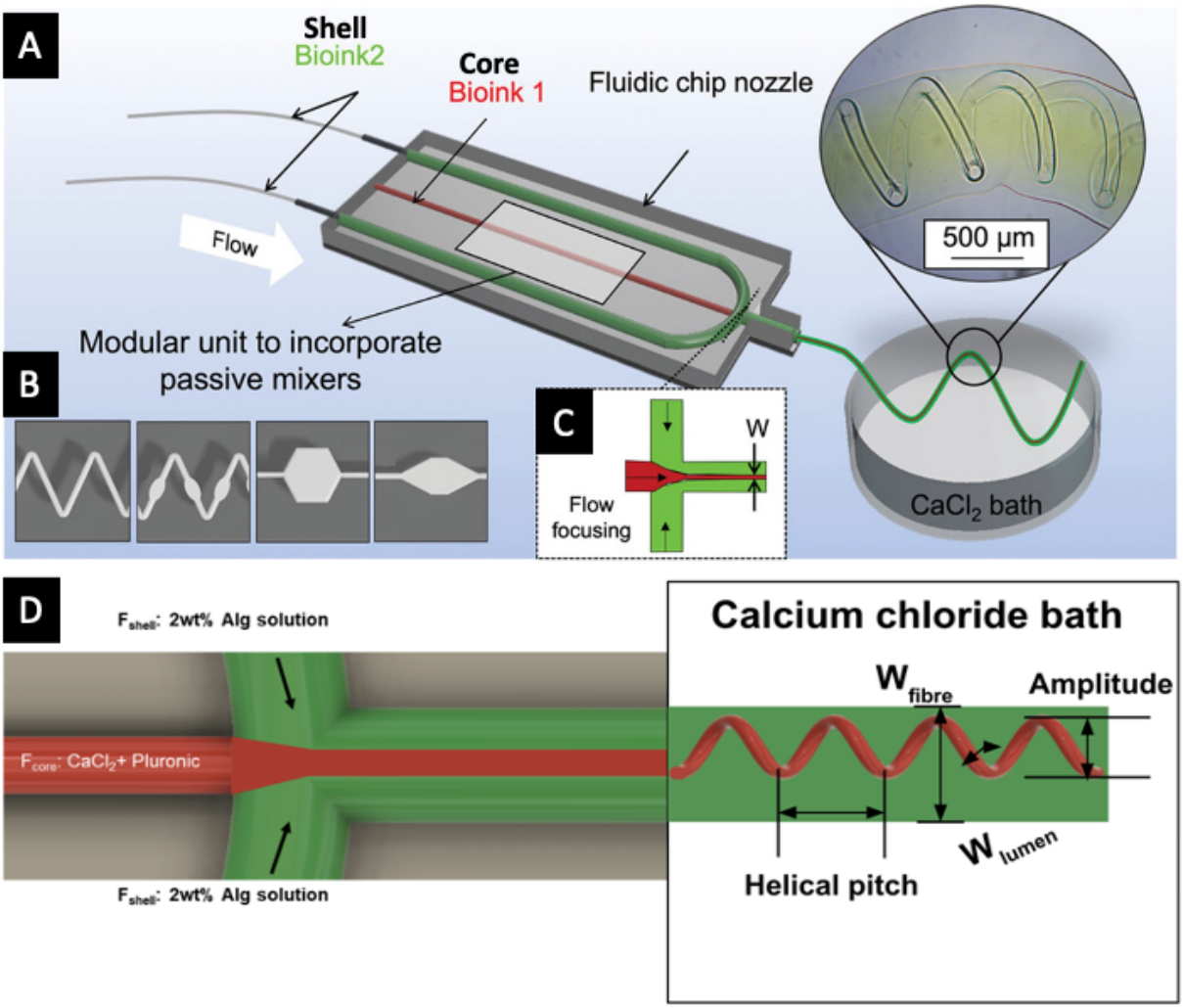


Figure 1. 10: A novel microfluidic-based extrusion device for constructing blood vessel mimics. A) Bioinks are extruded through the microfluidic-based nozzle into a $CaCl_2$ bath, forming helical core-shell fibres. **B**) The chip has the potential to be incorporated with a range of mixer channels for various studies. **C**) Flow focusing **D**) channels allow the extrusion of multiple materials at once. Channel sizes are 400 µm for core and 1000 µm for shell. Figure provided by Moetazedian et al. (2023) (110).

1.5. Summary

Perfusable vasculature models are in demand due to lack of oxygen and nutrients, as well as removal of waste from the cells inside the core of the tissue scaffold for tissue engineering, as this causes the reduced cellular activity and cell death (37,39). It is crucial to have perfusable networks through the hydrogel construct to provide essential materials for cells to maintain their metabolism until the tissue mimic has integrated into the host tissue (49,133). There are many different methods available to print blood vessel mimics, however, they have some drawbacks which the novel microfluidic-based chip, manufactured using the MEAM method, can overcome such as affordability to manufacture each chip because it is made of a cheap, readily available silicone called PDMS (110). In this study, hydrogel fibres with a variety of continuous core shapes, which can be perfused and have cells embedded, will be developed to further the progress in tissue engineering to meet the growing demand of organs required for bone transplantation.

1.6. Aim and objectives

Aim

The aim of this research project is to investigate the efficacy of a novel microfluidic-based chip for fabricating hollow cell-compatible fibres, which are structurally adjustable, durable and can be perfused to mimic physiological blood flow for tissue engineering purposes.

Objectives

The following objectives have been identified to achieve the project's aim:

1. Investigate the range of hollow core-shell fibres that can be generated with a defined width and geometry by changing the extrusion flow rates of core (**section 3.2.1.**).
2. Assess the cytotoxicity and alginate cross-linking capabilities of varying concentrations of $CaCl_2$ in the bath solution, to identify the concentration with maximum cell viability and structural integrity of the fibre (**section 3.2.2.**).
3. Determine the optimal concentration of gelatine required to achieve the desired cell adhesion and viability, while ensuring hollow core-shell fibre formation (**section 3.2.3.**).
4. Evaluate the impact of extrusion method, material composition and prolonged culture on cell viability of cells encapsulated in fibres with different structures (**section 4.2.1.**).

5. Investigate the influence of storage and incubation conditions on fibre degradation and morphology (**section 4.2.2.**).
6. Perfusion of hollow fibres, using gravity, to confirm the structural integrity and uniformity of fibre's core for replicating blood flow (**section 5.2.1.**).
7. Explore the cannulation methods and loading of fibres on a chip to create a set-up that can potentially be used for testing the efficacy of fibres in future studies (**section 5.2.2.**).

2. Materials and Methods

2.1. Materials

Except where stated, all chemicals used in this project were purchased from Sigma-Aldrich®.

2.2. Methods

2.2.1. Preparation of solutions to generate and perfuse fibres

For the following, fresh solution was prepared whenever needed and was used within 2 weeks of preparation. Additionally, for cell culture studies, solutions were sterilised with 0.22 μm filter unit before use.

Sodium alginate

On a magnetic stirrer (Corning®), a glass bottle containing reverse osmosis (RO) water, and a stirring magnet, was heated to 80 °C. Sodium alginate was gradually added to the RO water, at a concentration of 2 wt% (20 mg/ml), while stirring. Tartrazine, a yellow dye, was also added to the solution at a concentration of 0.1 wt% (1 mg/ml), for visualisation. In this project, sodium alginate is also referred to as ‘alginate’ in some places for simplicity.

Pluronic solution

Pluronic solution was composed of Pluronic® F-127 and calcium chloride ($CaCl_2$), to a concentration of 30 wt% (300 mg/ml) and 2 wt% (20 mg/ml) respectively, in RO water. The solution was left in 4 °C fridge to dissolve overnight and thoroughly mixed on a magnetic stirrer before use. Erioglaucine disodium salt as

blue dye was also added to the solution at a concentration of 0.1 wt% (1 mg/ml) for visualisation.

$CaCl_2$ bath solution

Bath solution for extrusion of fibres was prepared for by dissolving $CaCl_2$ in RO water or cell culture media at concentrations of 2 wt% (20 mg/ml), 4 wt% (40 mg/ml) and 10 wt% (100 mg/ml).

Gelatine-alginate blends

For making gelatine-alginate blends, gelatine (Bovine skin, Type B) was added to 2 wt% sodium alginate at following concentration: 2 wt% (20 mg/ml), 6 wt% (60 mg/ml) and 10 wt% (100 mg/ml).

Blue dye for perfusion

Erioglaucine disodium salt was mixed with RO water at a concentration of 0.2 wt% (2 mg/ml). This blue dye solution was used for perfusion studies.

2.2.2. Production of core-shell alginate fibres

2.2.2.1. Extrusion of core-shell fibres

The microfluidic-based chip was supplied by Moetazedian et al. (2023) (110). Sodium alginate solution was loaded into 2 plastic luer-lock syringes (Terumo®) and the Pluronic solution was loaded into a Hamilton 5 ml Gastight syringe (Hamilton®). These syringes were mounted onto the dual syringe pumps (IPS-14RS, Inovenso), and their inner diameter and volume was set up in the pumps' system according to **Table 2.1**.

Table 2. 1: Extrusion pump settings used for the syringes when printing core-shell fibres.

Syringe type	Inner diameter (cm)	Syringe volume (ml)
Plastic	14.5	10.0
Hamilton	10.3	05.0

Needles (22G size; Nordson EFD) were screwed to the syringes and plastic tubes (1/16″ outer diameter × 0.51 mm inner diameter; Darwin Microfluidics) were attached to the needles. The plastic tubes were inserted into the inlets of the microfluidics chip, 27 cm long tubes into the outer channels and a 25 cm long tube into the inner channel. Due to the narrow size of the inner channel, a small metal tube was used as a connecter between the plastic tube and the microfluidics chip's inner channel.

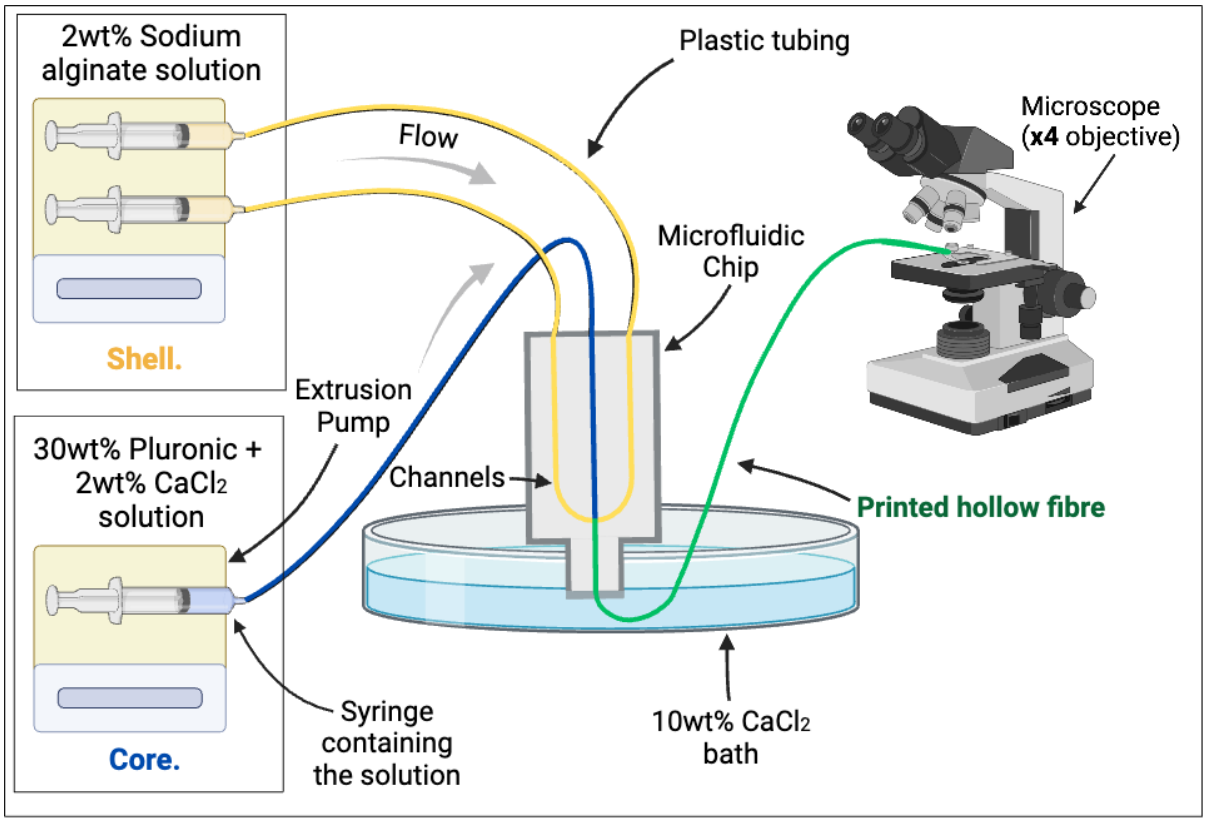


Figure 2. 1: Printing process of the core-shell fibres using the novel microfluidic chip. The Pluronic solution was extruded from the inner channel of the microfluidic chip, while sodium alginate was extruded from the outer channel, into the bath solution. The samples were imaged using a microscope. Created in BioRender.com.

The outlet of the microfluidic chip was held inside the bath solution contained in a petri dish (**Figure 2.1**). Flow rates were set according to **Table 2.2**, and 1.5 ml of solution was extruded from each syringe simultaneously. Once extruded, the resulting fibres were stored in a 4 °C fridge, within the bath solution, for at least 10 minutes. The procedure was repeated for all groups (1-6; **Table 2.2)** and three chips were tested individually.

Table 2. 2: Extrusion flow rates of solutions used for printing core-shell alginate fibres.

Group	Extrusion flow rate (µl.min^{-1})		Q_{shell}/Q_{core}
	Shell	**Core**	
1	2000	2000	1
2	2000	1500	1.3
3	2000	1000	2
4	2000	500	4
5	2000	250	8
6	2000	125	16

Throughout this procedure, the Pluronic solution was kept in a box with crushed ice to keep it in the liquid form and prevent gelling at room temperature (22 ± 2 °C). Hamilton syringe, its needle, tube and the microfluidic chip were placed in the same ice box, while not in use. An ice pack was kept on the syringe holder on the extrusion pump to keep that area cool. After extruding each fibre, the microfluidic chip and the tubing were flushed with cold water to remove excess Pluronic solution.

2.2.2.2. Width measurements

Carl Zeiss Primo Star microscope, attached to an iPad (2013, Apple), was used for capturing images of the fibres for structural analysis. Phase-contrast images, using a X4 objective, were taken on the Labscope app (Version 2.5, Zeiss). Three images were taken for each technical replicate. Fiji software was used for taking

length measurements of the fibre's width (see **Appendix A**) (134). For each image, five measurements were taken for each parameter, as shown in **Figure 2.2**.

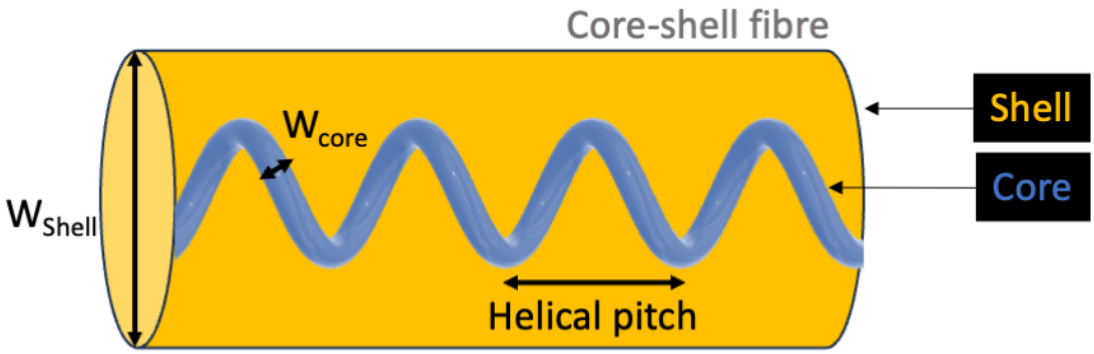


Figure 2. 2: Width and helical pitch measurements of core-shell fibre. Figure shows a core-shell fibre demonstrating how the helical pitch and width (W) measurements for each parameter were taken.

2.2.3. Standard tissue culture techniques

2.2.3.1. Cells and culture medium

Murine 3T3 fibroblasts (3T3s; ECACC 85022108) were used between passage number 24 and 38 throughout the course of this project. Cells were cultured in Dulbecco's Modified Eagle's Medium – high glucose (DMEM) supplemented to final concentrations of 10% foetal bovine serum (FBS; Gibco), 1 mM L-glutamine (L-glut; Thermo Fisher, UK), 100 U/ml penicillin and 100 µg/ml streptomycin (P/S; Gibco).

All cell culture solutions were stored in 4 °C fridge and pre-warmed in a 37 °C water bath (Grant Instruments, UK) prior to use. All plasticware and outer surface of containers were wiped down with 70% ethanol before moving into the Class II biological safety cabinet or laminar flow hood (Guardian MSC T1200, Monmouth Scientific, Bridgwater, UK).

2.2.3.2. Cell passage

In T75 flask, 3T3s were cultured in a 37 °C incubator and the cell culture media was refreshed every 2-3 days. An inverted phase-contrast microscope (AE 2000, Motic) was used to regularly monitor cell growth, and approximately every 3-4 days cells were passaged once 80% cell confluency was reached.

For harvesting, adherent cells in T75 were washed with 10 ml sterile phosphate buffered saline (PBS) to remove the FBS-containing cell culture media before adding 2.5 ml of trypsin-ethlyenediaminetetraacetic acid (trypsin-EDTA, 0.25% (v/v)) to detach the cell monolayer. Cells were incubated with trypsin for 3-4 minutes in the 37

°C incubator and then the flask was gently tapped from the side, with the palm of a hand, to detach any cells still partially attached to the surface of T75. After checking under the microscope for detachment of cells, trypsin was immediately diluted with the FBS-containing cell culture media. Cells were collected in a falcon tube and centrifuged (1000rpm, 3 minutes, 24 °C; Hettich®). After aspirating the media to remove trypsin, the cell pellet was resuspended in the fresh cell culture media and either used in experiments or passaged further.

2.2.3.3. Cell count

For determining cell number, e.g., for cryopreserving or seeding density for experiment purposes, cells were counted using a hemacytometer slide (Brand™). A 10 µl of cell suspension, in cell culture media, was mixed with 10 µl trypan blue in a 1:1 dilution, and vortexed. A 10 µl of that mixture was added underneath the glass cover slip of a hemacytometer. Under a microscope, the number of cells in each of the four hemacytometer grids were counted using a tally counter, averaged, and then calculated for seeding, using this formula: Number of cells in the 1 ml suspension = average number of counted cells x 2 (dilution factor) x 10^4. The appropriate number of cells were collected from the stock cell suspension for different purposes by following this calculation: Volume required (ml) = cell density of 1 ml cell suspension/cell density required.

2.2.3.4. Cryopreservation and thawing of cells

Cells were frozen using cryomedia that was composed of 70% DMEM (with P/S and L-glut), 20% FBS and 10% dimethyl sulfoxide (DMSO). The cell pellet was collected after trypsinizing and centrifuging the cells as described in **section 2.2.3.2.** The cell pellet was resuspended in the cryomedia and around $1x10^6$ cells/ml were prepared for cryopreservation. Cryovials (Fisherbrand) were gradually frozen in Mr. Frosty™ Freezing Container (Thermo Scientific™, Cat No: 5100-0001) in –80 °C freezer before moving them to the liquid nitrogen storage facilities (-196 °C), after 24 hours, for long-term storage.

Whenever required, cells were retrieved from the liquid nitrogen storage and thawed before resuspending in the fresh cell culture media. After centrifuging the cell suspension to collect a cell pellet, the media was discarded to remove DMSO. The 3T3s cell pellet was resuspended in fresh 7 ml cell culture media and cultured in a T25 flask for 3-5 days in a 37 °C incubator. Cell culture media was replaced every 1-2 days. After cells had adhered to the T25 flask and showed spreading and multiplying, the cells were passaged into T75 flasks as described in **section 2.2.3.2**.

2.2.4. Effect of bath $CaCl_2$ concentration on cell viability

To investigate the best concentration of $CaCl_2$ bath solution for cell-related studies, this experiment was carried out.

2.2.4.1. Fibre production

Extrusion equipment was sterilised with 70% ethanol and moved inside the laminar flow hood. The 3T3s were trypsinized and counted as described in **section 2.2.3.3.** The required amount of four cell suspensions were taken from the stock solution, containing $2x10^6$ cells/ml for each group (**Table 2.3**), and then centrifuged individually to collect a pellet. Media was carefully aspirated and discarded leaving behind 100 ±10 µl of cell culture media to mix the sodium alginate solution with.

Table 2. 3: List of $CaCl_2$ bath solutions, in supplemented cell culture media, tested for cell viability.

Group title	Description
2	2 wt% $CaCl_2$ bath solution
4	4 wt% $CaCl_2$ bath solution
10	10 wt% $CaCl_2$ bath solution

After mixing sodium alginate with the cells, solution was loaded into the plastic luer-lock syringe and mounted onto the extrusion pump. The 27 cm long plastic tube

was attached to the needle (22G size) of the syringe and 1.5 ml of the solution was extruded (flow rate: 2000 µl.min^{-1}) directly into a 15 ml bath solution. The bath solution was composed of supplemented cell culture media as a base with $CaCl_2$ added and sterilised using a 0.22 µm filter unit. Once the fibre was extruded, it was left in the bath for 30 minutes at room temperate (22 ± 2 °C). After the bath, the fibre was gently washed with RO water to remove excess $CaCl_2$, then cut into three 3 cm long pieces for each technical repeat. These fibre pieces were transferred to tissue culture plates (12-well; Thermo Scientific™). Supplemented cell culture media was added to each well at 2 ml and left to incubate in a 37 °C incubator. The same extrusion, bath and preparation steps were taken for all three (2, 4 and 10 wt%) test groups (**Table 2.3**). Samples were checked under the microscope before incubation to validate cells were homogenously distributed in the sodium alginate fibres.

2.2.4.2. Live/Dead assay

After incubation, a Live/Dead assay was carried out, using the LIVE/DEAD Viability/Cytotoxicity Kit (Invitrogen, Thermo Fisher Scientific, US), to measure viability of the cells embedded in the fibres and to assess the cells' morphology.

The staining solution for the assay was prepared as per the manufacturer's instructions, with a few variations in the staining steps. Calcein acetoxymethyl ester (Calcein-AM) at 2.5 µl and ethidium homodimer-1 (EtD-1) at 10 µl was added to 5 ml supplemented cell culture media. The falcon tube containing the solution was covered with tin foil for protection from light. A fresh solution was prepared every four hours, when needed.

Samples were taken out of the incubator and cell culture media was aspirated from the wells. Staining solution at 500 µl was added directly to the samples in the wells. The stain was added to three wells at a time, every 30 minutes, to prevent the cells from being over-exposed to stain while the first three samples were being imaged. After adding the stains, the plate was very gently agitated on an orbital shaker (10 seconds, x1 speed; Luckham) to allow the stains to mix evenly into the media and cells. The plates were covered with tin foil and incubated with the stains for 30 minutes at room temperature (22 ± 2 °C). After incubation, the staining solution was removed from the well, gently washed with fresh 500 µl media, and then replaced with 500 µl of fresh cell culture media to ensure the sample does not dry out during the imaging process.

Using a fluorescence confocal microscope (Zeiss LSM 700, Jena, Germany), stained samples were visualised. Wavelengths used were 488 nm for green channel and 555 nm for red channel. Images were saved in 16-bit, full resolution and .tif file format. The specific methods of image acquisition and processing, for cell viability assessment and measurement of the spreading area of a cell, are explained below.

Cell viability

For measuring the viability of the cells, three independent experiments were conducted, each consisting of three technical repeats per test group. For each technical repeat, at least three Z-stacks were captured (using the Zen 2011 application) at random locations of the samples, starting from one side of the fibre's wall and progressing perpendicularly to the other. The interval between Z-stacks was

maintained at 50 μm to avoid duplication of cells. The number of images per Z-stack varied between 6 and 27 (averaging 19) depending on the fibre's thickness. Some images were excluded during image processing due to high background noise that interfered with cell fluorescence and counting. The area of an image used for analysis was 1.63328 mm² (captured with a 5X objective lens).

Cell counts were performed using a custom automated macro in Fiji software (**Appendix B**). This macro processed images in sequence from each Z-stack. Briefly, an image was split into green (live cells) and red (dead cells) channels, and then converted into greyscale. Fiji's "3D Objects Counter" tool was employed to count cells in each image. The process was automated, repeating the counting of alive and dead cells for all images in the Z-stack folder. Results were recorded in a log file containing cell counts for each image.

The values generated by the Fiji macro were collated in an Excel spreadsheet. The following formula was used to calculate the percentage viability for each image:

$$\textbf{Cell viability}\ (\%) = \left(\frac{\textbf{Number of green-stained}\ (\text{alive})\ \textbf{cells}}{\textbf{Total number of cells}\ (\text{green-stained + red-stained})} \right) \times \mathbf{100}$$

Percentage values generated from the individual images were averaged for each z stack. Since the images were not taken consistently from the same location of the samples, the average viability values from Z-stacks per technical repeat were pooled across the three experiments. This method was chosen to minimize bias, especially if the cell viability might differ a lot across various regions of the same sample. By pooling the percentage values rather than averaging within the technical repeats, it

also allowed for statistical analysis on a larger data set for a more reliable p-value. The final pooled viability percentages were then analysed for statistical evaluation.

Spreading area of a cell

For analysing the average spreading area of a cell, one image was selected at random from each Z-stack (used for viability assessment), covering an area of 1.63328 mm² (captured with a 5X objective lens). The image was usually acquired from the fibre's centre when viewed cross-sectionally and from random locations of the sample. For each experimental repeat, three images were chosen. The scale of the image was set manually using Fiji's 'set scale' tool before applying the custom macro (**Appendix C**). Briefly, this macro split the image into green (alive cells) and red (dead cells) channels, but only the green channel was processed. The green channel was converted to greyscale, and a suitable threshold was applied. The cells in the image were masked, separated using the watershed tool if touching, and analysed to measure the surface area of each cell. The measurements (μm^2) were then collated into an Excel spreadsheet.

The spreading area (μm^2) for each cell was averaged with other cells within the same image. These averaged values were pooled across the three experimental repeats (x3 values each). As before, this method was selected to minimize bias, accounting for potential differences in cell size across various regions of the sample. Throughout the thesis, the average spreading area of a cell (μm^2) is also referred to as 'cell area' particularly in **Figure 3.9** and **3.12.**

2.2.4.3. Width measurements

The fibres were imaged, and the data were processed as described in **section 2.2.2.2**.

2.2.5. Effect of polymer composition on fibre formation - blends with gelatine

2.2.5.1. Cell attachment and morphology test

To investigate if the cells attach to the surface of gels after 24 hours of incubation on different gelatine blends, including the alginate-only group, the following experiment was carried out.

Transwell inserts (transparent membrane, pore diameter: 0,4 μm, Greiner Bio-One Thincert) were used to hold the blends and were placed inside the 12-well plates. $CaCl_2$ bath solution (supplemented DMEM as a base) was added into each of the plate's well at 1 ml. Solutions were added to their specific transwell inserts (**Table 2.4**). After 30 minutes of incubation in the 37 °C incubator, $CaCl_2$ bath solution was removed from the wells, washed with PBS and replaced with 1 ml of the supplemented cell culture media. The Negative group was used as a control which had no gel present, and the cells were seeded directly on the transwell's surface.

Table 2. 4: List of different compositions of alginate-gelatine blends tested for investigating cell response to the material.

Group	Gelatine	Sodium alginate
0	Not added	2 wt%
2	2 wt%	2 wt%
6	6 wt%	2 wt%
10	10 wt%	2 wt%
Negative	Not added	Not added

Cells were trypsinized and counted as described in **section 2.2.3.3**. The required amount of cell suspension was taken from the stock solution, containing $1x10^5$ cells/ml, and then centrifuged to collect a pellet. After mixing the cells with the fresh cell culture media, 1 ml of the cell suspension was seeded on top of the gels in the transwells. The samples were incubated in the 37 °C incubator.

2.2.5.2. Viability and morphological analysis

After 24 hours of incubation, samples were observed under a light microscope to ensure there were cells present on the gels before staining was carried out. Subsequently, to measure viability, spreading area and amount of cells attached to the gel's surface, the samples were stained using the LIVE/DEAD Viability/Cytotoxicity Kit and visualised using the fluorescence confocal microscope, as described in **section 2.2.4.2.**

Cell viability

For measuring the viability of the cells, three independent experiments were conducted, each consisting of three technical repeats per test group. For each technical repeat, at least three individual images were captured at random locations of the samples. The area of an image used for analysis was 1.63328 mm² (captured with a 5X objective lens).

Cell counts were performed using a custom automated macro in Fiji software (**Appendix B**). The individual images for each test group were compiled into one

folder. This is because the macro is designed to process multiple images in sequence, for the purpose of ease and saving time. The cell counts and viability calculation method is described in **section 2.2.4.2.** under '**Cell viability**'. Percentage values generated from the individual images per technical repeat were pooled across the three experiments. As mentioned previously, this method was chosen to minimize bias and to get a more reliable p-value.

Quantification of attached cells

Cell attachment means the percentage of cells attached to the test material (i.e., gel made up of alginate-gelatine blend) for each test group, relative to the Negative control.

The same values generated previously for '**Cell viability**' (**section 2.2.5.2.**) were used to determine the amount of cells attached in test samples compared to the control group, after 24 hours of culture. For each experimental repeat, the total number of green-stained (alive) cells in the Negative group were averaged across all images within that repeat. This average was then used as a reference for comparing the amount of green-stained (alive) cells present in the test sample images.

The percentage of cells present in each image, for the test groups, was calculated using this formula:

$$\textbf{\% cells attached} = \left(\frac{\textbf{Number of green-stained cells in an image (of a test group, i.e., 0, 2, 6 and 10 wt\%)}}{\textbf{Average number of green-stained cells in Negative control}} \right) \times \mathbf{100}$$

For statistical analysis, the percentage values for individual images were pooled across the technical repeats in each experiment, with a minimum of 3 values per technical repeat. As mentioned previously, this method was chosen to minimize bias and to get a more reliable p-value.

Throughout the thesis, the percentage of cells attached to the material (relative to Negative control group) is also referred to as '% cell attachment' particularly in **Figure 3.11 B**.

Spreading area of a cell

For analysing the average spreading area of a cell, one image was captured for each technical repeat, covering an area of 1.63328 mm² (captured with a 5X objective lens). Images were taken from random locations of the samples (x3 per technical repeat). After applying the custom macro (**Appendix C**), the raw values for area of each cell within an image were collected in an Excel spreadsheet. These spreading area values (μm^2) for each cell were averaged with other cells within the same image. Averaged values for the area of cells for each image were then pooled across the three experimental repeats. As mentioned previously (**section 2.2.4.2.**), this method was chosen to minimize bias and to get a more reliable p-value.

2.2.5.3. Extrusion of fibres

To investigate if the core-shell fibres still form if gelatine is added to the sodium alginate in the shell, this experiment was carried out. Another aim was to measure

the width of the fibre's core and shell to check if there was a difference compared to control, for different gelatine fibres (**Table 2.5**).

As described in **section 2.2.2.1.**, solutions for the shell and core of the fibre were loaded into the syringes and mounted on extrusion pumps. Microfluidic chip was attached to the end of the tubes and materials were extruded at the flow rate of 2000 µl.min^{-1} for the shell and 1500 µl.min^{-1} for the core into the 10 wt% $CaCl_2$ bath solution. A 1.5 ml of solution was extruded from all three syringes simultaneously. Once the fibres were extruded, they were left in the bath for 30 minutes, then transferred to a petri dish containing RO water to gently wash and remove excess $CaCl_2$. After a gentle wash, fibres were transferred to fresh RO water. The same steps were repeated for all test groups.

Table 2. 5: Different concentrations of gelatine was mixed with sodium alginate to make alginate-gelatine blends.

Group	Gelatine	Sodium alginate
0	0 Not added	2 wt%
2	2 wt%	2 wt%
6	6 wt%	2 wt%
10	10 wt%	2 wt%

2.2.5.4. Width measurements

The fibres were imaged, and the data were processed as described in **section 2.2.2.2.**

2.2.6. Prolonged (28-day) culture and storage of fibres

2.2.6.1. Preparation of cell-encapsulated fibres

To test if the viability of cells when embedded and cultured in hydrogel fibres of different material compositions over time and if there was a change in fibres' stability, a 28-day experiment was carried out. Cell viability was tested on Day 1, 7, 14, 21 and 28 of fibre's extrusion. Composition of materials and fibre types tested are listed in the **Table 2.6**.

Table 2. 6: Types of cell-encapsulated fibres tested for prolonged 28-day cell culture and the composition of materials that were used for each fibre.

		Shell (wt%)		Core (wt%)	
Group	**Fibre type**	**Sodium alginate**	**Gelatine**	**Pluronic**	**$CaCl_2$**
A	Solid	2	0	(No core)	
B	Core-shell	2	0	30	2
C	Core-shell	2	2	30	2

Fibres for the solid group were prepared, with 3T3s embedded, as described in **section 2.2.4.1**. Fibres for the core-shell group were prepared as described earlier in **section 2.2.2.1.**, with some changes. Briefly, 3T3s were trypsinized and a pellet was collected. Shell solution was mixed with cell suspension at a final concentration of $2x10^6$ cells/ml for each technical replicate. After loading the shell and core solutions into the syringe pump, with the microfluidic chip, the solutions were extruded into a

10 wt% $CaCl_2$ bath solution (cell culture media as a base). Flow rates for the shell solution was 2000 µl.min^{-1} and for the core it was 1500 µl.min^{-1}. A 1.5 ml of the solutions were extruded simultaneously from each syringe. Once the fibres were extruded, they were left in the bath for 30 minutes then washed with sterile RO water. Fibres were transferred to fresh cell culture media.

For each group, three technical replicates were prepared. Technical replicate refers to one continuous fibre extruded in a fresh bath solution. This one fibre was cut into five 3 cm long pieces for each time point. These fibre pieces were transferred to 12-well tissue culture plates. 1 ml of supplemented media was added to each well and left to incubate in 37 °C incubator. Cell culture media was changed three times a week. After incubation, Live/Dead assay was carried out to measure viability of the cells embedded in the fibres, for each time point.

2.2.6.2. Cell-free core-shell alginate fibres for different culture conditions

To investigate the stability of the fibres incubated in different compositions of culture medium and temperature over time, a long-term 28-day test was carried out. Measurements were taken on Day 0, 1, 7, 14, 21 and 28 of fibre's extrusion (**Table 2.7).**

Table 2. 7: The composition of incubation medium and temperatures that were used for testing the stability of core-shell alginate fibre over a 28-day period.

Group	Composition of medium	Incubation temperature
A	Supplemented DMEM and FBS	37 °C
B	Supplemented DMEM and no FBS	37 °C
C	RO water	37 °C
D	RO water	4 °C

Core-shell fibres were prepared as described earlier in **section 2.2.6.1.**, with minor changes. No cells were embedded in the fibres for this experiment. Core-shell fibres with Pluronic solution as the core and 2 wt% sodium alginate as the shell was tested only (**Table 2.8**).

Table 2. 8: The composition of core-shell alginate fibre for testing its stability over a 28-day period.

	Shell (wt%)	Core (wt%)	
Fibre type	**Sodium alginate**	**Pluronic**	**$CaCl_2$**
Core-shell	2	30	2

After extrusion and preparation of the core-shell alginate fibre, as described in **2.2.6.1.,** 3 cm long pieces for each time point were transferred to 12-well tissue culture plates. Media (1 ml), according to **Table 2.7**, was added to each well and left to incubate at the specific temperature for that group. Media was changed three times a week.

2.2.6.3. Cell viability and morphological analysis of the cell-encapsulated fibres

After 24 hours of incubation, Day 1 samples were observed under a microscope to ensure there were cells present in the wells before staining was carried out. Subsequently, to measure cell viability and morphological analysis, the samples were stained using the Live/Dead assay, imaged and processed using the same procedure described in **section 2.2.4.2.**, except the Z-stacks interval, which was increased to 100 µm. The same steps were carried out for other samples at their specific time points. For instance, Day 7 plate was imaged after seven days of incubation and so on.

2.2.6.4. Observation of the fibres' stability

Stability of the fibres was observed qualitatively on Day 0, 1, 7, 14, 21 and 28 of extrusion by taking images of fibres using the phase-contrast microscope. Additionally, for **section 2.2.6.2.** only, phone camera images of the fibres were also taken.

2.2.6.5. Width measurements of fibres

As described in **section 2.2.2.2.**, each piece of fibre was imaged and processed for core and shell width measurements on Day 0 for all time points. Then for each timepoint (Day 1, 7, 14, 21 and 28) samples were imaged again.

2.2.7. Perfusion of core-shell fibres

The methods below describe the different attempts for perfusing core-shell fibres.

Siphoning effect

To test the perfusion of core-shell alginate and gelatine fibres, created in **sections 2.2.2.1.** and **2.2.5.3.**, siphoning (use of gravity) method was carried out (**Figure 2.3**). One end of a 24 cm long core-shell fibre was placed inside a falcon tube (50 ml; Falcon™) containing blue dye and the other end was sticking out from the falcon tube and put into a petri dish containing RO water.

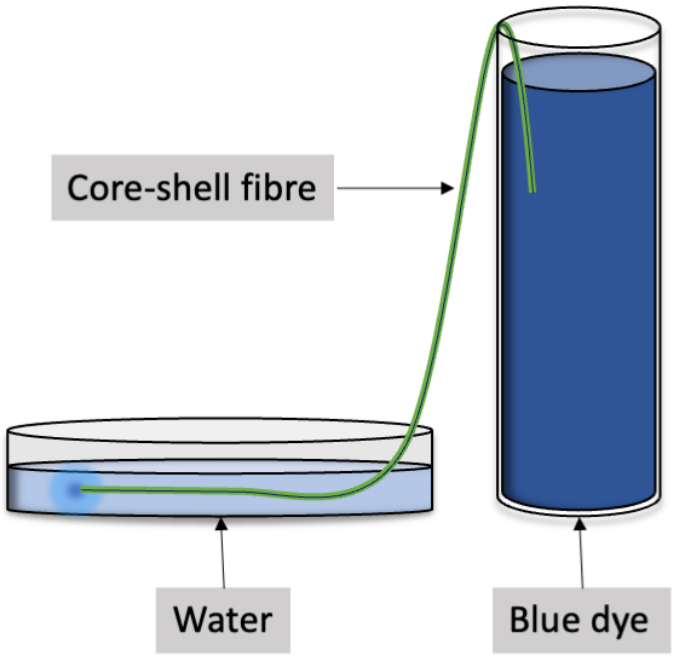


Figure 2. 3: Siphoning method to perfuse fibres. The diagram illustrates the set-up for perfusing fibres with blue dye, using the siphoning method.

Cannulation with needles

A needle (30G size; Nordson EFD) attached to a Hamilton 1 ml Gastight syringe (Hamilton®), containing blue dye, was used for cannulating the fibre. A dissection microscope (Wild Heerbrugg, Switzerland) was used to facilitate the cannulation of fibre's core.

Ibidi channels

A core-shell fibre was threaded through the channel of ibidi slides (sticky-Slide I Luer, ibidi®, Germany) with ends coming out of the two reservoirs. The slide was placed in a petri dish, turned upside down, and 30 wt% Pluronic solution (no $CaCl_2$ added) was poured into the two reservoirs and base of the slide for fixing the fibre in place. A polymer cover slip (ibidi®) was stuck to the bottom-side of the ibidi slide to secure the fibre and Pluronic solution in place. A needle (27G size; Monoject™), connected to a Hamilton 1 ml Gastight syringe (Hamilton®) containing blue dye, was used for cannulating the fibre.

2.2.8. Statistics

All statistical analysis in this project was performed using GraphPad Prism (version 8 for Windows, GraphPad Software, Boston, Massachusetts USA). The main types of analyses used are regression analysis and one-way ANOVA with post-hoc tests where appropriate. Linear regression was carried out for line graphs. In case of one-way ANOVA, Shapiro-Wilk test was carried out to determine whether or not the data were skewed. For skewed data, non-parametric (Kruskal-Wallis) test was carried out, followed by Dunn's multiple comparisons test. For normally distributed data, one-way ANOVA was carried out followed by Tukey's multiple comparisons test. The analyses performed for particular data sets are indicated in the relevant figure legend in **Chapters 3** and **4**.

Generally, the values processed from raw data were averaged within technical repeats, and then within experimental repeats, before any statistical analysis was performed (n=3). However, for some figures, the individual values processed from raw data were pooled across experimental repeats, to perform statistics on (n≥3). Sample size and the specific data processing method used for each results figure are mentioned in **sections (2.2.4.2 & 2.2.5.2)** of **Chapter 2**, and figure legends in **Chapter 3** and **4**.

3. Fabrication of biomimetic core-shell fibres

3.1. Introduction

The blood vessel mimic for tissue engineering need to recapitulate the complex structure and function as closely to the blood vessels as possible, in order to function properly when used in regenerative medicine (106,135,136). It needs to have a shell (i.e., vessel wall) and a core (i.e., lumen) to be able to recapitulate the basic structure of blood vessel. Moetazedian et al. (2023) created a chip, based on microfluidic system, for fabrication of hollow core-shell fibres that mimic the structure of blood vessel (110). A range of core shapes from straight, wavy and helical can be generated by varying the flow rates of the inner channel. In this section, the flow rates used for extruding the hydrogel fibres in the paper will be repeated to test the reproducibility and understand the process of the core-shell fibre generation.

Moetazedian et al. (2023) used 10 wt% concentration of $CaCl_2$ (45 mM of Ca^{2+} ions) in the bath solution to fabricate alginate hydrogel fibres (110). Extracellular Ca^{2+} concentrations of 1.1 – 1.3 mM are considered safe for normal cell functions and increase or decrease in this concentration can lead to cell death (137). Therefore, lower than 10 wt% concentrations of $CaCl_2$ need to be investigated that are biocompatible to cells, while still maintaining the integrity of the fibres. In 3D-printing, a range of $CaCl_2$ concentrations have been tested (126,129,131). An experiment will be carried out to assess the cytotoxicity of $CaCl_2$, used in the bath solution, on cells embedded in the hydrogel fibres.

Alginate, despite being biocompatible, is a non-adhesive biomaterial due to the lack of cell-interactive domains on its surface which prevent the cells to form

attachment links to the material (116–118). Although this might seem like a negative thing, instead the ‘blank slate’ nature of the sodium alginate provides the opportunity to modify its structure to design a hydrogel with specific properties for eliciting desired biological and mechanical outcomes in a highly regulated way (116). Gelatine is a commonly used material to promote cell attachment and viability when mixed with sodium alginate (138–140). The concentrations of gelatine blended with sodium alginate in the literature range from 1 wt% to even 20 wt% (87,126,141,142). Therefore, in this chapter, alginate will be blended with a broad range of gelatine concentrations to improve its adhesive properties, while ensuring that core-shell fibres are still formed. The use of gelatine to improve cellular response to shell material was also chosen due to the simple, cost- and time-effective preparation steps required, which are physical mixing with the alginate in water, unlike other methods such as arginine–glycine–aspartic acid (RGD) conjugation (143,144). Gelatine from bovine source was used in this project instead of porcine gelatine, which is widely used in 3D-printing (145–148). This is because the use of porcine-derived materials is prohibited in some religions, and since the final scaffolds will be implanted within patients, it is better to use bovine gelatine to facilitate patient care by providing alternatives to other blood vessel mimics that use porcine-derived gelatine (143,145,149–151).

Consequently, the overall aim of this chapter will be to optimise the fabrication process of hollow core-shell fibres to replicate the complexity of blood vasculature, while determining the optimum concentrations of materials required to promote cell biocompatibility.

3.2. Results

3.2.1. Effect of extrusion flow rate on core-shell alginate fibres' geometry

3.2.1.1. Core-shell alginate fibres with a range of core geometry can be generated

Extrusion of core-shell alginate fibres

The extrusion process is demonstrated in **Figure 3.1 A**. The microfluidic chip's nozzle was submerged in the 10 wt% $CaCl_2$ bath during extrusion. The solutions were extruded into the bath which formed into a hydrogel fibre through crosslinking of alginate polymers with Ca^{2+} ions in the bath. The $CaCl_2$ in the Pluronic solution gelled the alginate solution from the inside, while the $CaCl_2$ present in the bath solution gelled the fibre from outside as the partially gelled alginate solution was extruded out of the chip's nozzle. The use of dyes helped with the visualisation of the printing process. Pluronic and $CaCl_2$ (blue) solution was clearly seen to be concentrated in the middle of the fibre with sodium alginate (yellow) solution surrounding it from the sides. The images in **Figure 3.1** show that the fibre could be printed continuously. In **Figure 3.1 B**, the change in colour of the bath from clear to green showed the dye leaking out of the fibres. **Figure 3.1 B** shows that gelled fibres (green) with continuous length could be extruded in a controlled manner. The results in **Figure 3.1** clearly demonstrate the feasibility of employing 3D-printed microfluidic chip to produce core-shell alginate fibres.

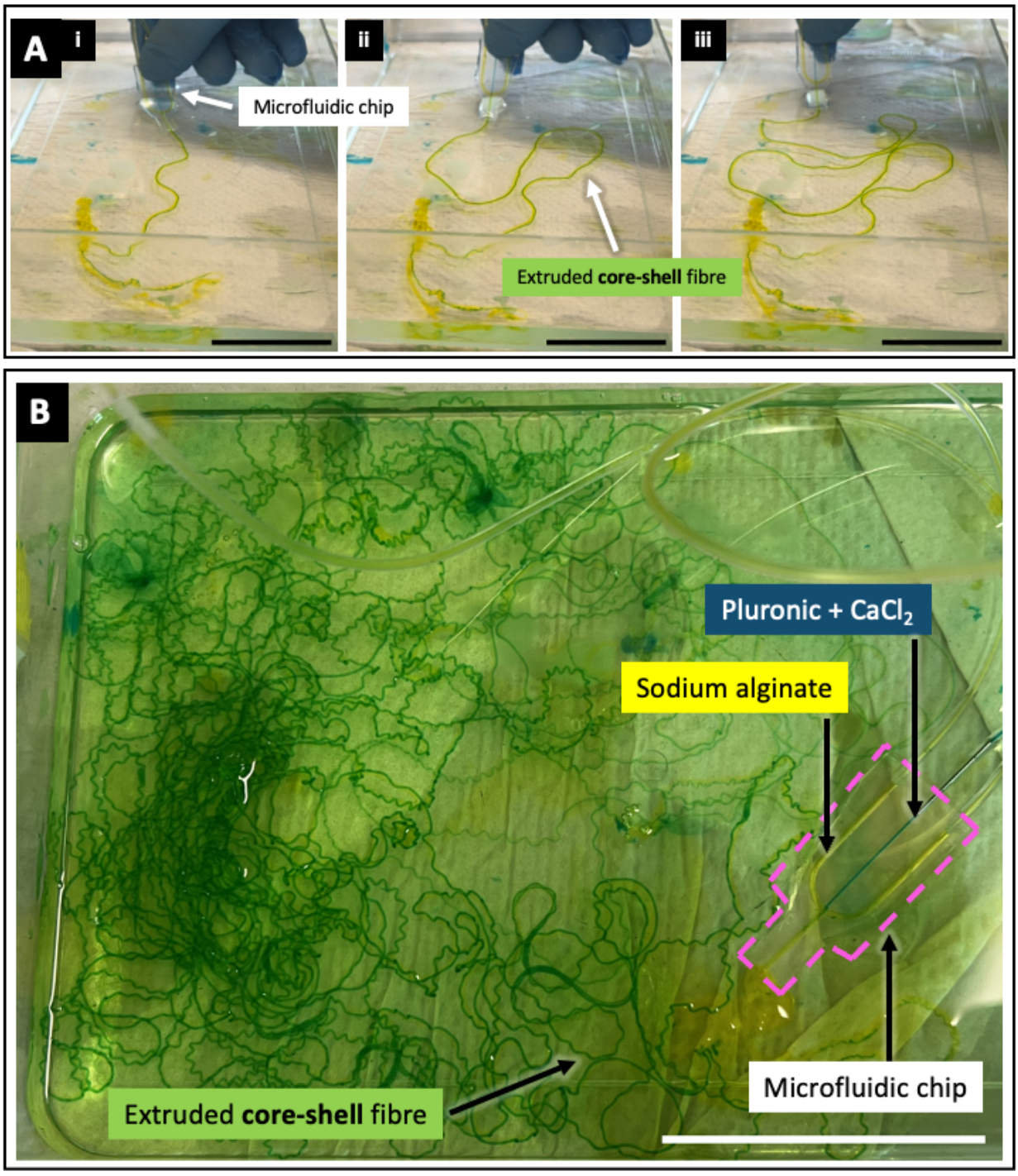


Figure 3. 1: Photographic images of the fibre extrusion process using the novel microfluidic chip. Ai-iii) Timelapse images of the fibre extrusion process. **B)** Image demonstrating that a very long fibre could be printed in one go. Yellow and blue dyes were used for visualisation of the fibres. Scale bar: 5 cm.

A range of core geometry can be generated

A set of images in **Figure 3.2** depict the range of core shapes that can be generated, using the microfluidic chip, when the solution flow rate for shell is kept constant at 2000 $\mu l.min^{-1}$ while the flow rate of core is changed within the range of 2000-125 $\mu l.min^{-1}$. **Figure 3.2** highlights the key words used in describing these fibres, with outer green lines highlighting the shell of the fibre and blue lines highlighting the core of the fibre.

From images in **Figure 3.2 B-D**, three distinct core shapes can be identified: straight, wavy and helical. Firstly, **Figure 3.2 B** shows fibres with straight core that have linear and uniform morphology along the length of the fibre's wall. Some fibres had core lining the fibre in the centre and almost evenly distributed in with the fibre's wall (**Figure 3.2 Bi**) but in some straight core fibres, the core was closer to one wall of the fibre and away from the other (**Figure 3.2 Bii**). Secondly, **Figure 3.2 C** shows wavy core structures, where the core of the fibre was not straight and uniform along the fibre's shell and showed periodic undulations and bends. Lastly, **Figure 3.2 D** shows a range of core shapes with bending and twisting patterns along the length of the fibres. From the 'Helical' images in **Figure 3.2 D**, the bend in the core seemed to be created through the core continuously touching the fibre's edge on one side and zigzagging to the opposite side of the fibre's edge.

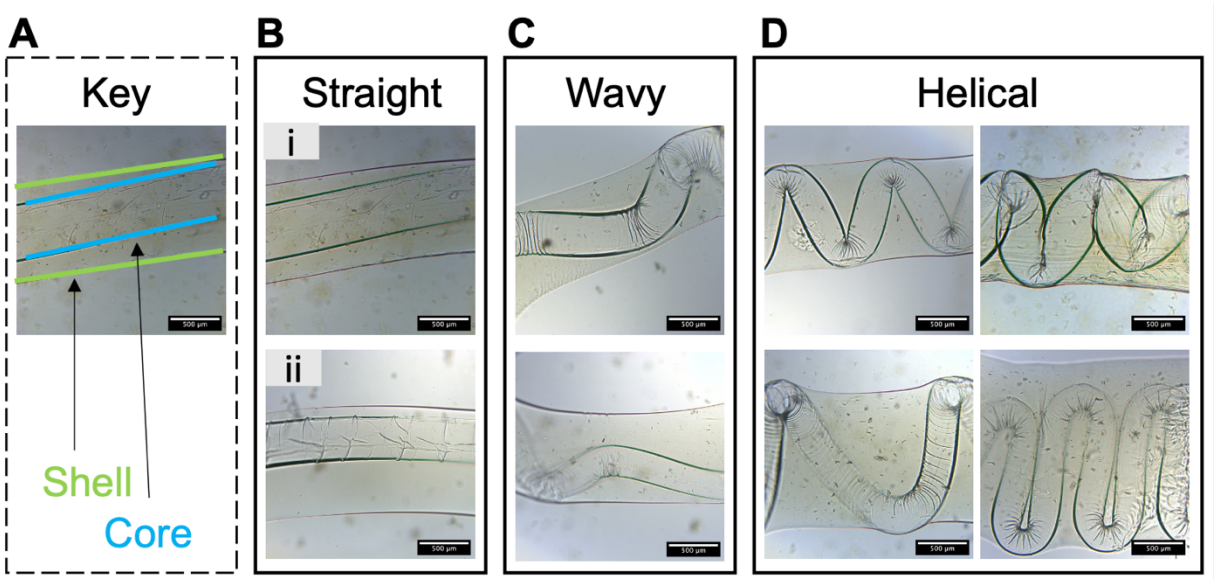


Figure 3. 2: Photographic images demonstrating fibres with a range of core structures that can be printed by changing the ratio between shell and core extrusion flow rates. A) Keywords to describe the structure of the fibre. Green lines indicate the shell of the fibre and blue lines highlight the core of the hollow hydrogel fibre. **Bi & ii)** Fibres with a straight core. **C)** Wavy core shapes. **D)** Fibres with a range of helical core shapes that are loosely and densely packed inside the fibre. The range of flow rates used for printing these fibres for the shell was kept constant at 2000 µl.min^{-1} while the flow rate of core was decreased from 2000-125 µl.min^{-1}. Scale bar: 500 µm.

3.2.1.2. Extrusion flow rate of core solution impacts the width of fibre's core and shell

Photographic images in **Figure 3.3** show that transparent fibres with distinct core shapes could be printed using core flow rates of 2000 µl.min^{-1} (**Figure 3.3 A**), 1500 µl.min^{-1} (**Figure 3.3 B),** 1000 µl.min^{-1} (**Figure 3.3 C**), 500 µl.min^{-1} (**Figure 3.3 D**), 250 µl.min^{-1} (**Figure 3.3 E**), 125 µl.min^{-1} (**Figure 3.3 F**) with a constant shell flow rate of 2000 µl.min^{-1}. The fabricated fibres were observed without the aid of a microscope. The fibres had a transparent core appearance, as observed against a black background. This transparency of the fibres made it easier to observe the

defined core inside the fibre. The images have been zoomed in (x4) (**Figure 3.3 A-Fii**) for the ease of visualisation in the figure, however, the translucent fibres with distinct core could be observed just with the naked eye (**Figure 3.3 A-Fi**).

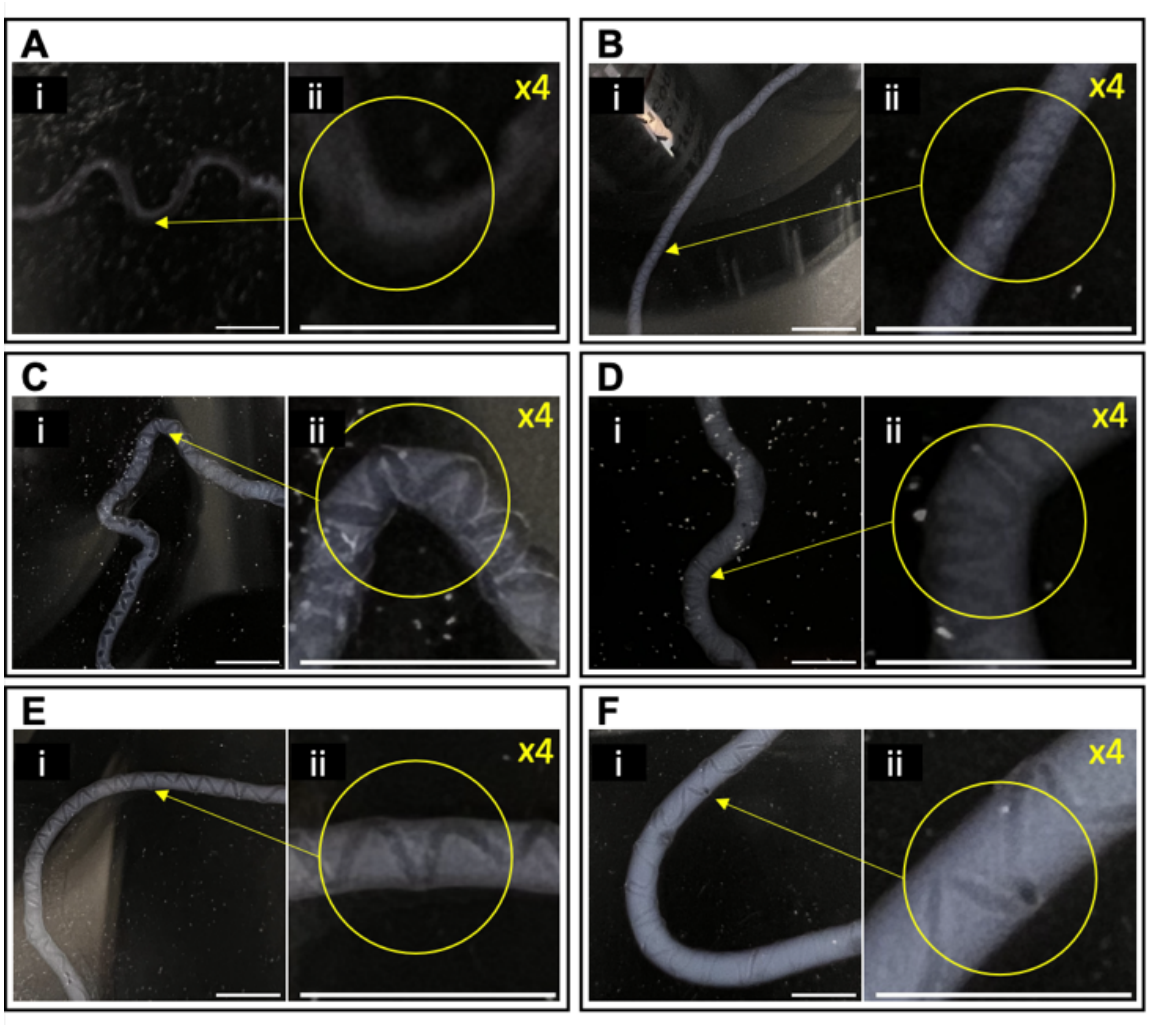


Figure 3. 3: Photographic images demonstrating the structure of fibres, as seen without a microscope. The demonstrated fibres were extruded using core flow rates of **A)** 2000 µl.min^{-1}, **B)** 1500 µl.min^{-1}, **C)** 1000 µl.min^{-1}, **D)** 500 µl.min^{-1}, **E)** 250 µl.min^{-1}, **F)** 125 µl.min^{-1} with a constant shell flow rate of 2000 µl.min^{-1}. Hollow alginate fibres could be printed with a range of core structures by changing the ratio of extrusion flow rates between shell and core. Specific areas of the fibres were zoomed in (x4) (**A-Fii**) from the original images (**A-Fi**), to clearly show the structure of the core. However, core of the fibres could be observed clearly with the naked eye as well. Scale bar: 5 mm.

Width of shell and core

The relationship between core solution flow rate and the two key parameters of hollow hydrogel fibres, shell and core width, is illustrated in **Figure 3.4**. The shell's width (green line), gradually decreased from 1345.10 ± 191.17 µm to 1062.07 ± 143.20 µm when the core flow rate was increased from 125-2000 µl.min^{-1}, which indicates a proportional reduction in the fibre's overall thickness. In contrast, the core (blue line) exhibited a gradual increase in width from 336.83 ± 26.95 µm to 684.14 ± 98.87 µm, which suggests a proportional growth in the width of the fibre's core. The opposite is true for both of these parameters when the core flow rate was decreased from 2000 - 125 µl.min^{-1}. Notably, the width values for both, shell and core, seemed to converge as the core flow rate increased from 125-2000 µl.min^{-1}. This convergence indicates that there is a possible relationship between the thickness of the fibre's wall and the changes in core flow rate when the flow rate of shell is kept constant at 2000 µl.min^{-1}.

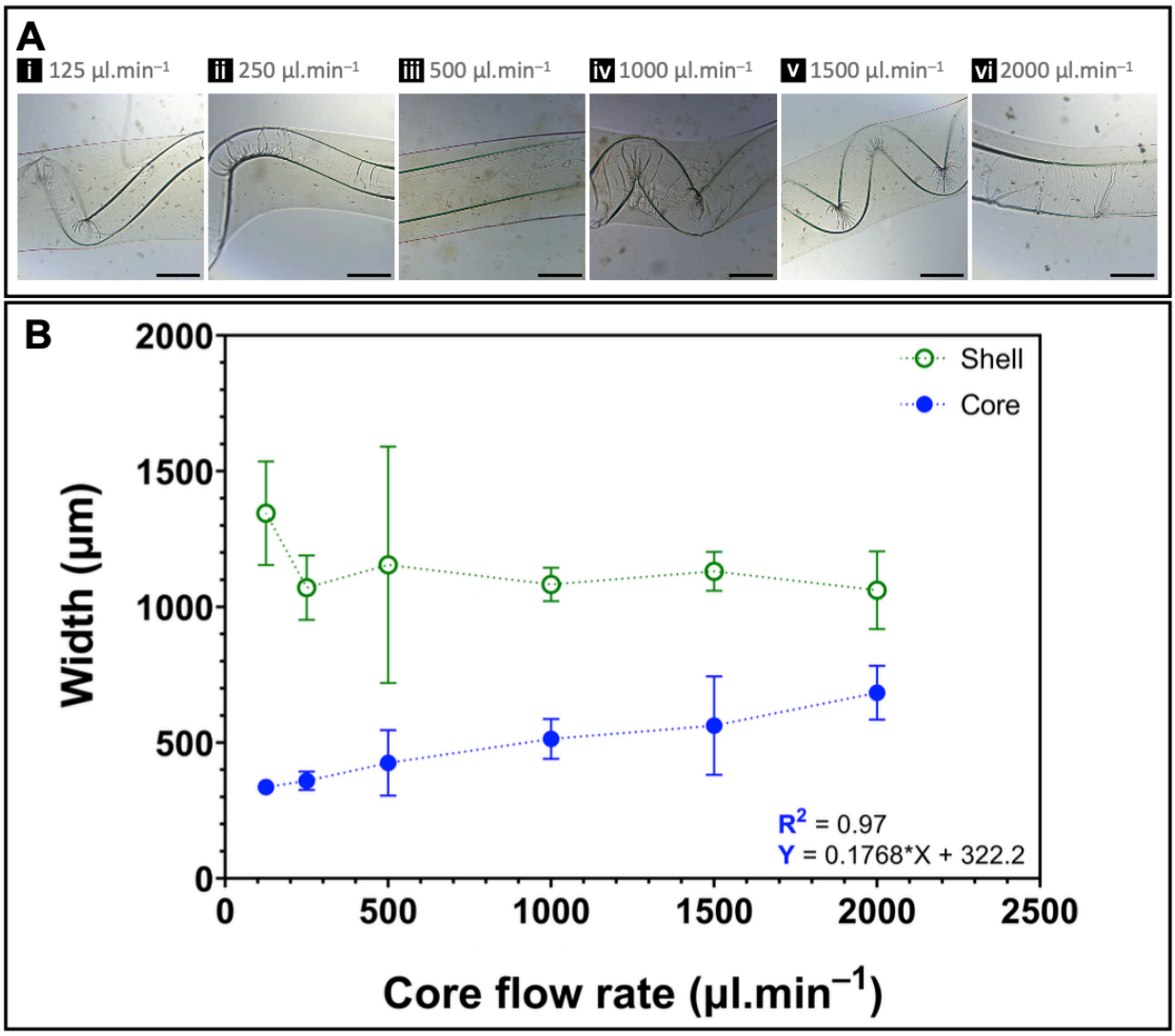


Figure 3. 4: Changes in the width of shell and core, of the alginate hollow fibre, in response to increase in the extrusion flow rate of core solution. Ai-vi) Phase-contrast images of the extruded core-shell fibres for each core flow rate, while the shell flow rate was kept constant at 2000 µl.min^{-1}. Scale: 500 µm. **B)** As the flow rate of core was increased from 125 µl.min^{-1} - 2000 µl.min^{-1}, shell width gradually decreased from 1345.10 ± 191.17 µm to 1062.07 ± 143.20 µm while the core width increased from 336.83 ± 26.95 µm to 684.14 ± 98.87 µm. Linear regression for core reported Y = 0.1768*X + 322.2. Data is shown as mean ± SD of three independent experiments. N = 3.

3.2.1.3. Impact of Qshell/Qcore on fibre's Wcore/Wshell and helical pitch

W_{core}/W_{shell}

The ratio of core width to shell width (W_{core}/W_{shell}) of hollow hydrogel fibres in response to increase in the extrusion flow rate (Q) ratio of shell and core solutions was tested. The flow rate of the shell (Q_{shell}) was kept constant at 2000 $\mu l.min^{-1}$ while the flow rate of core (Q_{core}) was decreased from 2000-125 $\mu l.min^{-1}$. The ratio of extrusion flow rates of shell and core solutions was plotted on the x-axis of the graph and the width of shell and core were measured, and their ratio was calculated and presented in the y-axis (**Figure 3.5**). Ratio of core width to shell width (W_{core}/W_{shell}) represents the relative size of the core in comparison to the overall fibre's width. A higher W_{core}/W_{shell} value indicates a wider core, while a lower ratio indicates a narrower core compared to the fibre width.

Relationship between W_{core}/W_{shell} and Q_{shell}/Q_{core} is shown in **Figure 3.5**. As the Q_{shell}/Q_{core} increased from 1 to 16, the W_{core}/W_{shell} decreased from 0.65 ± 0.097 to 0.27 ± 0.05. This indicates that the core width decreased as the extrusion flow rate of the core solution relative to the shell solution decreased. Conversely, as the extrusion flow rate of the core solution relative to the shell solution increased, it resulted in an increase in fibre's core size. These results demonstrate that fibres with thicker walls can be achieved by reducing the extrusion flow rate of the core solution in comparison to the extrusion flow rate of the shell solution, and vice versa.

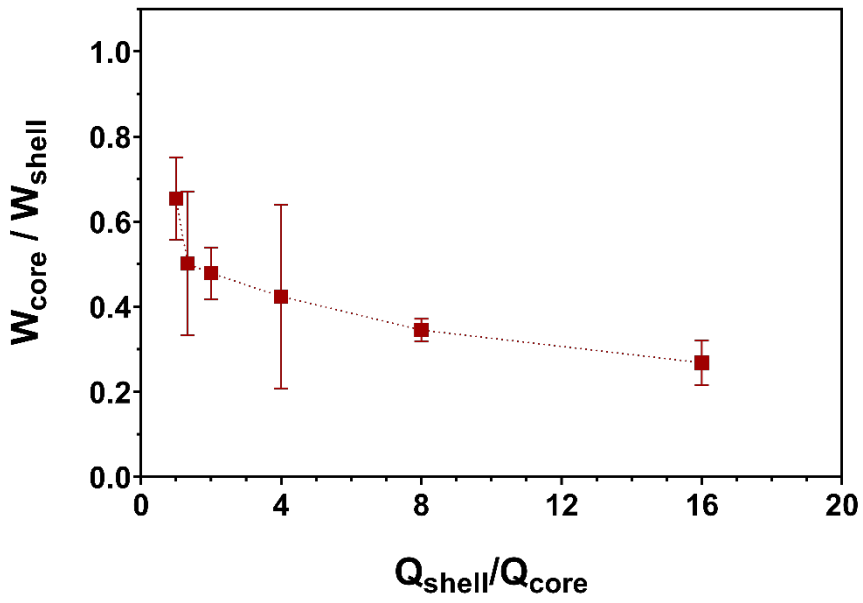


Figure 3. 5: W_{core}/W_{shell} of hollow alginate hydrogel fibres in response to increase in the extrusion flow rates (Q) ratio of shell and core solutions. The flow rate of the shell was kept constant at 2000 µl.min^{-1} while the flow rate of core decreased from 2000-125 µl.min^{-1}. W_{core}/W_{shell} (thickness of the fibre's wall) decreased from 0.65 ± 0.097 to 0.27 ± 0.05, as the Q_{shell}/Q_{core} (ratio between shell and core flow rate) increased from 1 to 16. Data is shown as mean ± SD of three independent experiments. N = 3.

Helical pitch

Relationship between the helical pitch (µm) of alginate fibre's core and increase in the extrusion flow rate (Q) ratio of shell and core solutions, from 1 – 16, is shown in **Figure 3.6**. Helical pitch represents the distance between consecutive bends in the helical structure of the core within a hollow hydrogel fibre. Higher the helical pitch value, the greater the distance between turns of the helix, while lower the helical pitch value, the narrower the distance between each turn of the core's helix.

From **Figure 3.6**, no clear relationship between ratio of flow rates (Q_{shell}/Q_{core}) and helical pitch can be observed. The data points are spread unevenly across the

graph, with large error bars (SD ranging between 289.38 and 634.73), as the Q_{shell}/Q_{core} increases from 1 – 16. This finding suggests that varying the extrusion flow rates to achieve a specific helical pitch cannot be predicted accurately at this point.

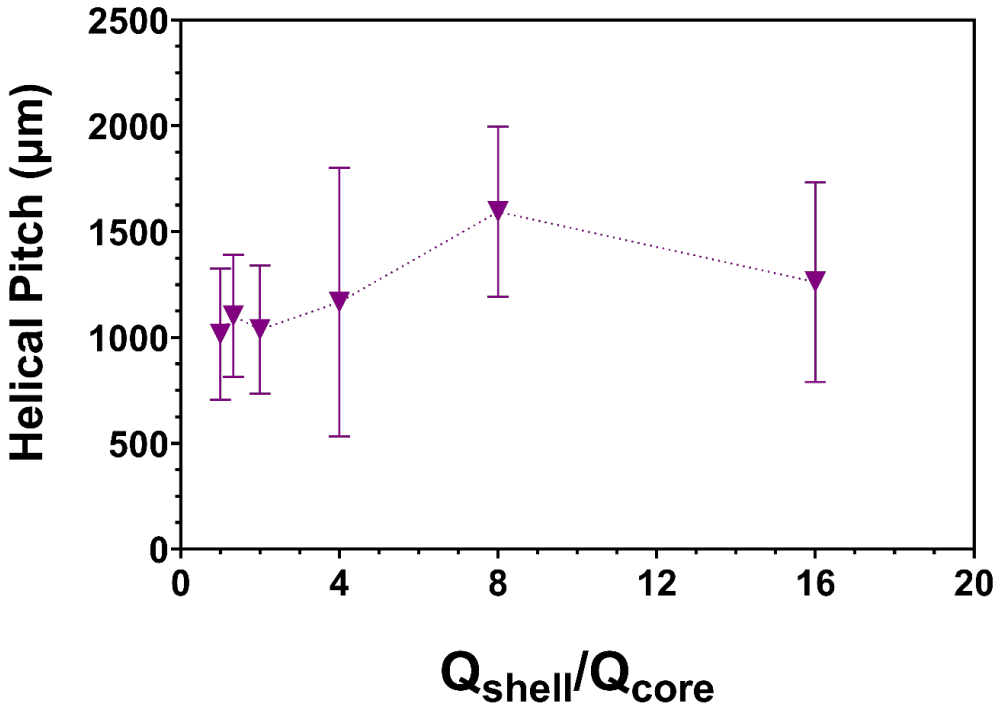


Figure 3. 6: Helical pitch of fibre's core in response to increase in the extrusion flow rates (Q) ratio of shell and core solutions. The flow rate of the shell was kept constant at 2000 µl.min^{-1} while the flow rate of core decreased from 2000-125 µl.min^{-1}. There was no distinct trend in the effect of Q_{shell}/Q_{core} on the helical pitch of fibre's core. Data are shown as mean ± SD of three independent experiments, representative of pooled measurements from multiple samples to account for measurements taken at random locations of each sample. N = ranges between 28 – 76.

3.2.2. Testing different concentrations of $CaCl_2$ in bath solution

3.2.2.1. Fibre width decreases with increasing $CaCl_2$ concentration

To investigate the influence of different concentrations of $CaCl_2$ in bath solution on fibre's width, 2 wt% solid alginate fibres were extruded into 2, 4 and 10 wt% $CaCl_2$ containing baths. **Figure 3.7 A (i-iii)** show phase-contrast images of fibres, confirming that alginate fibres can be printed in all test groups. A visual demonstration of fibres' size in comparison to each other shows that fibre printed in 10 wt% $CaCl_2$ appeared thinner than 2 wt% (by 31.61%) and 4 wt% (by 20.96%) fibres. **Figure 3.7 B** shows that the width of the shell gradually decreased from 1371.13 ± 115.74 μm to 1219.06 ± 96.67 μm as the concentration of $CaCl_2$ increased from 2 wt% to 10 wt%. Overall, **Figure 3.7** provides a comprehensive examination of the alginate fibres' thickness following printing in various concentrations of $CaCl_2$ bath solutions.

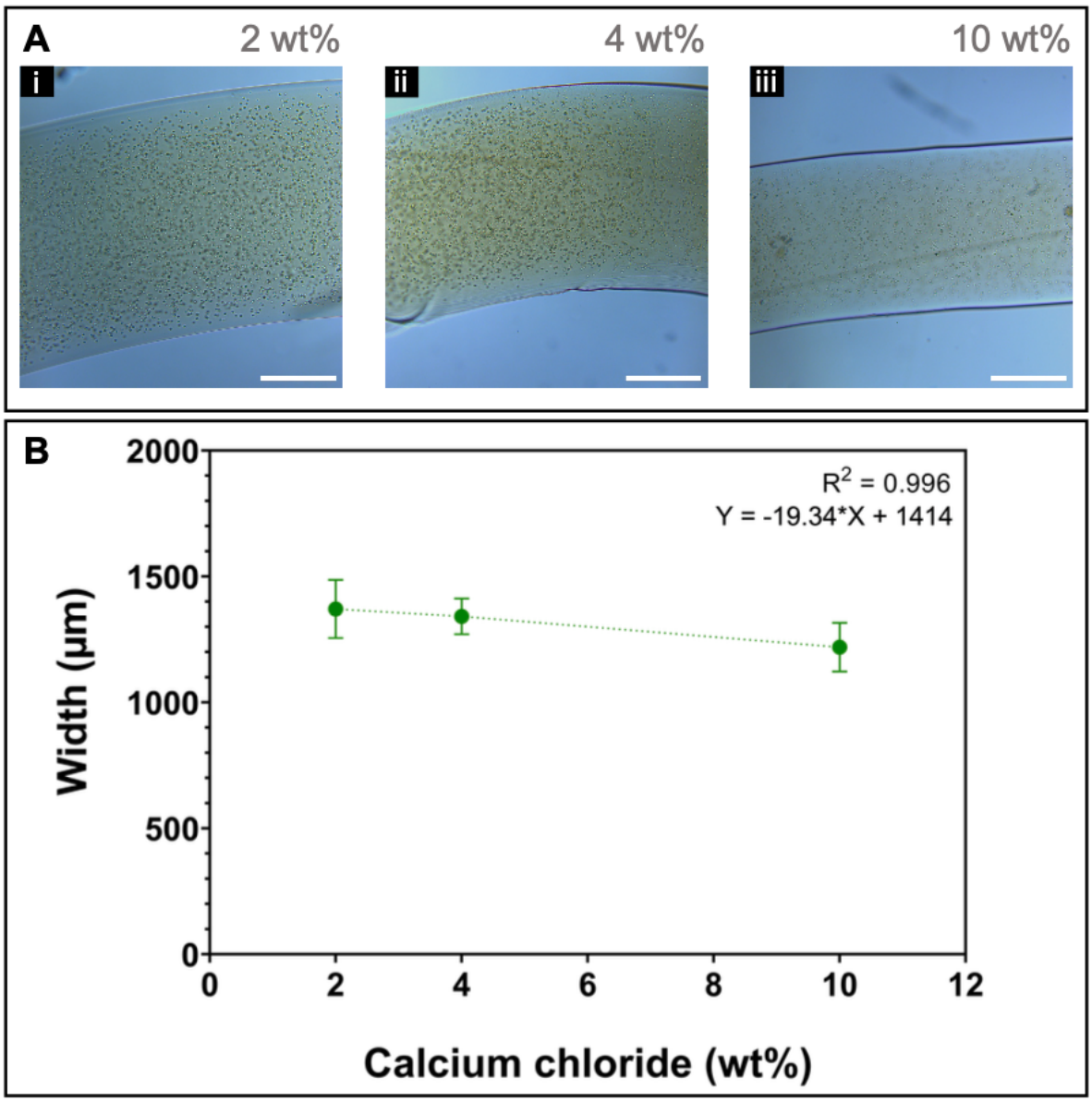


Figure 3. 7: Impact of $CaCl_2$ concentration on the width of the cell-encapsulated alginate fibres' shell. The extrusion flow rates used for alginate was 2000 µl.min^{-1} through a plastic tube, without the microfluidic chip, into the $CaCl_2$ bath solution at 2, 4 and 10 wt%. The concentration of alginate was kept constant at 2 wt%. **A i-iii**) Phase-contrast images of fibres, visually demonstrating their size in comparison to each other. Scale bar: 500 µm. **B)** A line graph illustrating the relationship between bath $CaCl_2$ concentration and the width of the fibre. Linear regression reported Y = -19.34*X + 1414. Data are shown as mean ± SD of three independent experiments. N = 3.

3.2.2.2. Impact of $CaCl_2$ concentration on cell viability and morphology

Cell viability

The effect of different $CaCl_2$ concentrations (2, 4 and 10 wt%) on 3T3s' viability while encapsulated in 2 wt% solid alginate-only fibres was investigated. Measurements for viability calculation of samples were collected, 24 hours after culture, as confocal Z-stack images at random locations in the sample, following a Live/Dead assay.

Figure 3.8 A-C (i) show phase-contrast images of 3T3s in alginate fibres, followed by corresponding confocal images of the cells (**Figure 3.8 A-C (ii-iv)**). Cells appear alive (green) in all test groups, confirming that cell-encapsulated alginate fibres can be extruded in different concentrations of $CaCl_2$ baths.

According to the results in **Figure 3.8 D**, the mean viability was observed to be highest for cells encapsulated in fibres that were bathed in 10 wt% $CaCl_2$ (86.6 ± 7.072%), followed by 4 wt% $CaCl_2$ (80.61 ± 12.12%), and 2 wt% group having the least cell viability of all three groups (69.03 ± 11.34%).

Statistical analysis revealed significant differences in cell viability amongst the different $CaCl_2$ concentrations ($p < 0.05$). As shown in **Figure 3.8 D**, increasing the concentration of $CaCl_2$ from 2 to 4 wt% in the bath solution resulted in a noticeable difference in cell viability by 11.58% ($p = 0.0011$). Cell viability was further improved, by 17.57% ($p < 0.0001$), when the bath $CaCl_2$ concentration increased from 2 wt% to

10 wt%. No significant difference was observed between 4 wt% and 10 wt% groups ($p = 0.2009$).

Overall, these findings demonstrate a dose-dependent effect of $CaCl_2$ concentration on cell viability of 3T3s embedded within the alginate-only solid fibres.

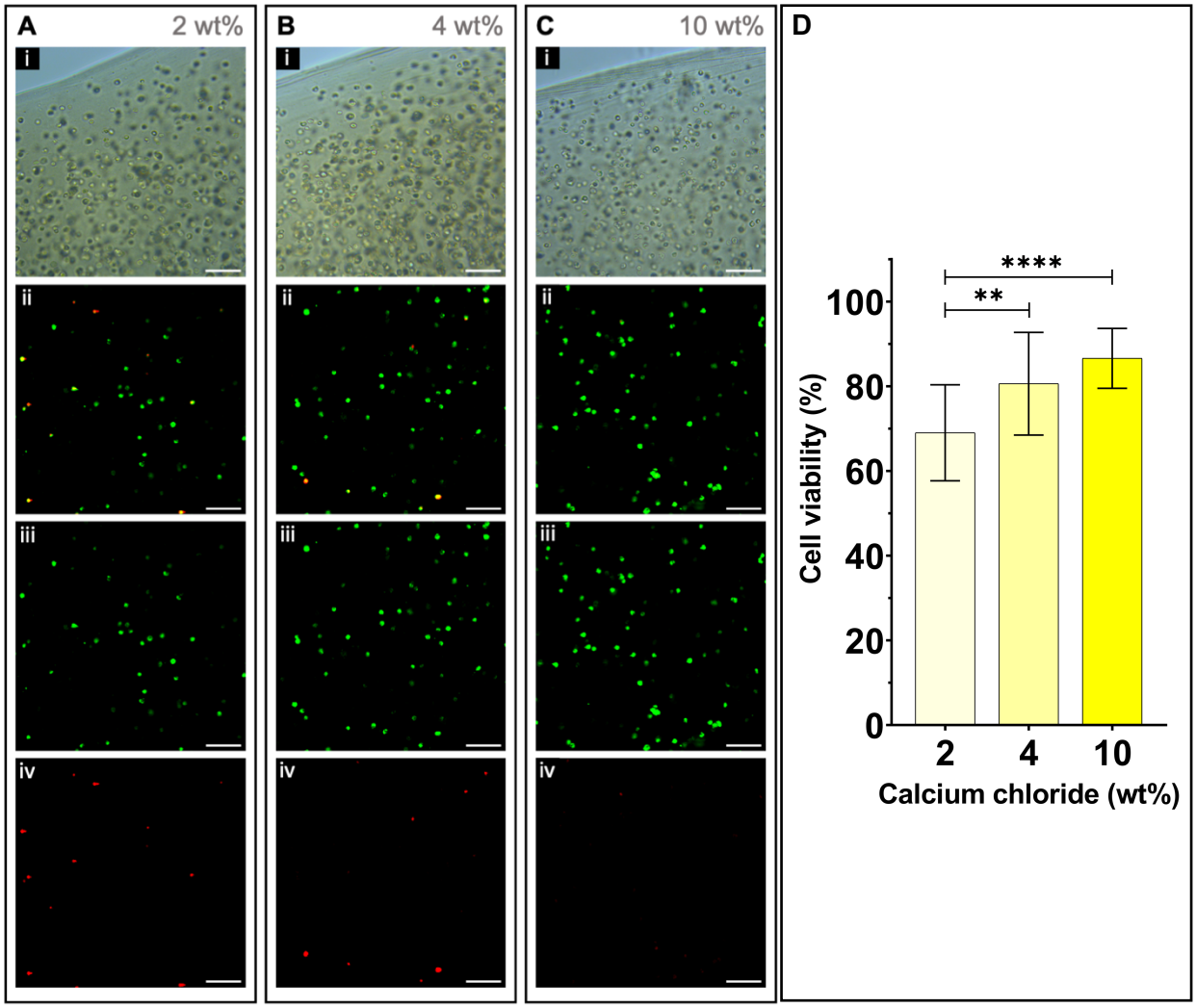


Figure 3. 8: Effect of bath $CaCl_2$ concentration on the viability of cells encapsulated in alginate fibres. The viability of cells (3T3s) embedded in solid alginate fibres was measured 24 hours after incubation, following bathing in different concentrations of $CaCl_2$ (2, 4 and 10 wt%) in water. The solid fibres without core were extruded at flow rate of 2000 µl.min^{-1}. Raw data were collected as confocal Z-stack images at random locations in the fibre samples, following a Live/Dead assay. **A - C i**) Phase-contrast images of cells encapsulated in alginate fibres. Scale bar: 500 µm. **A - C ii - iv**) Live (green) and dead (red) stained cells, encapsulated in the alginate fibres. Scale bar: 100 µm. **D)** Data are shown as mean ± SD of three independent experiments, representative of pooled measurements. This method was chosen to minimize bias and to get a more reliable p-value (see **section 2.2.4.2.**). A non-parametric one-way ANOVA on skewed data, followed by a multiple comparisons test among test groups 2 wt% (n=28), 4 wt% (n=29) and 10 wt% (n=30) was carried out ($p \leq 0.05$). Statistical analysis revealed significant differences in cell viability amongst the different $CaCl_2$ concentrations ($p < 0.05$). Cell viability was highest for 10 wt% $CaCl_2$ group (86.6 ± 7.072%), followed by 4 wt% $CaCl_2$ (80.61 ± 12.12%), and then 2 wt% group having the least cell viability of all three groups (69.03 ± 11.34%). ** $p \leq 0.01$ and **** $p \leq 0.0001$. Non-significant results ($p > 0.05$) are not labelled on the graph.

Cell morphology

Influence of different concentrations of $CaCl_2$ in bath solution on cell morphology is presented in **Figure 3.9**. In **Figure 3.9 A-C,** as well as **Figure 3.8 A-C** (ii-iv), it can be observed that cells remain spatially distant from each other and have a rounded morphology, 24 hours after culture.

The impact of different $CaCl_2$ concentrations (2, 4 and 10 wt%) on 3T3 cell's spreading area (μm^2), encapsulated in 2 wt% solid alginate fibres, is illustrated in **Figure 3.9 D**. The mean spreading area of a cell was 37.12 ± 8.01 μm^2 for 2 wt%, 38.05 ± 7.03 μm^2 for 4 wt% and 32.66 ± 5.96 μm^2 for 10 wt% group. However, statistical analysis revealed no significant differences in cell's spreading area amongst the different $CaCl_2$ concentrations ($p > 0.05$).

Overall, **Figure 3.9** provides insights into the distribution and morphology of cells within the solid alginate fibres, offering a closer examination of cellular interactions and spatial organisation within the alginate hydrogel matrix, 24 hours after culture.

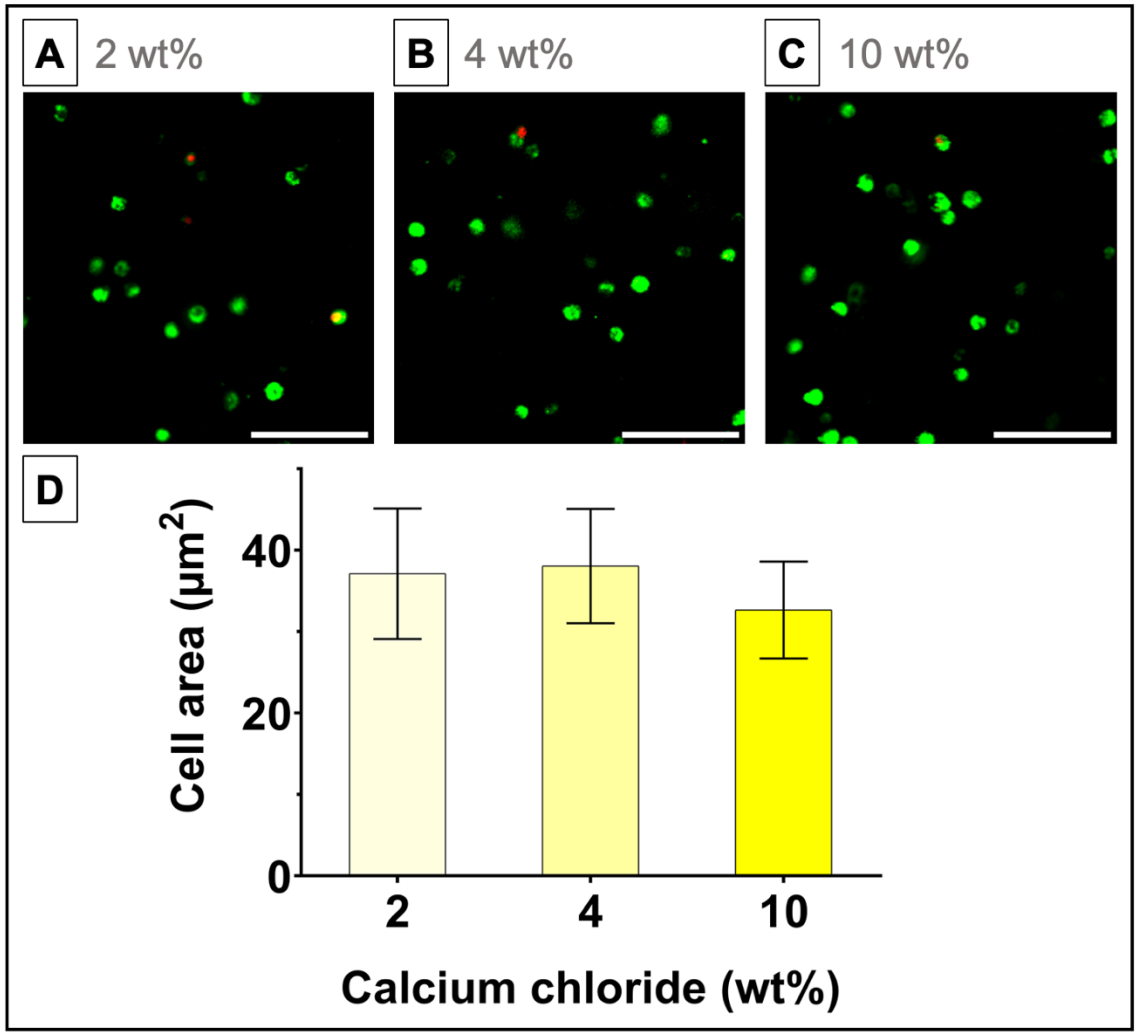


Figure 3. 9: Impact of different concentrations of $CaCl_2$ in bath solution on cell morphology. The extrusion flow rates used for alginate (2 wt%) was 2000 µl.min^{-1} through a plastic tube, without the microfluidic chip, into the $CaCl_2$ bath solution at 2, 4 and 10 wt%. Live/Dead stain was carried out after 24 hours of culture. Live (green) and dead (red) stained 3T3 cells, are shown encapsulated in the alginate fibres printed in **A)** 2 wt%, **B)** 4 wt% and **C)** 10 wt% $CaCl_2$ bath solution, with a rounded morphology. Scale bar: 100 µm. **D)** The relationship between bath $CaCl_2$ concentration and the mean spreading area of a cell (cell area; µm^2), encapsulated in the alginate fibre, 24 hours after culture is shown. Measurements for samples were collected as fluorescent images at random locations of the fibre samples, following a Live/Dead assay. Data are shown as mean ± SD of three independent experiments, representative of pooled averaged measurements from multiple images of samples (see **section 2.2.4.2.)**. Statistical analysis using a non-parametric one-way ANOVA, on skewed data, followed by a Dunn's multiple comparisons test between test groups revealed no significant differences in spreading area of a cell amongst the different $CaCl_2$ concentrations ($p > 0.05$). N = 9.

3.2.3. Changing the shell's polymer composition to promote cell attachment

3.2.3.1. Impact of increasing the gelatine concentration on viability, spreading area and amount of cells attached

The examination of cell morphology and attachment to the gel membrane in **Figure 3.10** provided valuable insights into cellular responses of cells seeded on alginate-gelatine blends composed of 0, 2, 6 and 10 wt% concentration of gelatine. Concentration of sodium alginate was kept constant at 2 wt%. **Figure 3.10 A-E (i)**, shows light microscope images confirming the presence of cells in all experimental groups, including the alginate-only control (0 wt%), prior to viability assessment following 24 hours of culture. However, a qualitative contrast emerged in stained confocal images (**Figure 3.10 A-E (ii-iv)**) after the Live/Dead assay was carried out, where a noticeable reduction in cell density was observed compared to the initial light microscope images. The Negative group (**Figure 3.10 E**) was used as a comparison for the percentage of cells present (as an indication of cell attachment to the test material) and morphology under normal culture conditions. Images such as those in **Figure 3.10 A-E (ii-iv)** were used to calculate the data presented in **Figures 3.11** and **3.12.**

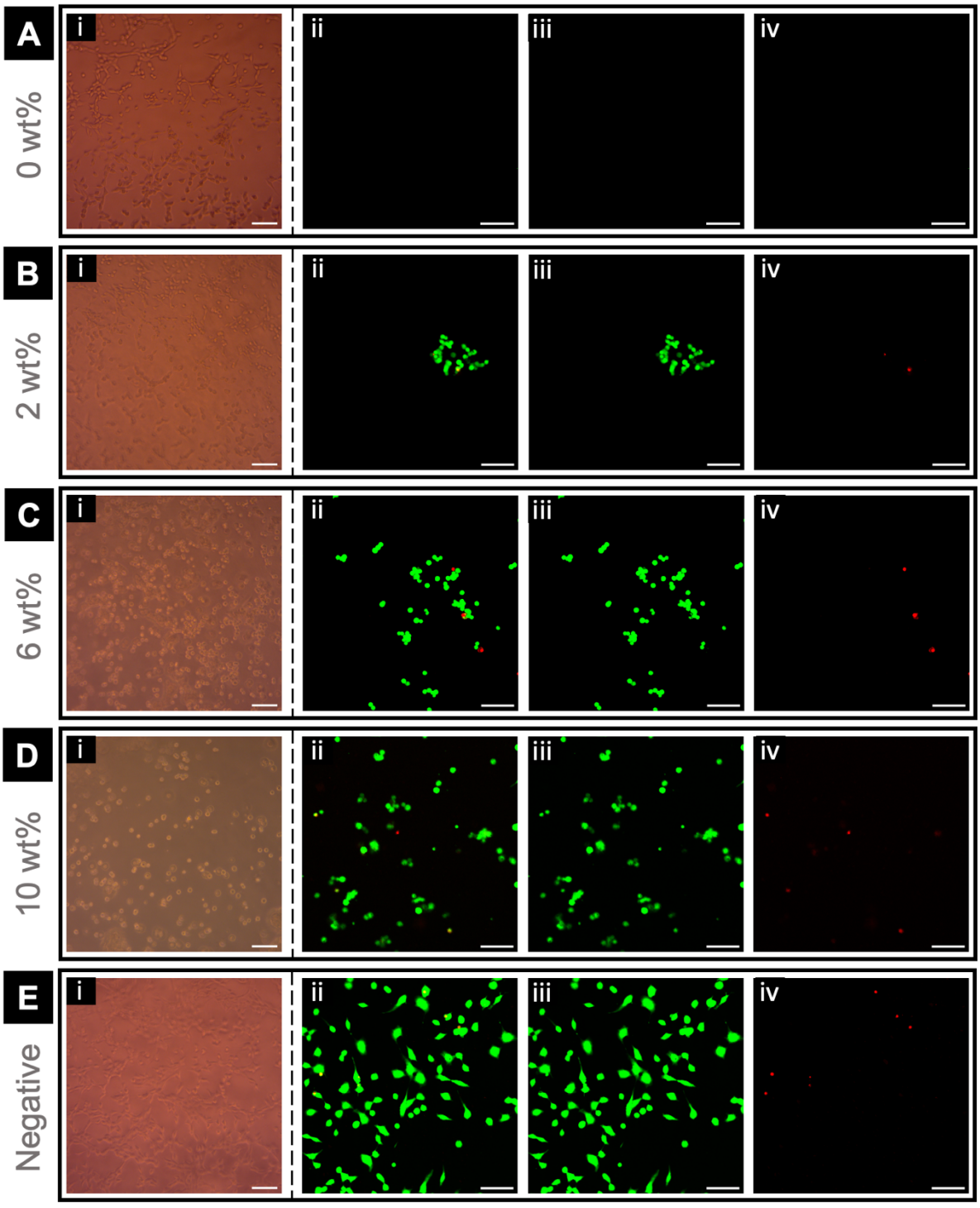


Figure 3. 10: Phase-contrast and confocal microscopy images of cells cultured on different concentrations of alginate-gelatine blends. Cells (3T3s) were cultured on alginate-gelatine blends composed of different concentrations of gelatine (0, 2, 6 and 10 wt%) for 24 hours, followed by a Live/Dead staining. **A-E (i)** show light microscope images of cells in each experimental group, 24 hours after culture, to demonstrate cell presence before Live/Dead assay was carried out. **A-E (ii-iv)** show confocal images illustrating cell morphology and numbers in comparison to the Negative control group. Scale bars: 100 μm.

Cell viability

The investigation into the impact of gelatine concentration (0, 2 , 6 and 10 wt%) on cell viability, 24 hours following culture on top of alginate-gelatine blends, was carried out (**Figure 3.11 A**). The mean viability of 3T3s in the Negative group was measured at 89.33 ± 5.04%, providing a reference point for the observed differences in the test groups where cells were seeded on top of the gel. Statistical analysis revealed significant differences in cell viability amongst the different groups tested ($p < 0.0001$). Alginate-only group (0 wt%) had a cell viability of 0 ± 0% which was significantly low compared to all other groups ($p < 0.0001$). Cell viability for 2 wt% gelatine group was 84.99 ± 13.76%, which was 4.3% lower compared to Negative control, however, it was not significantly different ($p = 0.5$). Cell viability for 6 wt% gelatine group was 80.51 ± 10.87%, which was significantly lower by 8.82% compared to Negative control ($p = 0.0072$). Cell viability for 10 wt% gelatine group was 81.69 ± 10.08%, which was significantly lower by 7.64% compared to Negative control ($p = 0.0067$). There was no significantly different cell viability within the groups with 2, 6 and 10 wt% gelatine added ($p > 0.05$). These results implied that seeding cells on top of alginate-gelatine blends, with 6 and 10 wt% concentrations of gelatine, had a noticeable decrease in cell viability compared to the Negative control.

Cell attachment

The relationship between gelatine concentration and the % cells present in samples (relative to Negative control) is presented in **Figure 3.11 B**. Results showed that after 24 hours of culture there were 0% cells left in 0 wt% gelatine group, which

was composed of alginate only with no gelatine added. Statistical analysis using a non-parametric one-way ANOVA, on skewed data, followed by a Dunn's multiple comparisons test between test groups revealed that only 10 wt% group had a significantly higher percentage of cells attached to the material compared to 2 wt% group by 150.07% ($p = 0.0357$). This is supported by qualitative observation of images in **Figure 3.10 A-D (ii-iv)** which show that 10 wt% gelatine had the most amount of cells present among the test groups. However, there was no significant difference between 6 wt% and other alginate-gelatine blend groups ($p > 0.05$). It is noteworthy that there was large variation in data as represented by large error bars.

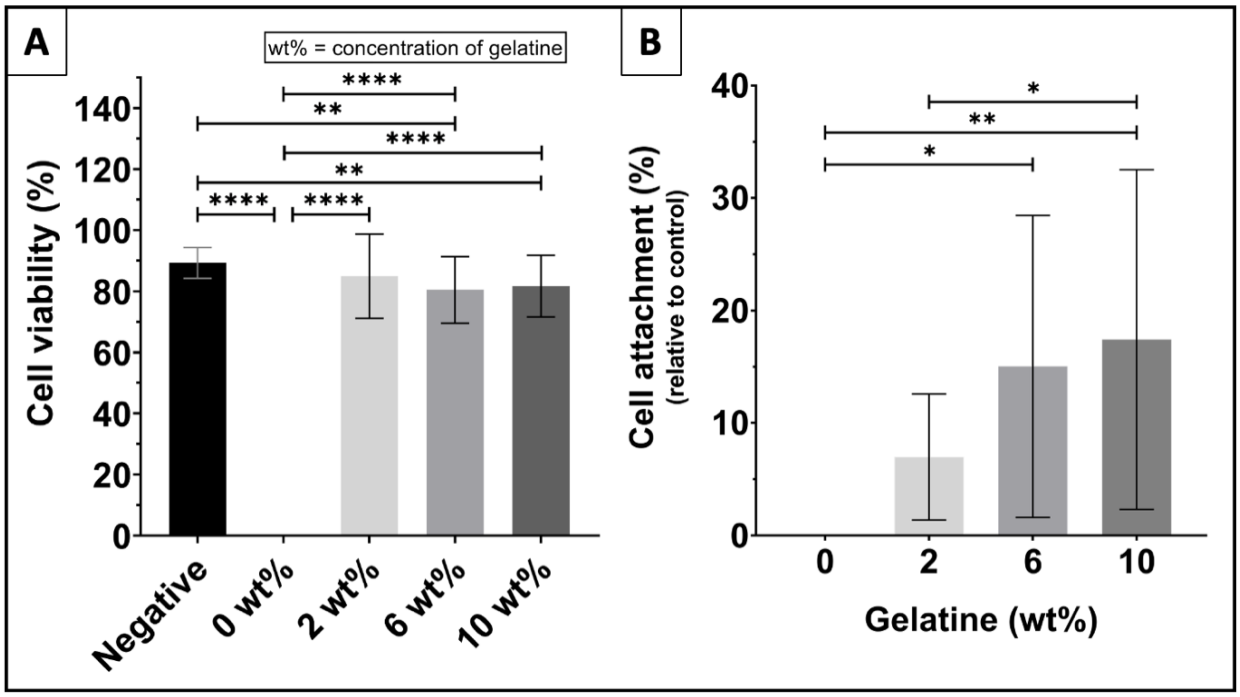


Figure 3. 11: Impact of gelatine concentration in the alginate-gelatine blend on cell viability and attachment. 3T3s were seeded on top of alginate-gelatine blends consisting of alginate (2 wt%) with different final concentrations of gelatine (2, 6, and 10 wt%). The test group of 0 wt% was used a positive control with no gelatine added. For Negative control, cells were seeded directly on the cell culture dish. The (**A**) viability (%) and (**B**) the percentage of cells attached to the test material (compared to Negative control; cell attachment (%)) were measured after 24 hours of culture. Measurements for samples were collected as fluorescent images at random locations of the samples, following a Live/Dead assay. Data are shown as mean ± SD of three independent experiments, representative of pooled averaged measurements from multiple images of samples (see **section 2.2.5.2.**). **A**) One-way ANOVA, followed by a Tukey's multiple comparisons test among Negative (n=35), 0 wt% (n=3), 2 wt% (n=21), 6 wt% (n=25) and 10 wt% (n=45), was carried out ($p \leq 0.05$). Alginate-only group (0 wt%) had a cell viability of 0 ± 0% which was expected due to no cells left in the samples (**B**). Cell viability for 2 wt% gelatine group was 4.3% lower compared to Negative control, however, it was not significantly different ($p = 0.5$). Cell viability for 6 wt% gelatine group was significantly lower by 8.82% compared to Negative control ($p = 0.0072$). Cell viability for 10 wt% gelatine group was significantly lower by 7.64% compared to Negative control ($p = 0.0067$). **B**) Statistical analysis using a non-parametric one-way ANOVA, on skewed data, followed by a Dunn's multiple comparisons test among 0 wt% (n=3), 2 wt% (n=23), 6 wt% (n=23) and 10 wt% (n=41) was carried out ($p \leq 0.05$). Only 10 wt% group had a significantly higher number of cells attached compared to 2 wt% group by 150.07% ($p = 0.0357$). No significant difference was observed between 6 wt% and other alginate-gelatine blend groups. There was large variation in data as represented by large error bars. * $p \leq 0.05$, ** $p \leq 0.01$, **** $p \leq 0.0001$. Non-significant results ($p > 0.05$) are not labelled on the graph. wt% on the graphs refer to gelatine concentration in the alginate-gelatine blend.

Spreading area of a cell

Impact of gelatine concentration on the average spreading area of a cell is illustrated in **Figure 3.12.** Statistical analysis using one-way ANOVA showed a significant difference in data ($p < 0.05$). However, Tukey's multiple comparisons test between groups revealed that only 10 wt% group had significantly different average spreading area of a cell compared to Negative group by 35.20% ($p = 0.0402$). There was no significant difference in the average spreading area of a cell amongst the different gelatine concentrations ($p > 0.05$). Alginate-only group (0 wt%) had significantly lower average spreading area of a cell compared to all other groups ($p < 0.0001$), as excepted due to absence of cells.

These differences in viability, spreading area and number of cells between experimental and Negative control groups provided useful insights into cell-material interactions for various gelatine concentrations.

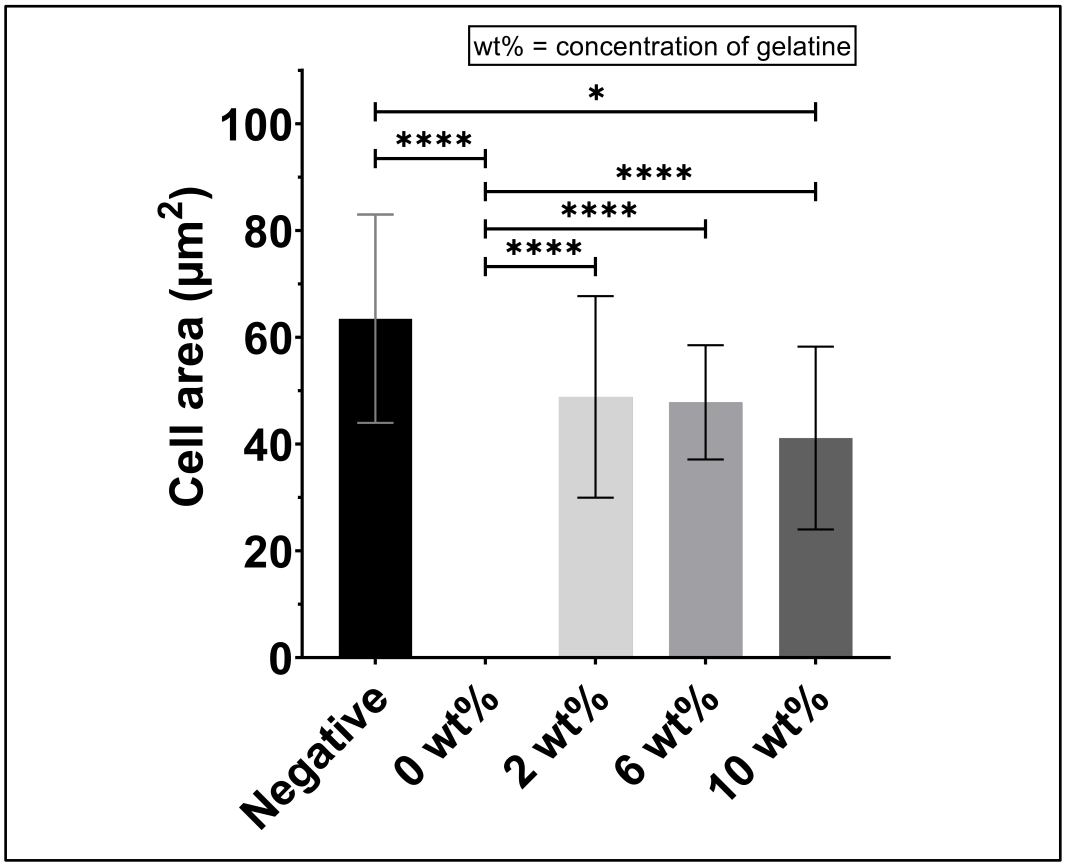


Figure 3. 12: Impact of gelatine concentration in the alginate-gelatine blend on spreading area of cells. 3T3s were seeded on top of alginate-gelatine blends consisting of alginate (2 wt%) with different final concentrations of gelatine (2, 6, and 10 wt%). The test group of 0 wt% was used as a positive control with no gelatine added to alginate. The Negative group refers to negative control where cells were seeded directly on the cell culture dish. The mean spreading area of a cell (cell area; μm^2), seeded on top of these polymer blends was measured after 24 hours of culture. Measurements for samples were collected as fluorescent images at random locations of the samples, following a Live/Dead assay. Data are shown as mean ± SD of three independent experiments, representative of pooled averaged measurements from multiple images of samples (see **section 2.2.5.2.**). One-way ANOVA with Tukey's multiple comparisons test between Negative (n=9), 0 wt% (n=9), 2 wt% (n=9), 6 wt% (n=9) and 10 wt% (n=7) was carried out ($p \leq 0.05$). Statistical analysis revealed that only 10 wt% group had significantly different spreading area of cells compared to the ones in Negative group by 35.20% ($p = 0.0402$). * $p \leq 0.05$, ** $p \leq 0.01$, **** $p \leq 0.0001$. Non-significant results ($p > 0.05$) are not labelled on the graph. wt% on the graph refers to gelatine concentration in the alginate-gelatine blend.

3.2.3.2. Impact of increasing the gelatine concentration on fibre's structure

Core-shell fibres with different composition of gelatine, in alginate-gelatine blends, were printed to test if the addition of gelatine affects core-shell fibre formation, as shown in **Figure 3.13**. Fibres with gelatine added to alginate-gelatine blend (**Figure 3.13 Aii-iv**) were compared with the control 0 wt% gelatine group with no gelatine added (**Figure 3.13 Ai**). In **Figure 3.13 A**, microscopic phase-contrast images show the structure of alginate-gelatine fibres and illustrates successful printing of core-shell fibres using 2 and 6 wt% gelatine in alginate-gelatine blends, like the alginate-only group (0 wt%). Fibre with 10 wt% gelatine did not have a distinct core like other groups (**Figure 3.13 A iv**).

Width of fibre's shell and core

Relationship between the width (μm) of the fibres' shell and core, and varying the concentration of gelatine, was investigated (**Figure 3.13 B**). The width of the shell (green line) gradually increased by 8.12% between alginate-only (0 wt%) and 2 wt% gelatine concentration group. Within the gelatine groups, width of the shell increased by 0.19% from 2 wt% to 6 wt%. From 6 wt% to 10 wt%, the width of the shell decreased by 27.81%. The mean width of the core (blue line) decreased by 6.34% between alginate-only (0 wt%) and 2 wt% gelatine concentration group. Within the gelatine groups, width of the core increased by 6.02% from 2 wt% to 6 wt%. For 10 wt% group, the width of the core was 0.

W_{core}/W_{shell}

The line graph (**Figure 3.13 C**) illustrates the relationship between gelatine concentration (wt%) within alginate-gelatine blend and the ratio of fibre's core and shell in width (i.e., W_{core}/W_{shell}). The W_{core}/W_{shell} value decreased by 13.37% between alginate-only (0 wt%) and 2 wt% gelatine concentration group. Within the gelatine groups, the W_{core}/W_{shell} value increased by 3.5% from 2 wt% to 6 wt%. From 6 wt% to 10 wt%, the W_{core}/W_{shell} value decreased by 33.27%. Furthermore, the results for the 10 wt% gelatine concentration showed considerable variation, as indicated by the error bar, suggesting increased variability in the observed width measurements for this concentration.

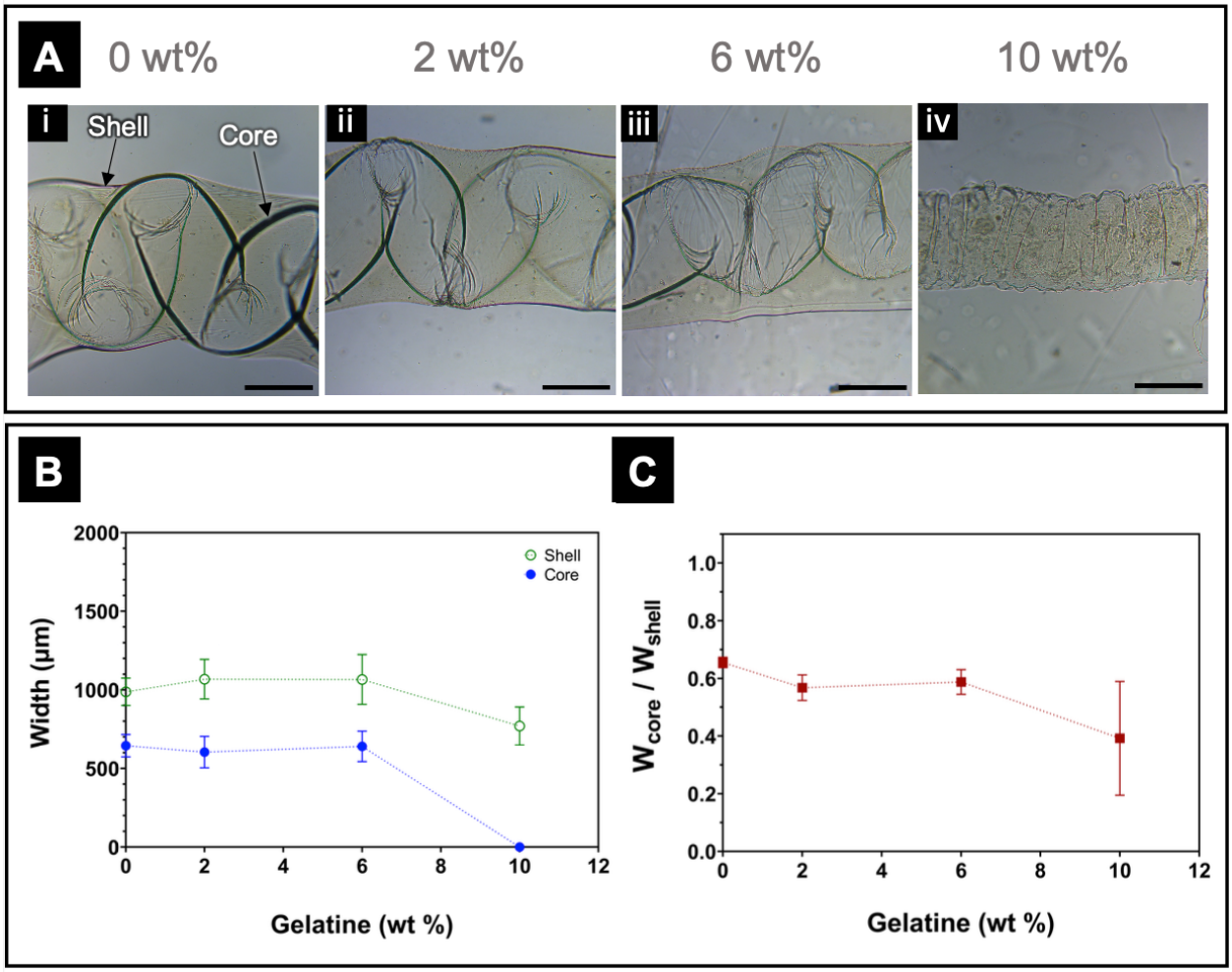


Figure 3. 13: Impact of gelatine concentration on the structure of alginate-gelatine hollow fibres. Core-shell fibres with different concentrations of gelatine were printed. The final concentration of gelatine, 0, 2, 4 and 10 wt%, in the alginate-gelatine blend fibres were tested, while the final concentration of alginate was kept constant at 2 wt%.The extrusion flow rates used for materials in this study were 2000 µl.min^{-1} for the shell and 1500 µl.min^{-1} for the core, into the 10 wt% $CaCl_2$ bath solution. **Ai – iv)** Phase-contrast images of core-shell fibres' structure. Fibres printed with 10 wt% gelatine (iv) did not have a distinct core. Scale bar: 500 µm. **B)** Relationship between gelatine concentration and the width of shell (green) and core (blue). **C)** Relationship between gelatine concentration and W_{core}/W_{shell} (i.e., fibre's wall thickness). Values are expressed as mean ± SD. n=3.

Helical pitch

The relationship between the helical pitch (μm) of the alginate-gelatine fibre's core and increase in the final concentration of gelatine at 0, 2, 6 and 10 wt%, was investigated. From **Figure 3.14**, no clear relationship between gelatine concentration and helical pitch can be observed. The helical pitch value (μm) decreased by 335.53 μm from the 0 wt%) to 2 wt%; then increases by 28.13 μm from 2 wt% to 6 wt% gelatine concentration before decreasing again to 0 μm for 10 wt%. Additionally, the data for 2 wt% and 6 wt% gelatine concentration vary considerably, as indicated by the large error bars, suggesting increased variability in the observed helical pitch measurements for these concentrations. Overall, from these results, varying the gelatine concertation in alginate-gelatine blends to achieve a specific helical pitch cannot be predicted accurately.

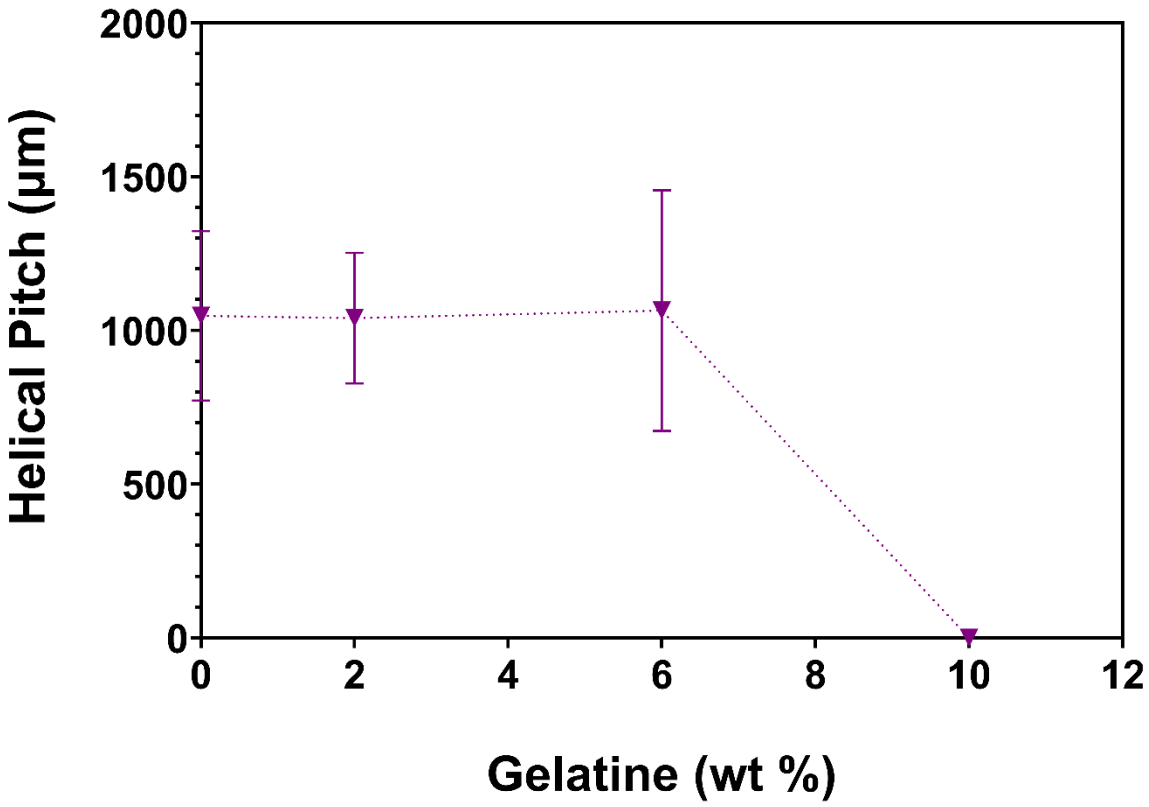


Figure 3. 14: Impact of gelatine concentration on the helical pitch of core-shell fibres' core. Core-shell fibres with different concentrations of gelatine were printed. The final concentration of gelatine, 0, 2, 6 and 10 wt%, in the alginate-gelatine blend fibres were tested, while the final concentration of alginate was kept constant at 2 wt%. The extrusion flow rates used for materials in this study were 2000 µl.min^{-1} for the shell and 1500 µl.min^{-1} for the core, into the 10 wt% $CaCl_2$ bath solution. Data are shown as mean ± SD of three independent experiments, representative of pooled measurements from multiple samples to account for measurements taken at random locations of each sample. N = ranges between 3 – 71.

3.3. Discussion

3.3.1. Effect of extrusion flow rate on core-shell alginate fibres' geometry

In order to mimic the blood vessels' structure, a precise control over the fabrication of the fibre and core's size and the thickness of the fibres' wall is important (106). Therefore, first aim of the study was to repeat the extrusion flow rates used by Moetazedian et al. (2023) to confirm the formation of core-shell fibres (110).

3.3.1.1. Printing process

Initially, the amount of material extruded was not specified to see if the fibre can be extruded continuously. It was found that continuous fibre could be printed in one go. The nozzle of the chip was held inside the bath solution to help the exiting partially crosslinked sodium alginate to be able to react with the $CaCl_2$. The partially linked sodium alginate crosslinked immediately upon touching the bath solution, forming a fibre. The yellow and blue dyes, mixed in the solutions, helped with visualising where each solution was concentrated in the fibre's structure. The yellow was on the outer edges of the fibre and blue was in the centre of the fibre. The dyes mixed to form green and bled into the bath solution when the fibres were left in the bath solution after printing. This finding is consistent with Lan et al. (2021) who

observed the blue dye leaking out of the hydrogel fibre's wall after 5 minutes of printing, thus confirming semi-permeability of the fibre's wall (152).

The Pluronic solution in the core of the fibre acted as a scaffold to hold the core of the fibre open for the alginate to polymerise with Ca^{2+} from the inside, to form different shapes of cores. The Ca^{2+} from the bath solution polymerised the alginate from outer side of the shell (106). Leaving the fibres in the bath solution for 30 minutes ensured that the sodium alginate was fully formed. As the Pluronic liquifies at low temperatures, storing the fibres in fridge (4 °C) for 10 minutes helped the Pluronic solution and dyes to leak out from the fibres structure, leaving a hollow core behind (110,153).

3.3.1.2. Fibre's structure

With increasing the core extrusion flow rate from 125 - 2000 $\mu l.min^{-1}$, the fibres' shell (i.e., overall fibre's size) became smaller in width by 21.04% while core increased in width by 103.11%. This was also reflected in the wall thickness as increasing the core flow rate (i.e., reducing the Q_{core}/Q_{shell}) resulted in an increase in W_{shell}/W_{core} by 140.74%. This means that by reducing the ratio of extrusion flow rate for core and shell, the amount of space taken up by the core in comparison to the overall fibre is increased, thus, reduction in fibre's wall thickness. Altering the fibre's core size with changing the flow rate of materials can be explained by the amount of Pluronic solution that is being extruded in comparison to sodium alginate at a given time. Pluronic solution coming from the inner channel of the chip pushes the sodium alginate solution outwards to the wall of the nozzle as it gels the sodium alginate.

Therefore, if the extrusion flow rate of core is changed, the force that it exerts to push the alginate solution to the chip nozzle's wall is changed. If the core flow rate is reduced from 2000 $\mu l.min^{-1}$ to 125 $\mu l.min^{-1}$, the force exerted is reduced and the amount of space the Pluronic solution takes up inside the fibre is also reduced, which results in thinner core. Furthermore, the wall of the printed fibre is translucent, allowing the core shape to be clearly seen through the fibre's shell without the use of a microscope. This is important because it allows the visualisation of fluids going through the fibres core if needed for different studies.

Ability to create vessel mimics with a range of sizes is essential for the progression of tissue engineering technologies within the field of regenerative medicine. In this project, vessel mimics with diameter sizes (i.e., W_{shell}) ranging from 1345.10 ± 191.17 μm to 1062.07 ± 143.20 μm were created. These sizes are comparable to the sizes of arteries and veins (**Table 1.1**)**.** Engineering of blood vessel mimics with even smaller diameters were beyond the scope of this project. Although different fabrications methods, vasculature mimics as small as 5 μm have been engineered previously (58,99). Therefore, one of the potential investigation opportunities is to push the capabilities of our novel microfluidic-based chip to print hollow hydrogel fibres that are comparable to the size of arterioles, venules, and even perhaps capillaries. For capillary-sized fibres, either hollow fibres that are within the diameter range of 3 μm – 30 μm (**Table 1.1**) could be printed or the endothelial cells embedded in arteriole-sized vessel mimics could be induced with growth factors (such as VEGF) to grow microvessels through the process of angiogenesis (**section 1.3.2.**). It is important to note that such microvessels should allow appropriate diffusion of relevant substances such as oxygen, carbon dioxide and metabolites

across the wall of the fibres between the plasma and bone tissue parenchymal cells. Further investigation into the range of vessel mimics that could be created with this microfluidic-based chip is very important for bone tissue engineering or testing novel therapeutics.

Helical pitch

The helical pitch is the twists and turns in the core along the lining of the shell. In literature, the extrusion flow rates have shown to play a role in core morphology (i.e., straight, wavy, helical) (96,154). Results in this study confirmed that different flow rate ratios (Q_{shell}/Q_{core}) generated different core helical shapes from straight, wavy and helical. This is an interesting finding because other technologies require a support structure to produce complex shapes of blood vessel mimics, such as a PDMS block to mould the 3D-printed blood vessel mimic, nozzle of the extrusion devices to be modified in sizes and quantities, and specific moulds to be used in order to print a specific core shape (96,154–157). In contrast, printing the hollow hydrogel fibres using our novel microfluidic chip does not require any moulds or further support. Previously, Jia et al. (2019) obtained similar helical structures as the ones in this study by microfluidics-based technique, however, they used a complex set-up of the device which required the nozzle of the chip to be adjusted to get a desired shape (96). With our novel chip, only the extrusion flow rates needed to be changed to create different core shapes, without the modification of the chip's nozzle or the requirements for specific moulds. In further studies, once the control of changes in helical shape of the core in relation to changes in core flow rate is

optimised, it will be a device of significant importance as it will allow the researchers to easily print a fibre with desired core shape without the need for sophisticated nozzles or moulds.

The mechanism behind the helical core formation and frequency of turns can be explained by the amount of core solution being extruded compared to the shell solution. A phenomenon observed by Jia et al. (2019) can provide some insights into why the decrease in core flow rate led to narrower helical pitch (96). Jia et al. (2019) increased the concentration of polyvinyl alcohol (PVA) in the crosslinker solution, extruded it from the outer channel for their device and alginate from the inner channel. This pushed the alginate solution inwards, decreasing the fibre's width and thus helped the fibre twist more easily and form a tighter coil (96). The similar situation could have happened with fibres in this study, but instead of sodium alginate in the centre, we had Pluronic in the centre and alginate on the outside. Although it was the addition of PVA in the solution extruded through the outer channel in that study that led to increase in sheer stress, it can still explain why the reduction in core's size in our case led to the decrease in helical pitch measurements (i.e., tighter coil). On the contrary, Xu et al. (2017) printed the fibre similar to ours with $CaCl_2$ in core and sodium alginate for shell and attributed the coiling of the core (helix formation) to the sheer forces exerted on the core by the gelled sodium alginate area (by the core solution) (154). When there is less core solution being extruded, during slower core flow rates, less of the shell solution is gelled within the nozzle area of the chip where the solutions first meet. Conversely, when more core solution is being extruded, during higher core flow rates, more of the shell solution is gelled within the nozzle area of the chip when the solutions first meet. This means the velocity of the

outer sodium alginate solution and the sheer stress is low when slower core flow rates are used compared to higher core flow rates, from 2000 $\mu l.min^{-1}$ to 125 $\mu l.min^{-1}$. Therefore, when less core solution is being extruded through partially gelled sodium alginate, which is exerting less shear stress on core due to low velocity, it can help the core twist and turn easily leading to a narrower helical pitch. On the other hand, when more core solution is being extruded through partially gelled sodium alginate, exerting more shear stress on it due to high velocity as a result of quicker gelling, it cannot move easily thus leading to a wavy or straight core.

Although multiple shapes of the core could be generated, when measurements for each test group was taken, the relationship between the helical pitch and core flow rate was not clear at the moment as the spread of error bars indicated the variation in data. This is due to the movement of chip during printing of fibres, because whenever the movement and orientation of the chip inside the bath was changed, the shape of the core seemed to be changing along with it. The chip had to be swayed from side to side to remove the extruded fibre out of the way as the new part of the fibre was being extruded. Otherwise, the printed fibre would block the new fibre section by forming a clump at the opening of the chip. In literature, other researchers fixed the printing nozzle which means they could control the core shape better (154,158).

The Reynolds number is a dimensionless number used for predicting the behaviour of fluid flow (159). It is related to fluid properties, flow rate and channel dimensions of the microfluidic-based chip. As a result, it influences the profile and pattern of the flow and, consequently, the core structure of the fibre. A high Reynolds number suggests turbulent flow while a low Reynolds number indicates a laminar

flow. Detailed investigation on the effect of Reynolds number was outside the scope of this thesis project. However, based on the analysis carried out by Moetazedian et al. (2023) (where identical microfluidic-based chip, similar printing conditions and solutions were used), the Reynolds number is expected to be under 100 (110). This would imply that, under our experimental conditions, laminar flow is taking place within our microfluidic-based chips. Nonetheless, in further studies, accurate calculation of the Reynolds number is encouraged to support the links between flow rate and changes in the internal structure of the fibre's core.

3.3.2. Testing different concentrations of $CaCl_2$ in bath solution

3.3.2.1. Fibre's structure

Width of the fibres, generated using different concentration of $CaCl_2$, was measured to see if the changes in $CaCl_2$ concentration influences fibres size. Using phase-contrast images of the fibres printed in 2 wt%, 4 wt% and 10 wt% groups, it was observed that the fibres were thinner for 10 wt% group (1219.06 μm) compared to 2 wt% (1371.13 μm) and 4 wt% groups (1341.80 μm). This was expected since higher the $CaCl_2$ concentration is, compared to sodium alginate, the higher the polymerisation and tighter the structure of the alginate gel due to high concentrations for Ca^{2+} (160,161). This could also explain the delicate nature of the 2 wt% and 4 wt% fibres, which were breaking easily during the handling of fibres, after 24 hours of

culture. For tuning the structural integrity, the mechanical strength of the fibres can be tested in future studies by doing tensile strength test, to ensure the fibres can withstand stresses (97,106).

The changes in fibre's size due to changes in $CaCl_2$ concentration is advantageous for the purpose of creating blood vessel mimics, as it will allow further control of the fibre's structure, in addition to the changes in core flow rate (as mentioned in **section 3.3.1.**). In future studies, perhaps higher concentrations of $CaCl_2$ can be tested such as 20 wt% and 30 wt% $CaCl_2$ to see if the fibres will continue to become thinner in width. According to the equation in **Figure 3.7**, the 20 wt% $CaCl_2$ baths should give around 1027.2 μm thick fibres and 30 wt% should give around 833.8 μm thick fibres. This will be an important thing to consider if an even smaller width fibre, than the ones generated in this study, are required in future studies. Although, the cell viability studies will need to be carried out to confirm the biocompatibility of those fibres.

3.3.2.2. Cell viability

Intriguingly, 3T3s encapsulated in fibres that were printed and bathed in 10 wt% $CaCl_2$ showed significantly higher viability compared to 2 wt% by 25.45% after 24 hours of culture. It is important to note that during the pilot studies, when fibres were printed in 10 wt% calcium bath, cells had a very low viability (see **Appendix D**). It was found that if the fibres are transferred directly to the media for culture, after being left in the bath for 30 minutes, it transfers excess $CaCl_2$ to the media, thus constant exposure of cells to the Ca^{2+} ions. Bosch-Rué et al. (2020) washed fibres with media after bathing to remove excess $CaCl_2$ before culture (153). Therefore, the same

rinsing step was carried out in this study following bath in $CaCl_2$, but sterile water was used instead to prevent the waste of media.

Trypsin, used for detachment of cells for culture, can cause some damage to the cells (162). When cells are reintroduced to Ca^{2+} in the bath solution, they are more sensitive to its cytotoxic effects, thus leading to apoptosis (163). Therefore, the reason behind cell survival for 10 wt% group being more compared to 2 wt% group could be the decrease in porosity of the fibre's structure. Higher the concentration of cross-linker used (i.e., $CaCl_2$), the tighter the crosslinking of alginate structure due to high concentrations for Ca^{2+} (160,161). This means that less $CaCl_2$ (along with water) was able to enter fibres from the bath, and cause cell damage for 10 wt% group compared to 2 wt% group. For 2 and 4 wt%, the fibres structure is more porous, so more cells are exposed to the $CaCl_2$ from the bath, that is why they experience more cell death. To support this interpretation, in the future, scanning electron microscope (SEM) analysis of the fibres can provide insight into differences in the porosity of the cross-linked alginate's structure between different calcium concentrations.

Since, 2 wt% group had a cell viability lower than the ISO standard (< 70%), it is considered cytotoxic and inadvisable to go ahead with this concentration in future studies (164). Although 4 wt% group met the ISO standard (cell viability > 70%), the fibres were more delicate compared to 10 wt% group.

3.3.2.3. Cell morphology

The cells were visibly evenly distributed in the hydrogel matrix of the fibres, as shown by the phase-contrast and confocal images, rather than being clumped together (**Figures 3.8 A-C** & **3.9 A-C**). The area of the cell was measured to get an

indication of cell growth after 24 hours of culture. It was found that cells remained rounded and the same size for all test groups. This was expected since cells have been shown to keep a rounded morphology when embedded in alginate fibres due to lack of cell-ECM interaction (165,166).

3.3.3. Changing the shell's polymer composition to promote cellular biocompatibility

The reason why these experiments were carried out is because although 3T3-embedded fibres with alginate could be printed (**section 3.2.2.**), which remained viable for 24 hours of culture, those cells had a rounded morphology and were not spreading as cells normally should. Lack of 3T3 adhesion to material has been reported to result in cell death (167). In literature, modification of alginate is recommended to support cell-ECM interactions for cells embedded within the hydrogel fibres, and for the cells that will be lined in the fibre's core in future studies (168). Gelatine is a well-tested material that allows cell attachment and spreading once the cells are seeded on it (139,169).

Extrusion flow rates of 2000 $\mu l.min^{-1}$ for shell was chosen in this experiment as it has already shown good cell viability in **section 3.2.2.2.**. Extrusion flow rates of 1500 $\mu l.min^{-1}$ for core was chosen because in **section 3.2.1.**, this was the fastest flow rate that could generate fibres with more frequency of helical core (as observed

qualitatively from images) and had a wide width that will be useful for cannulation studies later in the project. Additionally, fast extrusion speed of fibre printing will reduce the time for cells to be out of the media, thus less effect on cell viability.

3.3.3.1. Cell viability

The viability of 3T3s that were remaining on the gel after 24 hours of culture was measured to observe any trends in data between the different gelatine concentrations. As expected, groups with 0 wt% gelatine had a significantly lower viability compared to Negative group due to lack of adhesive motifs on alginate. Groups with 6 wt% and 10 wt% gelatine also had a significantly lower viability compared to Negative control, but their mean was still above 80%. Interestingly, the 2 wt% group did not have a significantly different viability compared to Negative group. This could possibly be due to the large overlapping error bars for 2 wt%. Overall, the investigation into the impact of gelatine concentration on cell viability, seeded on top of alginate-gelatine membranes, revealed that despite the increasing final concentrations of gelatine from 2 wt% to 10 wt%, cell viability did not change significantly between groups.

Data for the viability of cells in 2 wt% test group (**Figure 3.11 A**) should be interpreted with caution. This is because a very low number of cells were actually present in the sample when the confocal microscope images were taken, according to **Figure 3.11 B**. The loss of cells is due to cells not being able to attach to the alginate material (in the absence of gelatine) and thus are washed away during the Live/Dead staining process. To avoid the loss of cells and get a more accurate representation of cell viability, perhaps a cell viability assay that doesn't involve the

washing step can be carried out in future studies such as the ReadyProbes Cell Viability Imaging Kit (Blue/Green) (170,171).

3.3.3.2. Cell attachment

The attachment of the 3T3s to the surface of gel membranes containing different concentrations of gelatine from 0 wt% to 10 wt% were compared with Negative control (2D culture). This study was carried out to determine if the hydrogel blend material was adhesive for cells.

When the Live/Dead staining was carried out 24 hours after culture, there were no cells attached to the surface of gel membranes containing no gelatine (0 wt%) and only alginate present, as expected. The highest attachment of cells was to the surface of gel membranes containing 10 wt% gelatine compared to the groups with 2 wt% and 6 wt%. This was expected because higher the concentration of gelatine is in a polymer blend; higher the cell attachment should be as shown previously (172). It is important to consider that the cells were present in the wells before the Live/Dead assay was carried out, as shown in light microscope images. This means that the cells were washed away as the media was aspirated from the wells for the Live/Dead stain to be added.

Cell attachment mainly seemed to be towards the corners of the gel membrane and was not uniform throughout the surface of the gel, except for Negative group. Cell aggregate formation on gelatine was also observed previously (173). For this reason, confocal images for Live/Dead assay were taken only at locations with cells and there were large areas of the gel membranes for 2 wt%, 6 wt% and 10 wt%

gelatine groups that had no cells attached to the gel. This could be due to gelatine polymers sticking out of the alginate solution at specific places thus cells attaching to those areas of the gel only.

3.3.3.3. Cell area

The morphology of the 3T3s seeded on top of gel membranes containing different concentrations of gelatine from 0 wt% to 10 wt% were compared with Negative control (2D culture). This was measured to indicate if the cells were elongating or not following attachment to the test material. The cells seeded in Negative group showed spreading after 24 hours of culture as observed using Live/Dead stained images and spreading area of a cell was 63.49 ± 19.52 μm^2. However, the cells seeded on top of 2 wt%, 6 wt% and 10 wt% gelatine membranes had a rounded morphology and spreading area of a cell approximately 27.64% less (averaged) than the Negative group.

Nonetheless, from the results in this study, it can be hypothesised that alginate-gelatine with 2 wt%, 6 wt% and 10 wt% gelatine have the potential to allow attachment of HUVECs to the inner lining of the core-shell fibres, when tested in future studies.

3.3.3.4. Fibre's structure

Core-shell fibres composed of gelatine at 0 wt% (alginate-only), 2 wt%, 6 wt% and 10 wt% concentration were printed. Concentration of alginate was kept constant

at 2 wt% for all groups. The purpose of this study was to check if core-shell fibres can be printed even if gelatine is added to the shell solution and if the increase in gelatine concentration from 2 wt% to 10 wt% has any effect on the fibre's core formation. When the fibres were extruded using 2000 $\mu l.min^{-1}$ extrusion flow rate for shell and 1500 $\mu l.min^{-1}$ for core, the core-shell fibres were printed for 0 wt%, 2 wt% and 6 wt% gelatine blend groups but not for 10 wt%. This is likely due to the fluctuating temperatures, and solidifying, of gelatine in shell solutions which could not be kept the exact same temperature for all groups (174,175). Even when placed in 37 °C bath, by the time (less than 1 minute) the solution was transferred from the main bottle in the water bath to the syringe and after assembling of the printing equipment, the solutions had cooled down slightly to room temperature. For 2 wt% the gelling was slower compared to 6 wt% and 10 wt% groups and the fibres could be printed easily. However, the shell solution for 6 wt% would gel faster than 2 wt%, resulting in the blockage of tubes and chip channels during printing and thus had to be refreshed from solution warmed in the water bath for each technical repeat. Shell solution with 10 wt% gelatine gelled the fastest and would block the tubing (in less than 1 minute). This resulted in fibres without a defined core for 10 wt% group.

Width of the fibre's shell and core was measured to observe if there were any differences between different concentrations of gelatine used and the alginate-only group. The results showed that no clear trend between the fibre's structure and the gelatine concentration can be predicted. Generally, it could mean that there is no major difference in structure between fibre containing alginate-only and different concentrations of gelatine (except 10 wt%) in the shell solution. Same was observed for helical pitch.

3.4. Limitations of the study

For **section 3.2.1.**, there were some disparities between the data obtained in this study and the data generated by Moetazedian et al. (2023) for the width of shell and core, ratios and the helical pitch (110). Although the material preparation, extrusion flow rates and the printing equipment used were the same for both studies, the differences in the data could be attributed to the temperature and the chip size. As the Pluronic F-127 in core solution gels at room temperature, care was taken to keep it cool and in liquid form during printing. Ice was used to keep the microfluidic chip and solution cool before loading into the syringe, ice packs were placed on top of the syringes in the extrusion pump during printing. But whenever the printing was stopped, the tubing and the chip had to be cleaned with cold water within ~10 seconds otherwise the solution would gel inside and cause blockage. While printing, it is very likely that the temperature of the core solution fluctuated and resulted in different flows between replicates of each test group. This could have resulted in the slight variation of fibre's structure and inconsistency between data from this study and the data by Moetazedian et al. (2023) (110). Slight changes in the room temperature due to weather and time of the year could have also played a role in the liquid state of the core solution during printing. The equipment would get blocked with Pluronic solution quicker during the summer than it did during winter. In order to prevent further issues and ensure reproducibility of the data, in future studies it is best to use a syringe cooler such as the one designed by Kogler et al. (2022) to keep a constant temperature of core solution for the duration of printing process (176). Temperature regulated syringes will also ensure that regardless of where the

fibres are printed geographically, for example in countries with hot climates, the structure of the fibre generated should not be affected due to inconsistencies in the solution and room temperature. As for controlling the chip size and length of channels, rather than just cutting the chip out from the Petri dish it was casted in, it is best to use a custom 3D-printed master mould, as done by Behroodi et al. (2020), for casting PDMS to form the chip (177). This should simplify the production of chips, ensure reproducibility, and allow for rapid manufacturing in the future. If the disparities in data were caused due to any differences in the size of the chip, it should be reduced by consistency in the chip design.

For **section 3.2.3.2.**, in future studies it is best to use a syringe warmer such as the Syringe Heater Kit (New Era Instruments, USA) to keep a constant temperature of the shell solution at 37 °C for the duration of printing. Fan et al. (2016) printed a 3D construct with and without temperature-control and found that controlled temperature enhanced the homogeneous composition of the material (agarose in their case) (178). Therefore, printing alginate-gelatine blends with a temperature-controlled syringe will ensure a hollow core-shell fibre is printed, that has a homogeneous composition of the material and less variation between the technical repeats.

The mechanical properties of the hollow fibres have not yet been measured. Once the printing conditions are optimised, the investigation into the mechanical properties of the fibres should be carried out and comparisons made with those of native blood vessels.

In future studies, if the experiments for cell viability and cell area are repeated, they should be carried out separately. In this research project, cell viability studies were given priority as they were some of the main experiments (**Figure 3.8 D & 3.11**

A). The data used to create graphs for **Figures 3.9 D** and **3.12** were the same confocal microscope images taken for cell viability studies. This could potentially be the reason behind high variability in results for cell area because low-resolution images were used. For this reason, data regarding the cell area should be taken with caution. Additionally, Live/Dead stain was used for visualising the cells and it stains part of the cytoplasm, not the full cell. Therefore, the data for cell morphology in **Chapter 3** have been included to give only an indication of cell area. To get a more accurate representation of the changes in cell spreading area in future studies, stains for actin protein (e.g., the gold standard phalloidin or CellMask™ Green Actin Tracking Stain kit) can be used because it is present throughout the cell (179). Furthermore, higher resolution images (using the 20X objective lens) should be taken for subsequent image analysis.

In future studies, the confocal microscope images for measuring cell viability, cell area and cell attachment should be taken at fixed locations of the samples for technical repeats within an experiment. Currently, a minimum of three Z-stacks (**section 2.2.4.2.)** or individual images (**section 2.2.5.2.**) were taken per technical repeat at random locations of the samples. Additionally, for **Figure 3.9 D**, only three images were used for extracting raw data (average cell area) per experimental repeat for each test group. To get more reliable data, in addition to taking images at fixed locations of the sample (such as the start, middle and end of the fibre for **Figure 3.9 D**), a minimum of five Z-stacks or individual images should be taken. This is because, if any of the images for a technical repeat need to be excluded from data analysis, due to background noise in fluorescence during image processing, there will still be three or more samples within a technical repeat for averaging and statistical analysis.

3.5. Summary

This study confirmed that by using the novel microfluidic-based chip, a range of hollow core-shell fibres can be generated with a defined width and geometry, just by changing the extrusion flow rates of core solution. Fibres printed in 10 wt% $CaCl_2$ bath had a high viability, compared to 2 wt% and 4 wt% groups, were stronger to handle and also had a smaller width. For this reason, it was confirmed that the 10 wt% concentration of the bath solution was right for this project. Addition of gelatine to the shell solution improved cell attachment to the material in a dose-dependent manner. However, the formation of fibre became difficult with increasing concentrations of gelatine due to gelatine gelling at room temperature and blocking the printing equipment. Therefore, for the prolonged cell culture and fibre degradation studies (**Chapter 4**), 2 wt% gelatine concentration is chosen due to its ease of use, core-shell fibre formation and confirmation of cell attachment.

4. Effect of prolonged culture on cell viability and fibre degradation

4.1. Introduction

Having established some cell attachment on gel membranes (**section 3.2.3.1.**), studies in this chapter were carried out to investigate the viability of cells encapsulated inside the fibre‘s shell. General purpose behind this study was to observe how the cells react to material over time and how the material will need to be modified to improve its biocompatibility before it is made more complex in the future. This will allow optimisation for SMCs, embedded in fibre’s shell, when used in the future for producing 3D-printed blood vessel mimics.

Overall, it would be an interesting finding to observe how much the culture of fibres printed using the novel microfluidic chip can be prolonged. Therefore, the time-points tested were Day 1 to observe what would happen to the cells and fibres after 24 hours of culture, as normally tested during this project so far, and then every week from the start date of when the fibres were printed, on Day 7, 14, 21, and 28.

In this chapter, the impact of the shear stress produced by the extrusion technique, using the novel chip, on cell viability between fibres without a core (Group A) and with a core (Group B) after 24 hours of culture (Day 1) will be assessed. Comparison between the core-shell alginate-only fibre (Group B) and core-shell fibre with the 2 wt% gelatine added (Group C) was to see if the addition of gelatine has any influence on cell viability and fibre structure over a long period of culture.

The reason behind the use of 2 wt% gelatine concentration for prolonged cell culture is because with this concentration the fibres were easy to print (**section 3.2.3.2.**) and there was still some cell attachment, compared to the 0 wt% (alginate-only) group (**section 3.2.3.1.**). Although 6 wt% and 10 wt% groups had generally

more cell attachment, the fibres were not easy to print at this stage. In future studies, depending on the results for 2 wt% gelatine, fibres with 6 wt% and 10 wt% gelatine can be printed and compared with 2 wt% group. HUVECs attachment to the fibre's inner lining can be compared between these groups, when the fibres are perfused with cell suspended media for culture.

In this chapter, the effect of prolonged culture time on fibre's structure, cultured and stored under different conditions, was also tested. This is a crucial analysis because it will provide insights into how the storage conditions of the fibres will need to be optimised to ensure their structural integrity for tissue engineering.

Therefore, the overall aim of this chapter is to assess the impact of fibre extrusion, with varying structures, on cell viability and storage conditions and time-dependent degradation of fibres over a prolonged culture period.

4.2. Results

4.2.1. Testing different types of fibres

4.2.1.1. Viability and morphology of cells embedded in fibres for a 28-Day culture

To investigate the changes in morphology and viability of cells embedded in different types of fibres, across long culture period, this study was carried out. 3T3s were embedded in alginate-only solid fibres (**Figure 4.1**), alginate-only core-shell fibres (**Figure 4.2**) and alginate-gelatine core-shell fibres (**Figure 4.3**). Live/Dead assay was carried out on cells encapsulated in fibres on Day 1 (24 hours of culture), 7, 14, 21 and 28. Confocal images of cells were captured and used for morphological and viability analysis.

Figures 4.1- 4.3 show that the morphology of cells embedded in all fibres appeared rounded across all days. For all groups, cells show a consistent distribution throughout the hydrogel with little to no apparent clustering. From the green channel (live cell) images (A & B), a consistent signal is observed throughout the culture period, which indicates sustained cell viability within both alginate-only (**Figures 4.1 & 4.1**) and alginate-gelatine blend (**Figure 4.3**) fibres. However, the green channel images for Day 28 for both solid (**Figure 4.1**) and core-shell (**Figure 4.2**) alginate-only fibres exhibit a lot of background noise, characterised by bright green fluorescence. In order to improve the visibility of red channels (dead cells), due to a

faint signal which was detected across all days, they had to be enhanced using the Fiji software (**Figure 4.1C – 4.3C**).

Overall, the confocal microscopy analysis provided a valuable insight into the viability and morphology of 3T3s embedded within the solid and core-shell fibres composed of alginate-only and alginate-gelatine blends, across 28-day culture.

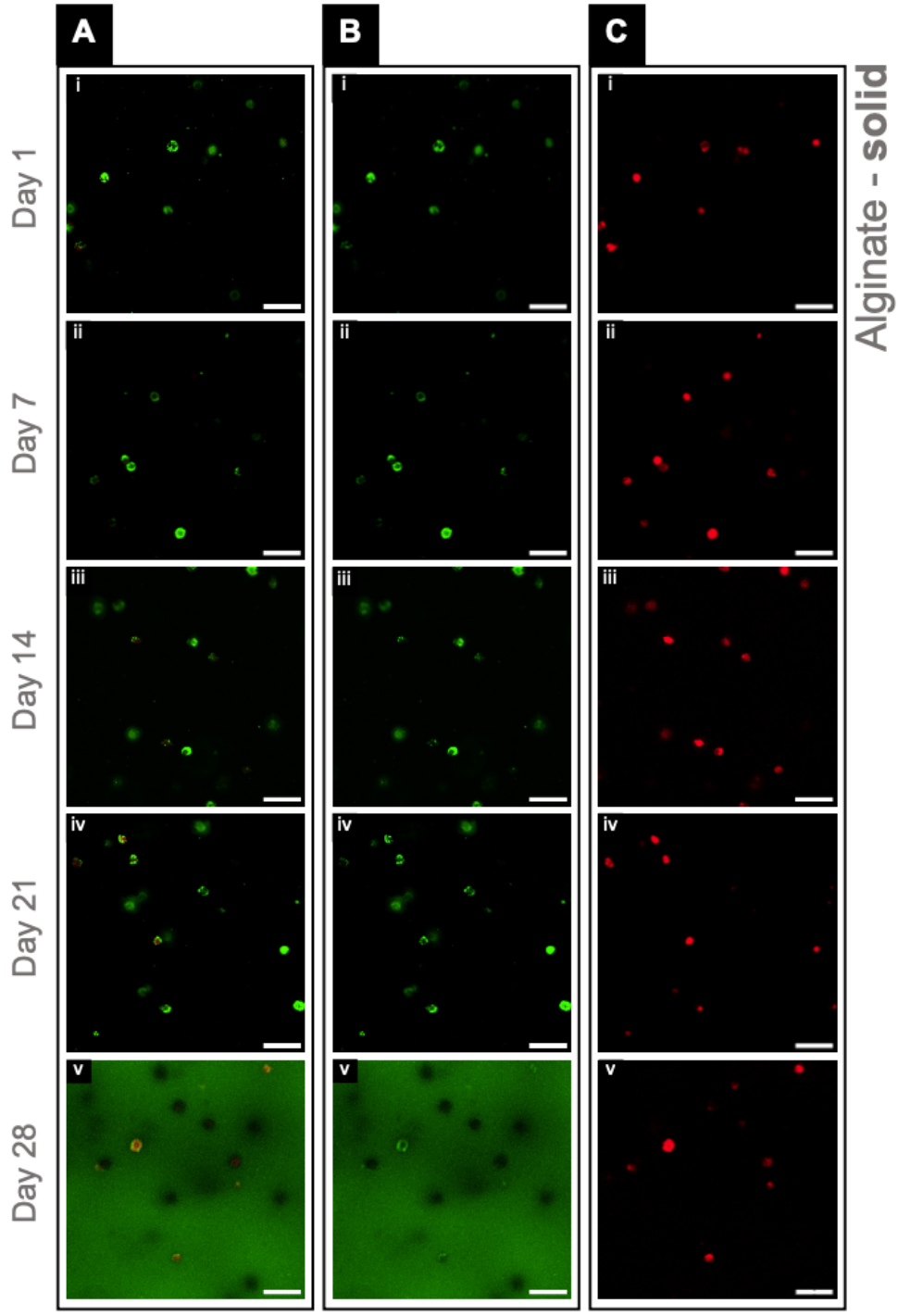


Figure 4. 1: Confocal microscopy analysis of cells embedded in solid alginate fibres. 3T3s embedded within solid alginate fibres are presented, with each row representing a specific day of culture: Day 1 (i), 7 (ii), 14 (iii), 21 (iv) and 28 (v). Each column displays different confocal imaging channels: **A**) both red and green channels, **B**) green channel (alive cells) only, and **C**) red channel (dead cells) only. The contrast in red channels (**C**) was enhanced by 0.35 saturation using Fiji software. Scale: 100 µm.

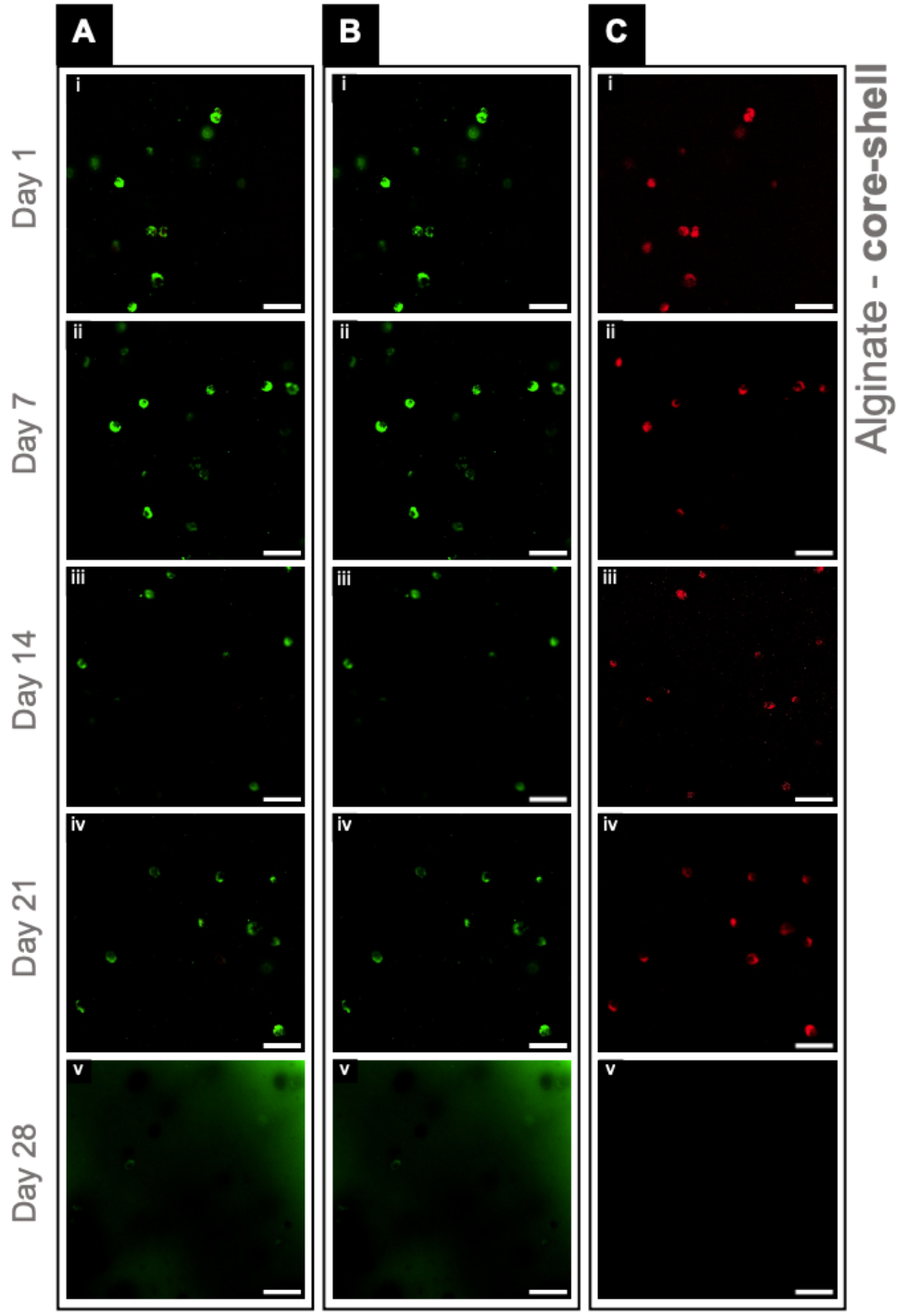


Figure 4. 2: Confocal microscopy analysis of cells embedded in core-shell alginate fibres. 3T3s embedded within core-shell alginate fibres are presented, with each row representing a specific day of culture: Day 1 (i), 7 (ii), 14 (iii), 21 (iv) and 28 (v). Each column displays different confocal imaging channels: **A**) both red and green channels, **B**) green channel (alive cells) only, and **C**) red channel (dead cells) only. The contrast in red channels (**C**) was enhanced by 0.35 saturation using Fiji software. Scale: 100 µm.

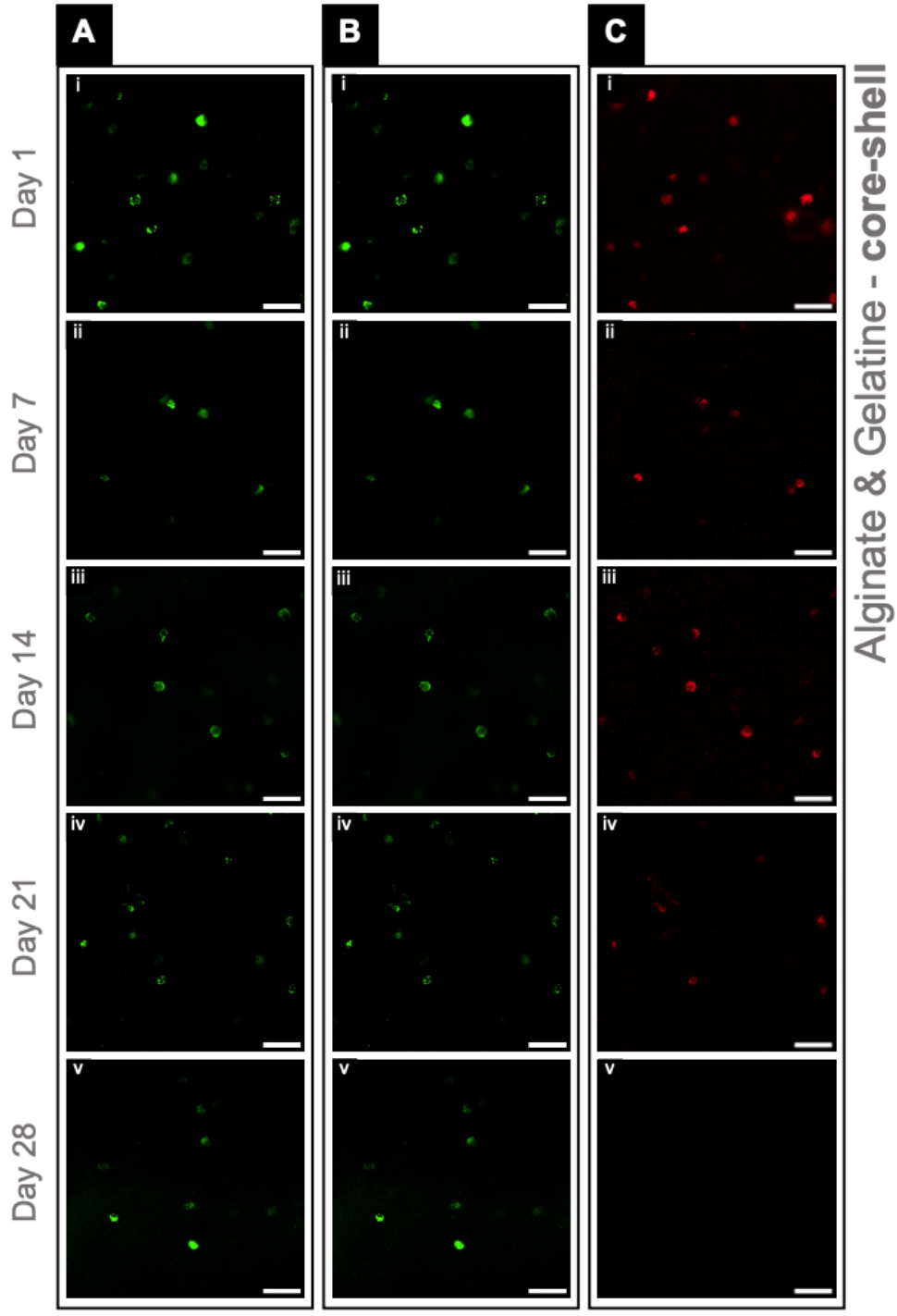


Figure 4. 3: Confocal microscopy analysis of cells embedded in core-shell alginate-gelatine blend fibres. 3T3s embedded within core-shell alginate-gelatine fibres are presented, with each row representing a specific day of culture: Day 1 (i), 7 (ii), 14 (iii), 21 (iv) and 28 (v). Each column displays different confocal imaging channels: A) both red and green channels, B) green channel (alive cells) only, and C) red channel (dead cells) only. The contrast in red channels (C) was enhanced by 0.35 saturation using Fiji software. Scale: 100 μm.

Cell viability

Changes in the viability of three types of cell-encapsulated alginate fibres, over a 28-day culture period was studied (**Figure 4.4**). The types of groups tested were two alginate-only fibres with a solid (Group A) and core-shell (Group B) structure, and alginate-gelatine blend core-shell fibres composed of 2 wt% alginate and 2 wt% gelatine (Group C). The days the measurements were taken were Day 1, 7, 14, 21 and 28. Measurements for samples were collected as confocal Z-stack images at random locations in the sample, following a Live/Dead assay. Statistical analysis using a parametric and non-parametric one-way ANOVA — on normally distributed and skewed data, respectively — followed by a multiple comparisons test between Groups at a specific timepoint (Day) and between Days for each group ($p \leq 0.05$).

For a multiple comparisons test between Groups at a specific timepoint (Day), significant differences in viability were observed (**Figure 4.4**; $p \leq 0.05$). For Day 1 and Day 14, Group B had a significantly higher viability compared to Group A by 7.44% ($p= 0.0345$) and 15.68% ($p= 0.017$), respectively. Additionally, for Day 1, Group B also had a significantly higher viability compared to Group C by 9.77% ($p= 0.0072$). For Day 14, Group C had a significantly higher viability compared to Group A by 21% ($p= 0.0014$).

For a multiple comparisons test between Days for each group, significant differences in viability were observed (**Figure 4.4**; $p \leq 0.05$). Group A had a significantly higher viability on Day 21 compared to Day 1 by 15.29% ($p= 0.0249$). Group B had a significantly higher viability on Day 7 compared to Day 1 by 27.64% ($p= 0.0012$). However, between Day 7 and Day 21, viability of cells in Group B

reduced by 28.06% (p= 0.0015). Group C had a significantly higher viability on Day 7 compared to Day 1 by 26.86% (p= 0.0378), which further increased by 29.64% (p= 0.0172) on Day 14.

Overall, this study provides an overview of the changes in viability between cell-encapsulated fibres with different structures when cultured for 28 days**.**

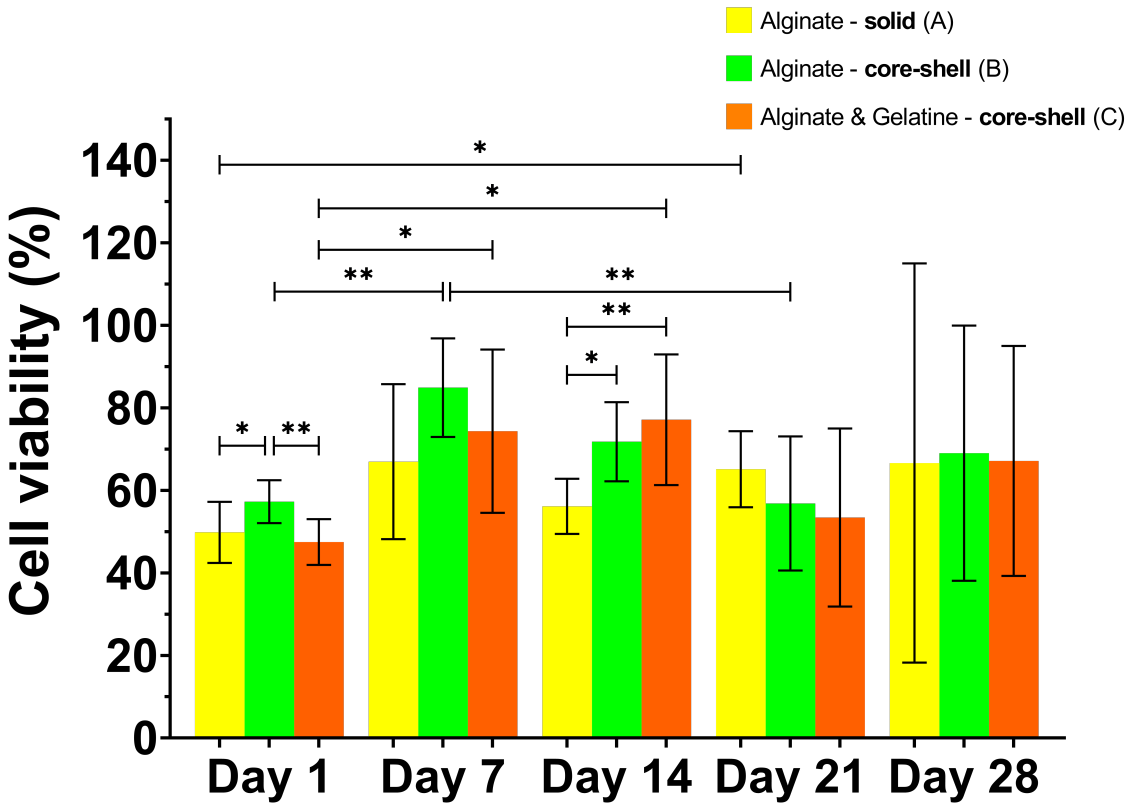


Figure 4. 4: The viability of 3T3s embedded in different types of fibres and cultured for 28 days. The types of cell-encapsulated fibres tested were: (**A**) solid and (**B**) core-shell fibres composed of 2 wt% alginate only and (**C**) core-shell fibres made of 2 wt% alginate and 2 wt% gelatine blends. Extrusion flow rates used were 2000 µl.min^{-1} for shell (**A-C**) and 1500 µl.min^{-1} for core (**B-C**). Measurements for samples were collected as confocal Z-stack images at random locations in the sample, following a Live/Dead assay. Data are shown as mean ± SD of one independent experiment, representative of pooled measurements from multiple samples. Statistical analysis using a parametric and non-parametric one-way ANOVA — on normally distributed and skewed data, respectively — followed by a multiple comparisons test between Groups at a specific timepoint (Day) and between Days for each group ($p \leq 0.05$) was carried out. * $p \leq 0.05$ and ** $p \leq 0.01$. Non-significant results ($p > 0.05$) are not labelled on the graph. N = ranges between 3 - 11.

4.2.1.2. Effect of culture time on fibres' morphology

The temporal changes in three types of cell-encapsulated alginate fibres' morphology were observed using phase-contrast microscopy, over a 28-day culture period (**Figure 4.5**). The types of groups tested were two alginate-only fibres with a solid (Group A) and core-shell (Group B) structure, and alginate-gelatine blend core-shell fibres composed of 2 wt% alginate and 2 wt% gelatine (Group C). The days the images were taken are Day 1, 7, 14, 21 and 28. The individual fibre was printed for each day, and the columns do not represent a single fibre imaged over time (**Figure 4.5 i-vi**).

The temporal phase-contrast images of fibres illustrate the visual changes in fibres shell overtime for each test group (**Figure 4.5**). The shell of the fibres is seen to be cracking, when compared with Day 0 fibres, and even break in some areas, such as for images **Figure 4.5 B & C (v)**. A noteworthy finding is the gradual darkening of the fibres over time, with Group B and C appearing more darker compared to Group A. It is interesting to note that the culture media was changed regularly, indicating that factors other than nutrient depletion or waste accumulation could be the cause of observed changes.

Overall, the images reveal progressive changes in fibres' structure, including cracking in the shell wall and darkening, suggesting dynamic remodelling within the hydrogel matrix over a long period of culture.

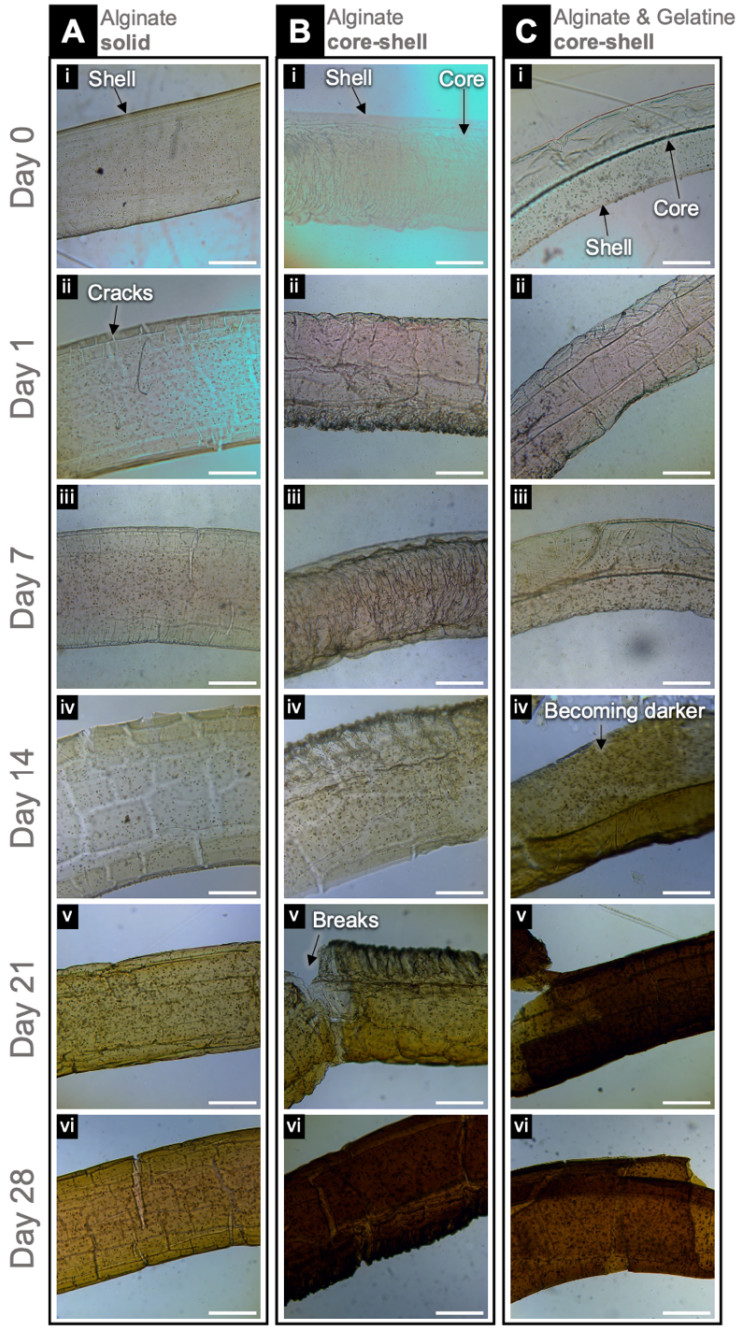


Figure 4. 5: Phase-contrast images of temporal changes in three different types of fibres. The types of cell-encapsulated fibres tested were: (**A**) solid and (**B**) core-shell fibres composed of 2 wt% alginate only and (**C**) core-shell fibre made of 2 wt% alginate and 2 wt% gelatine blends. Fibres were cultured in supplemented DMEM, which was changed regularly. Images represent multiple fibres that were printed specifically for the day the images were taken. Each row within the figure represents a specific day of culture (Day 1, 7, 14, 21 and 28) for all three groups, allowing for a visual comparison of fibre's morphology over time. Extrusion flow rates used were 2000 µl.min^{-1} for shell (**A-C**) and 1500 µl.min^{-1} for core (**B-C**). Scale bar: 500 µm.

Width of fibre's core and shell

The temporal changes in three types of cell-encapsulated alginate fibres' morphology, over a 28-day culture period was observed (**Figure 4.6**). The types of groups tested were two alginate-only fibres with a solid (Group A) and core-shell (Group B) structure, and alginate-gelatine blend core-shell fibres composed of 2 wt% alginate and 2 wt% gelatine (Group C). The days the measurements were taken were Day 1, 7, 14, 21 and 28 and the day when samples were first printed. For example, a fibre printed for Day 1 was measured on the day it was printed (Day 0) and one day later (Day 1).

For each test group, the width of fibres' shell and core was statistically compared between the day the fibre was printed and the day of interest when the measurements were taken. Statistical analysis using a two-tailed parametric and non-parametric t-test — on normally distributed and skewed data, respectively — between Day 0 and the corresponding day was carried out. For group A, the increase in fibre's mean shell size after 1 day and 14 days were 212.5 μm ($p= 0.0053$), 520.7 μm ($p = 0.0062$), respectively (**Figure 4.6 Ai**). For group B, the increase in fibre's mean shell size after 1 day and 14 days were 176 μm ($p<0.0001$), 388.1 μm ($p<0.0001$), respectively (**Figure 4.6 Bi**). For group C, the increase in fibre's mean shell size after 7 and 14 days were 133.9 μm ($p = 0.0422$), 235.3 μm ($p<0.0001$), respectively (**Figure 4.6 Ci**). Although changes in fibres' shell and core sizes were observed for all days and groups, it was not significantly different for all ($p >0.05$).

Overall, this study provides an overview of the changes in different fibres' structures when cultured for 28 days, between the day it was printed and the time-point of interest.

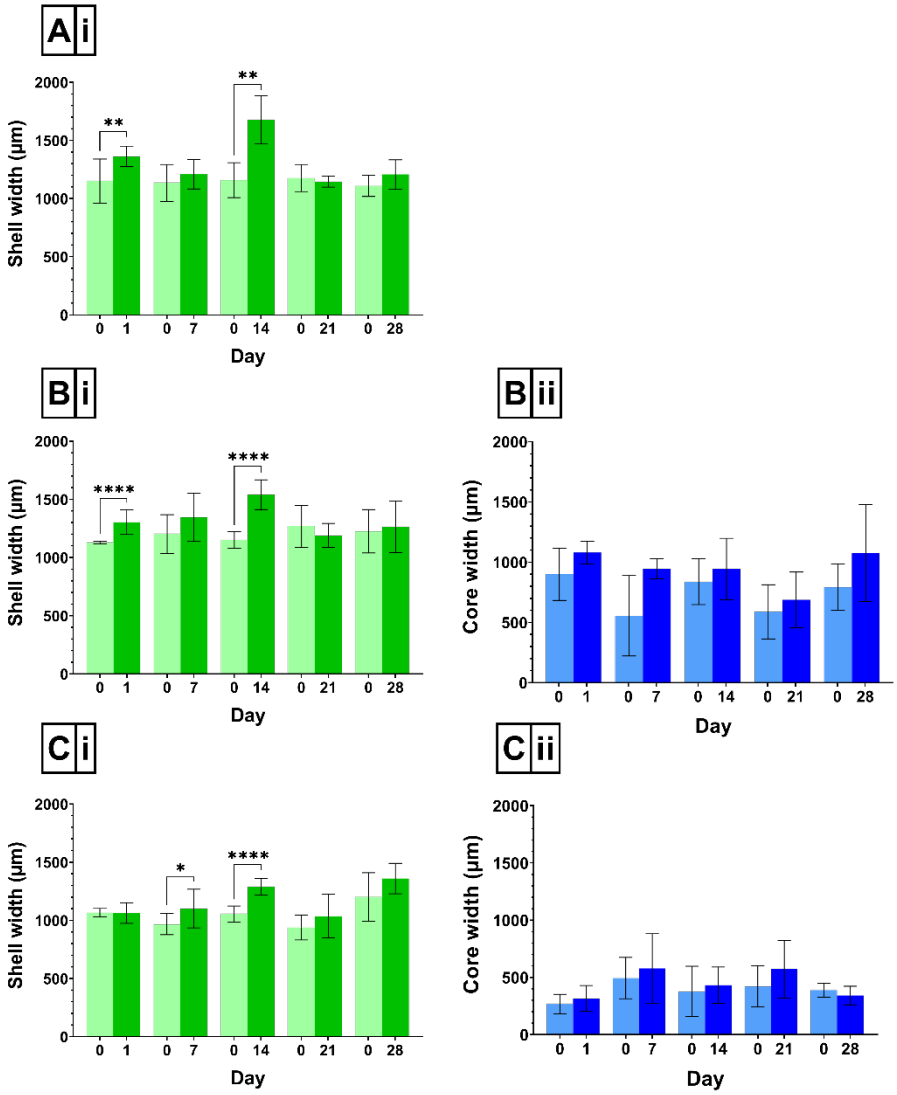


Figure 4. 6: The width of different fibres' shell is influenced by culture for 28 days. The types of cell-encapsulated fibres tested were: (**A**) solid and (**B**) core-shell fibres composed of 2 wt% alginate only and (**C**) core-shell fibres made of 2 wt% alginate and 2 wt% gelatine blends. Extrusion flow rates used were 2000 µl.min^{-1} for shell (**A-C**) and 1500 µl.min^{-1} for core (**B-C**). Width measurement data for all fibres' shell size are presented in the green graph (**Ai – Ci**) and core size measurements for core-shell fibres are presented in blue graphs (**Bii and Cii**). Day 0 represents the measurements taken of the fibres' structure on the day it was printed for the corresponding Day bar it is presented with. Data are shown as mean ± SD of one independent experiment, representative of pooled measurements from multiple samples. Statistical analysis using a two-tailed parametric and non-parametric t-test — on normally distributed and skewed data, respectively — between Day 0 and the corresponding day was carried out ($p \leq 0.05$). * $p \leq 0.05$, ** $p \leq 0.01$, *** $p \leq 0.001$, **** $p \leq 0.0001$. Non-significant results ($p > 0.05$) are not labelled on the graph. N = ranges between 3-16 for shell, and 3-13 for core.

W_{core}/W_{shell}

The temporal changes in two types of cell-encapsulated alginate fibres' W_{core}/W_{shell}, over a 28-day culture period, were measured to investigate the differences in fibre's wall thickness over time (**Figure 4.7**). The types of groups tested were alginate-only fibres with a core-shell (Group B) structure and alginate-gelatine blend core-shell fibres composed of 2 wt% alginate and 2 wt% gelatine (Group C). The days the measurements were taken were Day 1, 7, 14, 21 and 28 and the day when samples were first printed. For example, a fibre printed for Day 1 was measured on the day it was printed (Day 0) and one day later (Day 1).

For each test group, the width of fibres' W_{core}/W_{shell} was statistically compared between the day the fibre was printed and the day of interest when the measurements were taken. Statistical analysis using a two-tailed parametric and non-parametric t-test — on normally distributed and skewed data, respectively — between Day 0 and the corresponding day was carried out. Although changes in fibres' W_{core}/W_{shell} were observed for all days and groups, it was not significantly different ($p > 0.05$).

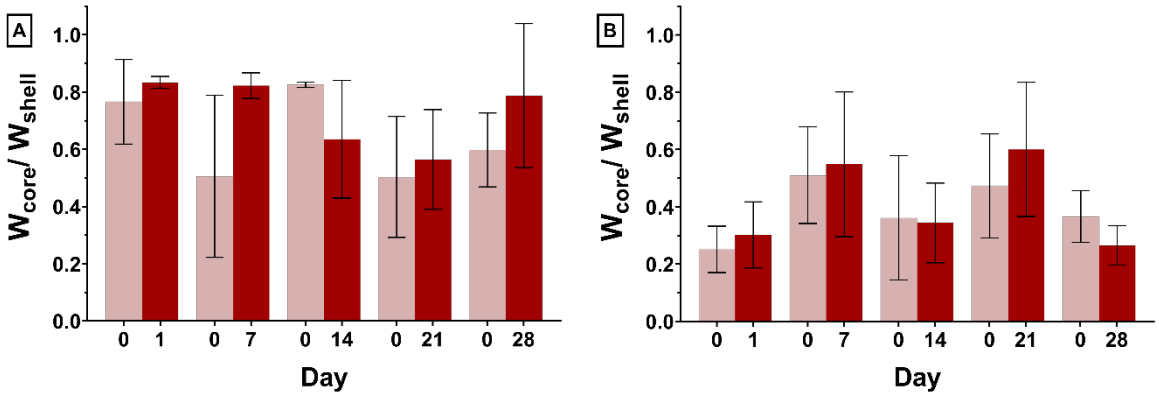


Figure 4. 7: The W_{core}/W_{shell} of different fibres when cultured for 28 days. The types of cell-encapsulated fibres presented are: (**A**) core-shell fibres composed of 2 wt% alginate only and (**B**) fibres made of 2 wt% alginate and 2 wt% gelatine blends. Extrusion flow rates used were 2000 µl.min^{-1} for shell and 1500 µl.min^{-1} for core. Day 0 represents the measurements taken of the fibres' structure on the day it was printed for the corresponding Day bar it is presented with. Data are shown as mean ± SD of one independent experiment, representative of pooled measurements from multiple samples. Statistical analysis using a two-tailed parametric and non-parametric t-test — on normally distributed and skewed data, respectively — between Day 0 and the corresponding day was carried out ($p \leq 0.05$). Non-significant results ($p > 0.05$) are not labelled on the graph. N = ranges between 3-13.

4.2.2. Testing different incubation and storage conditions

4.2.2.1. Effect of storage conditions on fibre's morphology

Camera photos were taken to visually inspect the changes in alginate core-shell fibres, cultured in various conditions for 28-day period (**Figure 4.8**). Fibres were printed under the same conditions and bathed in 10 wt% $CaCl_2$. Subsequently, the fibres were cultured under different conditions. Group A fibres were cultured in supplemented DMEM with FBS, Group B fibres were cultured in supplemented DMEM without FBS, and Group C and D fibres were cultured in RO water. Group A - C were incubated at 37 °C, while Group D was stored in a 4 °C fridge. Each image in **Figure 4.8**. represents an individual fibre, not the same fibre imaged over time.

Based on the camera photos in **Figure 4.8**, distinct trends can be observed in the structural integrity of alginate core-shell fibres between test conditions for different days. In Groups C and D, the fibres consistently maintain their integrity throughout the 28-day culture, as shown by their continuous intact (as one fibre) presence in the images for all days. However, for Group C, the visibility of the fibre is poor due to the image taken with the culture-dish's lid present, as a result of an infection on Day 21 and Day 28, which limits clarity. In contrast, fibres in Groups A and B displayed a different trend over time. Fibres initially appeared intact on Day 0 when printed but afterwards broke into pieces from being in culture from Day 1 onwards. Interestingly, Group A and B fibres appear as translucent, causing poor visualisation and had to be observed by swaying the plate to allow the varied lighting

conditions which could not be captured through the camera lens for still images. A white dotted line is used to outline the fibres that are not clearly visible.

Overall, the images in **Figure 4.8** demonstrate the structural integrity of alginate core-shell fibre cultured under various conditions for a 28-day period and give insight on the differences between test groups.

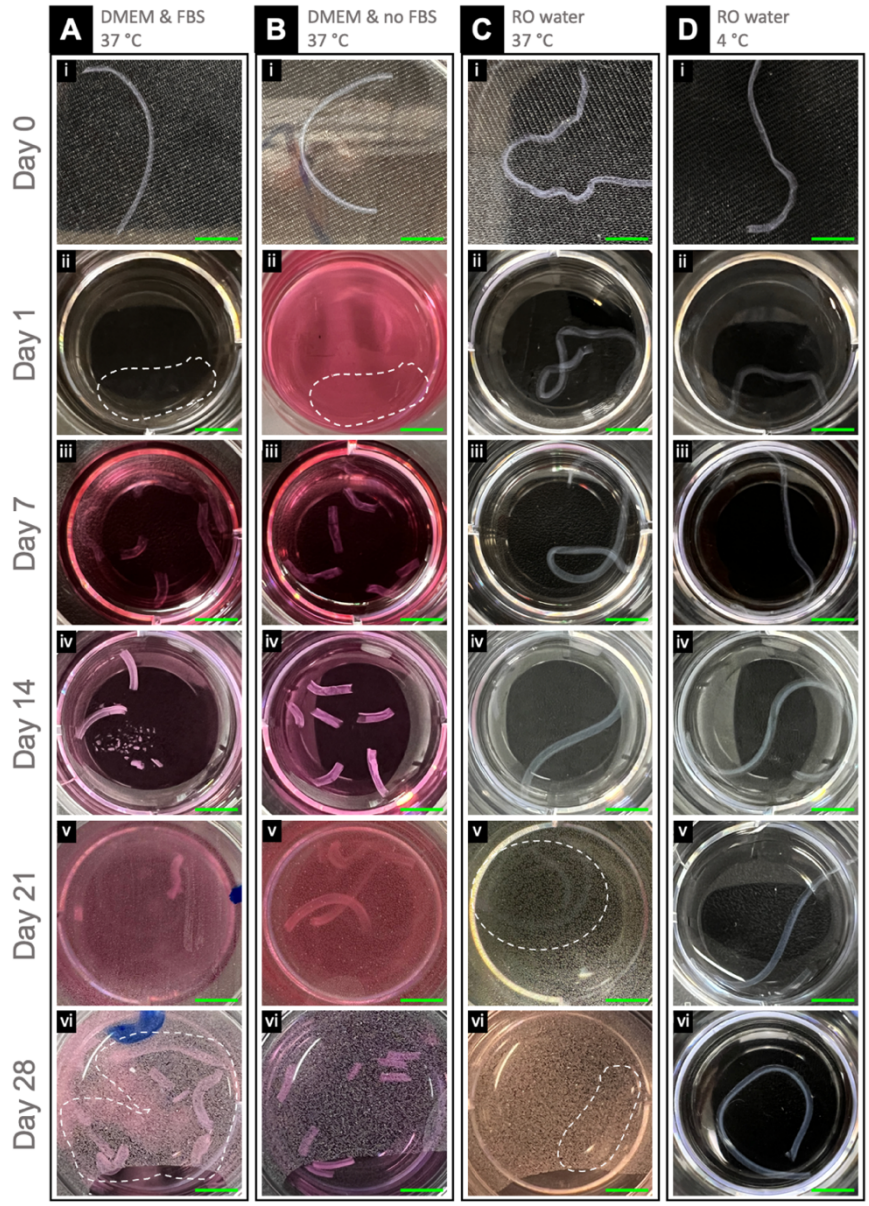


Figure 4. 8: Camera photos of alginate core-shell fibres cultured in various conditions for a 28-day period. Alginate fibres printed under the same conditions were tested in various cell culture conditions. Cell culture conditions tested were: (**A**) supplemented DMEM with FBS at 37 °C, (**B**) supplemented DMEM without FBS at 37 °C, (**C**) RO water at 37 °C, and (**D**) RO water at 4 °C. Media was changed regularly. Each image represents an individual fibre that was printed specifically for the day the images were taken. Each row within the figure represents a specific day when images were acquired (Day 1, 7, 14, 21 and 28) for all groups, allowing for a visual comparison of fibre's morphology over time. For groups **A – C** on Day 21 and Day 28, infection occurred so the images could not be taken clearly without the lid for those time points. White dotted line is used to highlight the fibres that were not clearly visible. Scale bar: 5 mm.

The temporal changes in cell-free alginate core-shell fibres' morphology were observed using phase-contrast microscopy, over a 28-day culture period (**Figure 4.9**). Fibres were printed under the same conditions but cultured under different conditions. Group A fibres were cultured in supplemented DMEM with FBS, Group B fibres were cultured in supplemented DMEM without FBS, and Group C and D fibres were cultured in RO water. Group A - C were incubated at 37 °C, while Group D was stored in a 4 °C fridge. Each image in **Figure 4.9** represents an individual fibre, not the same fibre imaged over time. Days the images were taken are Day 1, 7, 14, 21 and 28 (**Figure 4.9 i-vi**).

The temporal phase-contrast images of fibres illustrate the visual changes in fibres shell overtime for each test group (**Figure 4.9 i-vi**). The shell of the fibres predominantly appears intact for all test groups across time, however, fibres from Group A and B exhibit swelling and translucency compared to Groups C and D, for Day 1 time-point (**Figure 4.9 ii**). Another noteworthy finding is the gradual darkening and browning of the fibres colour over time, for Group A and B, while fibres in Group C and D keep the same visual appearance (**Figure 4.9 iii & iv**). It is important to note that the culture media was changed regularly, confirming the change was not due to aging of media. The absence of Day 21 and Day 28 images for Group A-C is due to the infection of cell culture plates (**Figure 4.9 v & vi**).

Overall, these phase-contrast images reveal progressive changes in Group A and B fibres' structure, including swelling of the shell on Day 1 and darkening over time, while fibres in Group C and D remained unchanged (confirmed up to Day 14 for Group C). These qualitative observations suggest dynamic remodelling within the

alginate hydrogel matrix over a long period of culture for fibres cultured in supplemented DMEM at 37 °C.

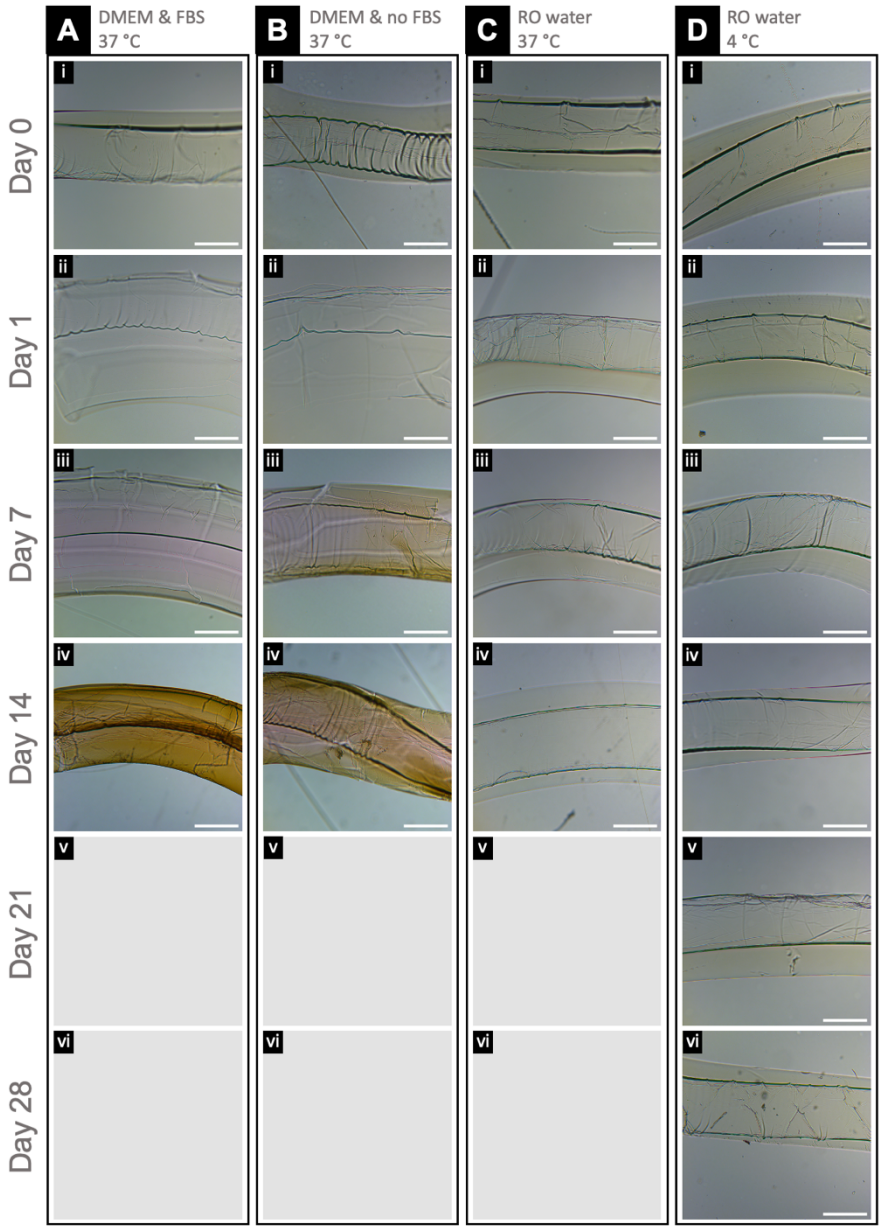


Figure 4. 9: Phase-contrast images of temporal changes in core-shell alginate fibres cultured under various conditions. Alginate fibres printed under the same conditions were tested in various cell culture conditions. Cell culture conditions tested were: (**A**) supplemented DMEM with FBS at 37 °C, (**B**) supplemented DMEM without FBS at 37 °C, (**C**) RO water at 37 °C, and (**D**) RO water at 4 °C. Media was changed regularly. Each image represents an individual fibre that was printed specifically for the day the images were taken. Each row within the figure represents a specific day when images were acquired (Day 1, 7, 14, 21 and 28) for all groups, allowing for a visual comparison of fibre's morphology over time. For groups **A – C** on Day 21 and Day 28, infection occurred so the images could not be taken for those time points. Scale bar: 500 µm.

4.2.2.2. Effect of storage conditions on fibre's core and shell

Width of fibre's core and shell

The temporal changes in 2 wt% core-shell alginate fibres' core and shell width, printed under the same conditions, but tested in various cell culture media and conditions were investigated (**Figure 4.10**). Cell culture media and conditions tested were supplemented DMEM with FBS at 37 °C (Group A), supplemented DMEM without FBS at 37 °C (Group B), RO water at 37 °C (Group C), and RO water at 4 °C (Group D). The days the measurements were taken were Day 1, 7, 14, 21 and 28 and the day when samples were first printed. For example, a fibre printed for Day 1 was measured on the day it was printed (Day 0) and one day later (Day 1).

For each test group, the width of fibres' shell and core was statistically compared between the day the fibre was printed and the day of interest when the measurements were taken. Statistical analysis using a two-tailed parametric and non-parametric t-test — on normally distributed and skewed data, respectively — between Day 0 and the corresponding day was carried out.

A significant increase in fibre's shell size was observed for some samples from the day they were initially printed. For group A, the increase in fibre's mean shell size from the day it was printed and on Day 1 was 521.5 μm ($p<0.0001$), on Day 7 was 443.8 μm ($p<0.0001$) and on Day 14 was 152.5 μm ($p= 0.0037$) (**Figure 4.10 Ai**). For group B, the increase in fibre's mean shell size from the day it was printed and on Day 1 was 445.6 μm ($p <0.0001$), on Day 7 was 371.7 μm ($p= 0.0001$) and on Day 14 was 270.1 μm ($p<0.0001$) (**Figure 4.10 Bi**). For group C, the increase in fibre's

mean shell size from the day it was printed and on Day 7 was 99.38 μm (p= 0.0296) (**Figure 4.10 Ci**). For group D, the increase in fibre's mean shell size from the day it was printed and on Day 7 was 47.37 μm (p= 0.0426), on Day 21 was 86.95 μm (p= 0.0158) and on Day 28 was 77.57 μm (p= 0.0428) (**Figure 4.10 Di**).

Additionally, a significant change in fibre's core size was observed for some samples from the day they were initially printed. For group A, the increase in fibre's mean core size after 7 days was 130.40 μm (p = 0.0360) but decreased for Day 14 by 144.30 μm (p 0.0079) (**Figure 4.10 Aii**). For group D, the increase in fibre's mean core size from the day it was printed and on Day 7 was 24.90 μm (p= 0.0475), and on Day 21 was 73.91 μm (p= 0.0250) (**Figure 4.10 Dii**).

Although changes in fibres shell and core sizes were observed for all days and groups, it was not significantly different for all ($p > 0.05$). Moreover, lack of data for Day 21 and Day 28 for groups A-C meant that fibres' core and shell sizes for those groups could not be compared fully. Nonetheless, **Figure 4.10** provides an overview of the changes in different fibres' structures when cultured under various conditions for at least 14 days.

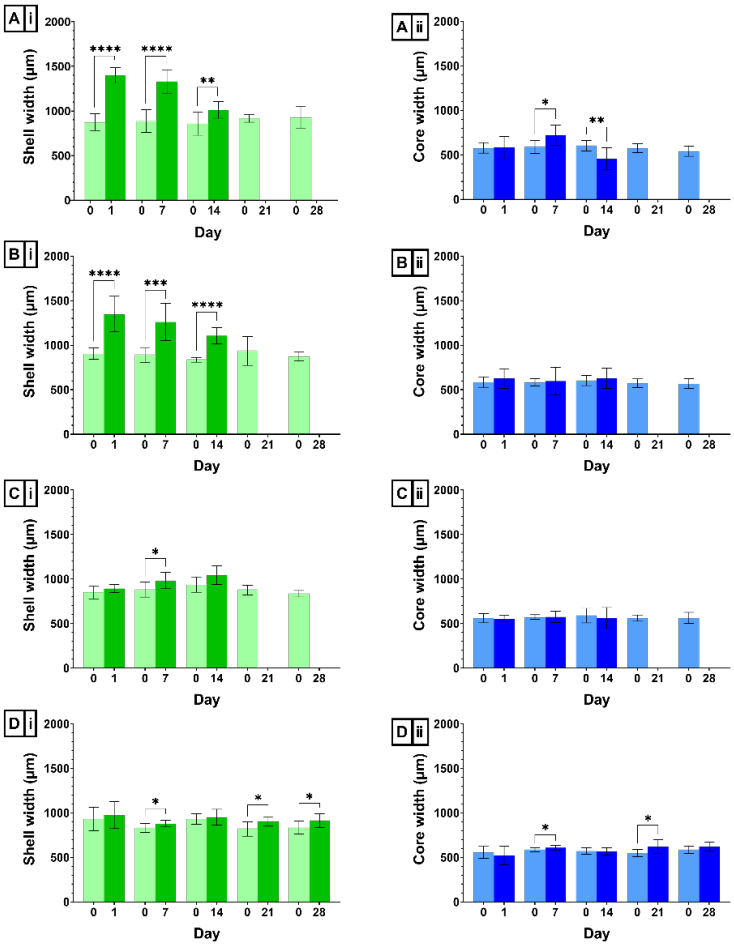


Figure 4. 10: Temporal changes in core-shell alginate fibres' shell and width size when cultured under various conditions for 28 days. Alginate fibres printed under the same conditions were tested in various cell culture conditions. Cell culture media and conditions tested were: (**A**) supplemented DMEM with FBS at 37 °C, (**B**) supplemented DMEM without FBS at 37 °C, (**C**) RO water at 37 °C, and (**D**) RO water at 4 °C. Media was changed regularly. Extrusion flow rates used were 2000 µl.min^{-1} for shell and 1500 µl.min^{-1} for core. Width measurement data for all fibres' shell size are presented in the green graph (**Ai – Di**) and core size measurements for core-shell fibres are presented in blue graphs (**Aii – Dii**). Day 0 represents the measurements taken of the fibres' structure on the day it was printed for the corresponding Day bar it is presented with. Data are shown as mean ± SD of one independent experiment, representative of pooled measurements from multiple samples. Missing data for Day 21 and Day 28 for groups **A-C** are due to the loss of samples to infection. Statistical analysis using a two-tailed parametric and non-parametric t-test — on normally distributed and skewed data, respectively — between Day 0 and the corresponding day was carried out ($p \leq 0.05$). * $p \leq 0.05$, ** $p \leq 0.01$, *** $p \leq 0.001$, **** $p \leq 0.0001$. Non-significant results ($p > 0.05$) are not labelled on the graph. N = ranges between 8-11.

W_{core}/W_{shell} of different fibres

The temporal changes in 2 wt% core-shell alginate fibres' W_{core}/W_{shell}, printed under the same conditions, but tested in various cell culture media and conditions was investigated (**Figure 4.11**). Cell culture media and conditions tested were supplemented DMEM with FBS at 37 °C (Group A), supplemented DMEM without FBS at 37 °C (Group B), RO water at 37 °C (Group C), and RO water at 4 °C (Group D). The days the measurements were taken were Day 1, 7, 14, 21 and 28 and the day when samples were first printed. For example, a fibre printed for Day 1 was measured on the day it was printed (Day 0) and one day later (Day 1).

For each test group, the width of fibres' W_{core}/W_{shell} was statistically compared between the day the fibre was printed and the day of interest when the measurements were taken. Statistical analysis using a two-tailed parametric and non-parametric t-test — on normally distributed and skewed data, respectively — between Day 0 and the corresponding day was carried out.

A significant increase in fibre's W_{core}/W_{shell} was observed for some samples from the day they were initially printed. For group A, the decrease in fibre's mean W_{core}/W_{shell} from the day it was printed and on Day 1 was 0.25 ($p<0.0001$), on Day 7 was 0.13 ($p=0.0137$), and on Day 14 was 0.26 ($p<0.0001$) (**Figure 4.11 A**). For group B, the decrease in fibre's mean W_{core}/W_{shell} from the day it was printed and on Day 1 was 0.18 ($p = 0.0014$), on Day 7 was 0.18 ($p = 0.0074$) and on Day 14 was 0.16 ($p=0.0004$) (**Figure 4.11 B**). For group C, the decrease in fibre's mean W_{core}/W_{shell} from the day it was printed and on Day 14 was 0.095 ($p= 0.0074$) (**Figure 4.11 C**).

Although changes in fibres W_{core}/W_{shell} were observed for all days and groups, it was not significantly different for all ($p > 0.05$). Moreover, lack of data for Day 21 and Day 28 for groups A-C meant that fibres' W_{core}/W_{shell} for those groups could not be compared fully. Nonetheless, **Figure 4.11** provides an overview of the changes in different fibres' structures when cultured under various conditions for at least 14 days.

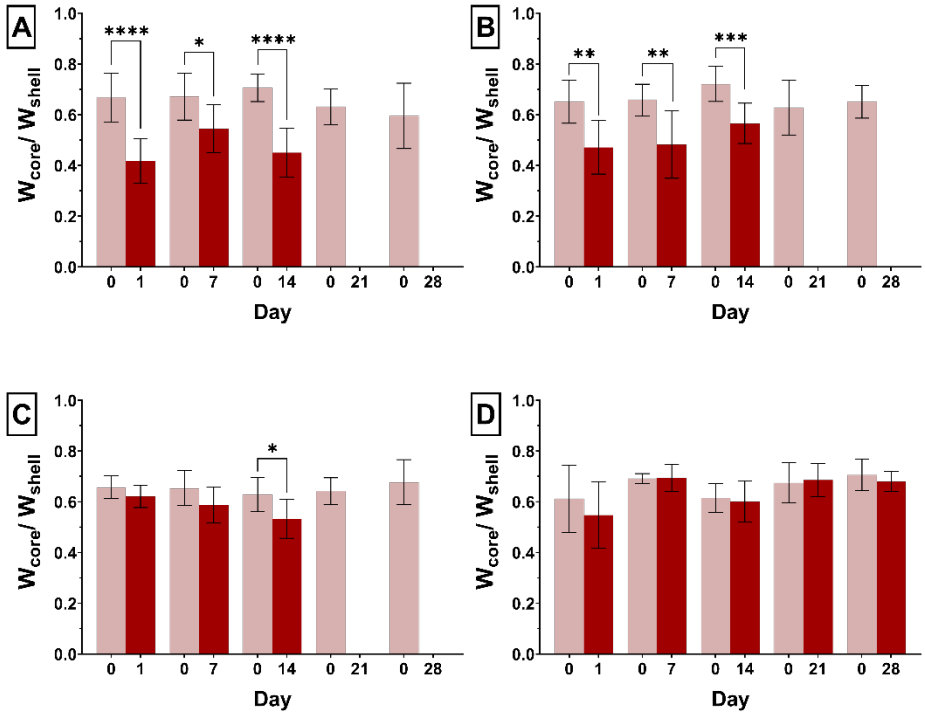


Figure 4. 11: Temporal changes in core-shell alginate fibres' W_{core}/W_{shell} when cultured under various conditions for 28 days. Alginate fibres printed under the same conditions were tested in various cell culture conditions. Cell culture media and conditions tested were: (**A**) supplemented DMEM with FBS at 37 °C, (**B**) supplemented DMEM without FBS at 37 °C, (**C**) RO water at 37 °C, and (**D**) RO water at 4 °C. Media was changed regularly. Extrusion flow rates used were 2000 $\mu l.min^{-1}$ for shell and 1500 $\mu l.min^{-1}$ for core. Day 0 represents the measurements taken of the fibres' structure on the day it was printed for the corresponding Day bar it is presented with. Data are shown as mean ± SD of one independent experiment, representative of pooled measurements from multiple samples. Missing data for Day 21 and Day 28 for groups **A-C** are due to the loss of samples to infection. Statistical analysis using a two-tailed parametric and non-parametric t-test — on normally distributed and skewed data, respectively — between Day 0 and the corresponding day was carried out ($p \leq 0.05$). * $p \leq 0.05$, ** $p \leq 0.01$, *** $p \leq 0.001$, **** $p \leq 0.0001$. Non-significant results ($p > 0.05$) are not labelled on the graph. N = ranges between 8-11.

4.3. Discussion

4.3.1. Testing different types of fibres

This study was carried out to investigate the changes in viability of 3T3s encapsulated in fibres and the structure of those fibres during prolonged 3D cell culture for more than 24 hours.

4.3.1.1. Cell viability and morphology

To investigate the changes in viability between cell-encapsulated fibres with different structures when cultured for 28 days, this experiment was carried out. The types of groups tested were two alginate-only fibres with a solid (Group A) and core-shell (Group B) structure, and alginate-gelatine blend core-shell fibres composed of 2 wt% alginate and 2 wt% gelatine (Group C). Analysis between Groups at a specific timepoint (Day), showed significant differences in cell viability. Group B had a significantly higher viability compared to Group A on Day 1 and Day 14. This meant that the extrusion through the novel microfluidics-based chip did not have a negative impact on cell viability. This interpretation could have been further supported by the generally higher cell viability on other days too, however the overlapping error bars caused no significant difference to be reported. Cell viability when gelatine is added to the shell solution was significantly lower than Group B (alginate-only) 24 hours after culture (Day 1), however, the differences fluctuated throughout the remaining culture period of 28 days.

For comparison between Days for each group, significant differences in viability were observed for all groups. Based on significant difference analysis, cells embedded in solid alginate-only fibres improved in cell viability between Day 1 and Day 21. While cells embedded in core-shell alginate-only fibres improved in cell viability between Day 1 and Day 7, the cell viability reduced by Day 21. Cells embedded in core-shell alginate-gelatine fibres consistently improved in cell viability between Day 1, 7 and 14. From these results, it can be interpreted that the viability of cells embedded in fibres with gelatine added improves over 14-day culture. However, the viability of cells, embedded in fibres with no gelatine added, decreases over 21-day culture, despite the initial rise in cell viability between Day 1 and Day 7. This is very likely due to the lack of adhesive molecules on alginate, causing the cells to escape the gel matrix as the fibre breaks in culture over time. Escape of cells from the alginate hydrogels has been previously reported by Fannon et al. (2021) due to degradation gel in culture overtime (180).

The trend in data could also be due to samples taken from areas of the initially printed fibre that had more cells which survived printing conditions, than other areas. This can explain the viability of cells embedded in core-shell alginate-only fibres to be below 80% on Day 1 but above 80% on Day 7. Cells embedded in solid alginate-only and core-shell alginate-gelatine fibres also had a viability below the ISO standard (< 70%) after 24 hours of culture (164). This supports the interpretation that the low cell viability, after 24 hours of culture, is not due to the extrusion of cells through the novel microfluidics-based chip. This is because even the solid fibres had a low cell viability after 24 hours of culture, contrary to the >80% viability in **section 3.2.2.1.** Additionally, there was no significant difference between other samples on the graph

which can be explained by large error bars. Therefore, in the future, it is best to measure the viability of cells repeatedly on the same sample for each timepoint, under sterile conditions, so a more controlled comparison can be made.

Furthermore, the 3T3s that were incapsulated in these fibres, remained rounded overtime. The lack of cell growth over time could be because of cells entering non-proliferative phase (G0) of cell cycle due to no cell attachment to the material (167).

4.3.1.2. Fibre morphology and structure

Study in this section was carried out to investigate if the thickness of the fibre's wall changes or if the fibre's shell degrades overtime. Measurements of the shell and core's width, and their ratio revealed that the size of core-shell alginate fibre fluctuated when cultured in DMEM over the period of 28 days. This was supported by the observations made from phase-contrast images which revealed progressive changes in fibres' structure, including cracking in the shell wall and darkening, which suggested dynamic remodelling within the hydrogel matrix over a long period of culture. Alginate gels are sensitive to compounds such as phosphate or cations such as sodium or magnesium which can interfere with the calcium-alginate binding (168). This can cause degradation of the gel and cause mechanical instability (180). The swelling of fibres can be explained by water uptake in the fibres as the fibre structure expands due to de-crosslinking caused by sodium in the DMEM (180,181). The cracking of the outer shell can be explained by the constant exposure of the outer layer to non-gelling cations and calcium chelating compounds creating a break in the fibre's wall (180). Perhaps this degradation of the gel could also explain the reduction

in cell number (both red and green) for fibres on 28th day in **section 4.2.1.1.** as the cells were escaping the fibre's structure and washed away in the media.

Degradation of a hydrogel can be beneficial on one hand to allow the hydrogel to be broken down and removed once an endothelial tube has formed. However, uncontrolled degradation of the hydrogel fibre can also result in weaking and rupturing of the developing endothelial wall. Additionally, it is important to study the degradation of fibres further because when the fibres are perfused in future studies, they will need to have a structurally robust to be able to withstand the sheer stress from fluid flow.

4.3.2. Testing different incubation and storage conditions

The cause behind morphological changes of the fibre, such as shell and core structure, when cultured for 28 Days as seen in **section 4.2.1**, needed to be investigated. Although blood vessels *in vivo* remodel structurally according to the changes in nutritional and oxygen demands of the tissue they are supplying to, it is a highly controlled process (182). It is important to study the changes in structure of the core-shell fibre (i.e., blood vessel mimic) overtime because if the size of shell (i.e., vessel wall) increases it will result in an increased porosity of the fibre's wall which will affect the diffusion of nutrients and molecules into the ECM. Similarly, if the core (i.e., lumen) of the fibre changes in size overtime, it can cause changes in the blood flow dynamics to the target tissue or organ. Therefore, it is crucial to study the

structural changes of the hydrogel fibres, produced to mimic the blood vasculature, to ensure that their function is controlled to achieve the desired outcome.

This study was designed to determine if it was mainly the DMEM, FBS, or the temperature of incubation that was causing the browning of the fibres. The reason behind the use of 2 wt% alginate-only core-shell fibre in this study is because it was one of the fibres that was browning and turning opaque in previous study (**section 4.2.1**). Once there is any indication of what the reason behind the structural changes of the fibre could be, then the experiment could be repeated in the future with gelatine core-shell fibres for comparison.

4.3.2.1. Fibre morphology and structure

The observations made from the phone camera images were that the fibres that were incubated (37 °C) or stored (4 °C) in water did not brown or become opaque overtime. Additionally, these fibres remained intact over time and their shell did not crack like the fibres in Group A and B. These fibres were also easy to handle during transfer from culture well to the petri dish for observations under the microscope. In contrast, fibres that were cultured in DMEM with FBS (Group A) and without FBS (Group B) displayed a different opacity of the fibres over time. Fibres initially appeared intact on Day 0 when printed but afterwards broke into pieces from being in culture from Day 1 onwards. Interestingly, Group A and B fibres appeared translucent 24 hours after culture at 37 °C, causing poor visualisation and had to be observed by swaying the plate to allow the varied lighting conditions which could not be captured through the camera lens for still images.

Measurements of the shell and core's width, and their ratio revealed that the size of core-shell alginate fibre fluctuated when cultured in DMEM over the period of 14 - 28 days. This was supported by the observations made from the phase-contrast images which showed that while the shell of the fibres predominantly appeared intact for all test groups across time, fibres from Group A and B exhibited swelling and translucency compared to Groups C and D, for Day 1 time-point. This made it difficult to see the fibres with and without the microscope. Presence of Ca^{2+} in the DMEM solution is supposed to maintain the integrity of the fibres in culture as reported by Andersen et al. (2014), however, we observed that the fibres that were kept in water were more structurally intact than the fibres that were kept in DMEM, regardless of the temperature (168). The amount of $CaCl_2$ present in our sample was 0.2mg/ml according to the manufacturers (183). Another interesting contrast between our data are that their cells were spreading inside the 3D gel from 6 to 23 days of culture, while the cells in this study (**section 4.2.1.1.**) remained rounded (168).

4.3.2.2. Cause of fibre degradation

In this section, the potential reasons behind the structural changes of the fibres overtime will be discussed to narrow down the real reason behind the issue.

Firstly, printing conditions such as extrusion flow rates and bath duration in $CaCl_2$ cannot be the issue in Group A and B fibres turning brown, going transparent and becoming delicate from Day 1. This is because the aforementioned changes were observed for Group A and B only and not for Group C and D, despite all of the printing conditions being kept the same for all groups. Pluronic F127, used for core solution, also cannot be the cause behind changes in fibres morphology. This is

because in **section 4.2.1.**, alginate-only solid fibres (without the core) would not have changed morphologically, as they did not have the Pluronic F127 present. Also, the reason behind the browning of the fibres could not be due impure pigments in the alginate. This is because all sample were made from sodium alginate and the fibres for RO water would have browned too.

Secondly, the temperature cannot be the cause behind changes in fibres morphology. This is because the fibres' that were kept in incubator at 37 °C in RO water looked unaffected morphologically compared to their Day 0 samples over time. Similarly, the fibres kept in the 4 °C fridge in water also remained unchanged over time. In order to strengthen this interpretation of the data, fibres in DMEM (with FBS and without FBS) should be stored at 4 °C as well next time, to see if the temperature change alters the effects of DMEM.

Thirdly, the FBS cannot be the cause behind changes in fibres' morphology because the fibres that were kept in Group B (without FBS) turned transparent, became delicate and looked brown. If it was because of the FBS, the changes would have been observed only in Group A (with FBS) and not Group B (without FBS). Therefore, it further narrows down something being in the DMEM (other than FBS) that was causing the browning of the fibres. The DMEM did seem to be the factor as both A and B Groups appeared brown on Day 7 and Day 14. Also, the fibres broke very easily, and some pieces were dissolved in media and washed away during media change for DMEM Groups (A & B). This was not observed in Group C and D with water. Therefore, the reason could be due to the oxidation of tryptophan present in the DMEM cell culture media, as reported previously to be the cause behind

browning of alginate gels (184). The DMEM used during this project had a tryptophan concentration of 0.016 mg/ml (183).

The significance of these finding is that the issue in structural changes of the fibres overtime is due to the materials used (i.e., sodium alginate) and not the novel microfluidics-based chip. Therefore, in the future, structural integrity of the sodium alginate will need to be enhanced through ligand conjugation, such as with the RGD motifs. This is because the presence of RGD ligand in alginate hydrogels have previously shown increased viability, proliferation, and migration of cells, while the mechanical stability of the gel was further supported by cell-ECM interaction (181,185–187).

4.4. Limitations of the study

The results presented in this chapter are obtained from just one experimental repeat for each study (**sections 4.2.1 and 4.2.2.**), due to the short duration of the project. This can explain the large error bars and variation in some data. Therefore, multiple experimental repeats should be carried out with the suggested optimisation steps to ensure consistency in data and a clear trend to be determined. Nevertheless, this study provided an overview of the changes in viability between cell-encapsulated fibres with different structures when cultured for 28 days.

It should be noted that only the temporal changes in cell-free fibres' morphology were observed under different culture conditions (**section 4.2.2**.). Although the potential causes behind fibre degradation were highlighted in **section 4.3.2.2.,** cell-encapsulated fibres should also be cultured alongside cell-free fibres in future

studies. This should provide clarification if any cell-related factors are contributing towards fibre's degradation overtime, as observed particularly in **section 4.2.1.**

Fibres that were kept in 37 °C incubator (Group A, B and C) were infected on Day 21 and Day 28 for **section 4.2.2.** Day 21 plate was infected first, followed by plate for Day 28 few days afterwards. Therefore, the images for measurements could not be taken on their specific timepoints for these samples. Lack of data for Day 21 and Day 28 for groups A-C meant that fibres' core and shell sizes for those groups could not be compared fully. Photo images taken for visual observation were poor quality due to the culture-dish's lid present that could not be removed. This limits the clarity in the changes being observed for long term studies. The media was changed regularly and was freshly aliquoted from stock solution. 3T3s being cultured in the flask for other studies at the same time, did not show any infection otherwise the reason for infection could have been narrowed down to infection of the media. The samples were kept separately, in a box in the incubator in order to prevent infection from other samples in case there was an infection from other's work. The reason behind the infection, therefore, is very likely due to the opening of the lid outside of the flow hood, or the tips used for this experiment. Nonetheless, this experiment provided an overview of the changes in different fibres' structures when cultured under various conditions for at least 14 days.

4.5. Summary

Overall, this study provides an overview of the changes in different fibres' structures when cultured for 28 days, between the day it was printed and the time-point of interest. Additionally, cell viability measurements demonstrated that the loss of cells overtime due to the degradation of fibres in media. Therefore, structural integrity of alginate core-shell fibres, cultured under various conditions for a 28-day period, was carried out to gain insight into the differences among the test groups. Findings revealed progressive changes in fibre's structure that were cultured in DMEM (with FBS and without FBS), including swelling of the shell from Day 1 and darkening over time, while fibres kept in water remained unchanged (confirmed up to Day 14 for fibres in 37 °C). These observations suggest dynamic remodelling within the alginate hydrogel matrix, over a long period of culture, for fibres cultured in supplemented DMEM at 37 °C.

5. Perfusion of fibres to mimic blood flow

5.1. Introduction

Having successfully printed the hollow core-shell fibres in **sections 3.2.1. and 3.2.3.**, perfusion test of the fibres needed to be carried out to mimic blood flow and confirm fibre's ability to function as blood vessel mimics. The reason why it is important to test the flow of fluid through the fibre's core is to ensure that the fibre has a continuous core from which fluid can be flowed without any blockage. Furthermore, by perfusing the hollow fibres to mimic blood flow, the potential of these fibres to be used for generating vascularised bone tissues will be determined.

Additionally, in order to create a fully functioning blood vessel mimic, the fibre needs to be cannulated to allow constant flow of fluid through the fibre. This is because when the cells are cultured in the fibre, such as SMCs and HUVECs in fibres and MSCs outside the fibre to form bone tissue, they will need to be supplied with oxygen and nutrients for development. Therefore, in this chapter, methods to create a set-up like organ-on-a-chip model would be explored with a potential as a 'nutrient circulation system' (188).

5.2. Results

5.2.1. Perfusion test

5.2.1.1. Fibres printed using varying extrusion flow rates of core solution

In order to test the hollow structure of the fibre's core and its perfusion for mimicking blood vessels, the hollow alginate fibres were perfused with blue dye solution using the siphoning method (**Figure 5.1**). Alginate fibres, printed using extrusion core flow rates of (**Figure 5.1 A**) 125, (**Figure 5.1 B**) 250, (**Figure 5.1 C**) 500, (**Figure 5.1 D**) 1000, (**Figure 5.1 E**) 1500, (**Figure 5.1 F**) 2000 $\mu l.min^{-1}$, with a constant shell flow rate of 2000 $\mu l.min^{-1}$, were tested.

The time-lapse images show the before and after state of fibres during the perfusion process (**Figure 5.1 ii-iv**). These images clearly demonstrate that all fibres have a continuous core present, from one end of the fibre to the other, that can be perfused without interruptions in the flow of blue dye solution. Notably, the uniformity of the perfusion throughout the fibres is evident from these images, as no localised areas of blockage or irregular flow patterns were observed. The blue dye solution flowed through the core of the fibre from one end and mixed into the clear water bath as it flowed out from the other end of the fibre. For **Figure 5.1 F**, the reason there is a leakage in the fibre is because the fibre broke during the handling for imaging after it was perfused. The perfused area after the leakage proves that the fibre had a

continuous core initially. These results emphasise the structural integrity of the fibre's core and their ability to be perfused with a consistent flow of fluid.

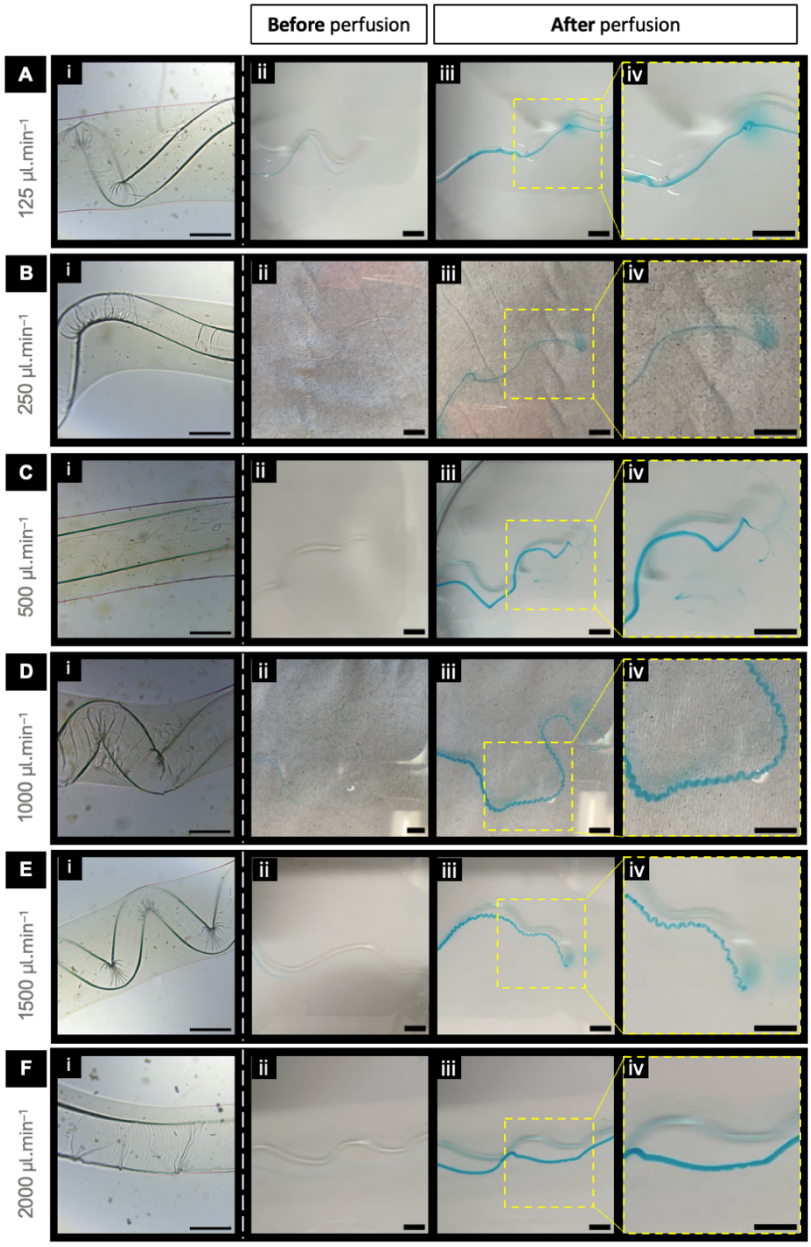


Figure 5. 1: Perfusion test of alginate core-shell fibres. Time-lapse images demonstrating blue dye flowing through the core of hollow alginate fibres. Fibres were perfused using the siphoning method, with one end in a tube containing blue dye, while the other end of the fibre was in a petri dish containing water. Fibres extruded using core flow rates of **A)** 125 µl.min^{-1}, **B)** 250 µl.min^{-1}, **C)** 500 µl.min^{-1}, **D)** 1000 µl.min^{-1}, **E)** 1500 µl.min^{-1}, **F)** 2000 µl.min^{-1} were tested, with a constant shell flow rate of 2000 µl.min^{-1}. **A – F (i)** show phase-contrast images of core-shell fibres' structure, while the corresponding camera images **(ii & iv)** for each group show the before and after perfusion of these fibres with blue dye. Close-up of each perfused fibre is also provided **(iv)**. Scale bar: 500 µm for **A – F (i)**, and 5 mm for **A – F (ii-iv)**.

5.2.1.2. Fibres printed using varying gelatine concentrations

Core-shell fibres with different compositions of gelatine in alginate-gelatine blends were perfused, as shown in **Figure 5.2 (i-iv).** Fibres with gelatine added to alginate-gelatine blend (**Figure 5.2**) were compared with the control group (0 wt%) with no gelatine added (**Figure 5.2**). Optical images show the visual evidence of fibres' before and after perfusion with blue dye thus confirming successful perfusion of these fibres with fluid, except for the 10 wt% group due to a lack of core. Therefore, **Figure 5.2**. illustrates the successful perfusion of core-shell fibres using 2 and 6 wt% gelatine in alginate-gelatine blends, like the alginate-only group (0 wt%).

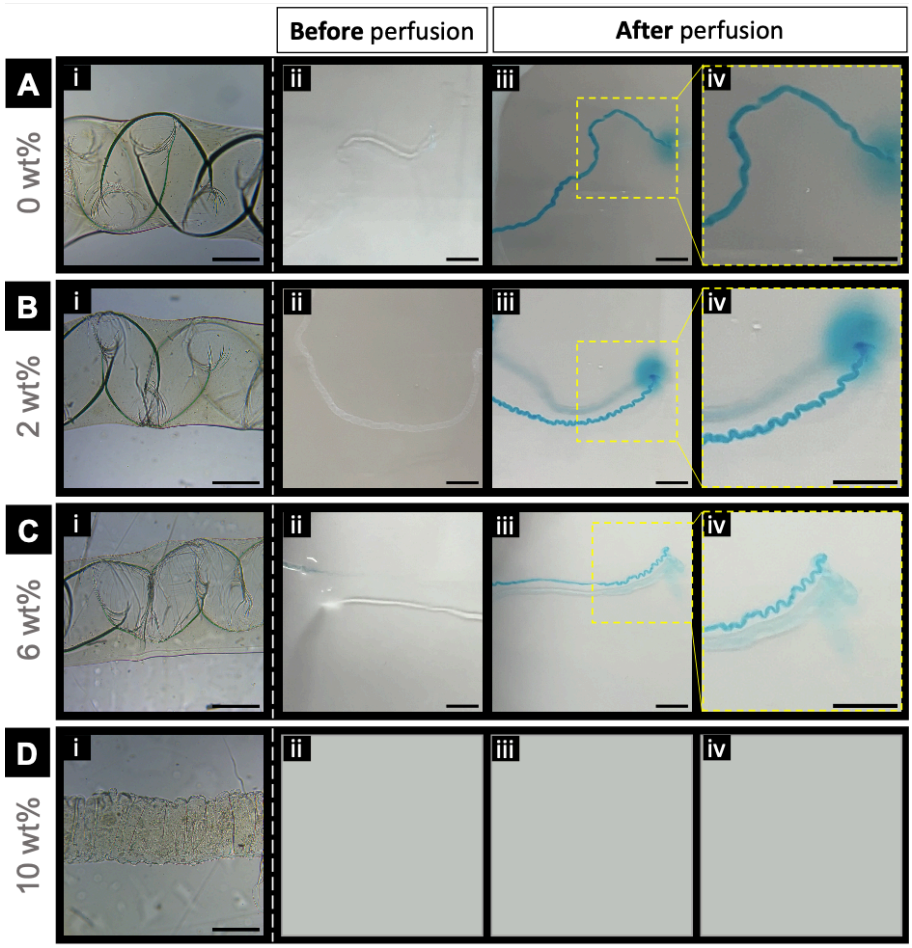


Figure 5. 2: Perfusion of alginate-gelatine core-shell fibres. Core-shell fibres with different concentrations of gelatine (2 wt% to 10 wt%) in an alginate-gelatine blend were printed and perfused. Alginate concentration was kept as 2 wt%. **A - D (i)** show phase-contrast images of core-shell fibres' structure, while the corresponding camera images **(ii & iii)** for each group show the before and after perfusion of these fibres with blue dye. Close-up of each perfused fibre is also provided in **A-C (iv)**. Fibres printed with 10 wt% gelatine did not have a core and thus could not be perfused as shown in **D (ii-iv)**. Scale bar: 500 µm for **A-D (i)**, and 5 mm for **A - C (ii-iv)**.

5.2.2. Cannulation and set-up of fibre on a chip

5.2.2.1. Cannulation of fibres

Figure 5.3 shows time-lapse images of the perfusion process of a hollow alginate fibre. The fibre was cannulated with a 30G needle, using a PDMS block with hollow area to hold the fibre in place. Thus, precision and control required to hold the needle into the fibre's core is illustrated. Subsequently, blue dye solution was perfused through the fibre's core from one end to the other. The sequence of images demonstrates the movement of blue fluid along the fibre's core, gradually filling the internal structure. Low opacity of the alginate fibre's shell allowed the visual representation of the perfusion process in the core.

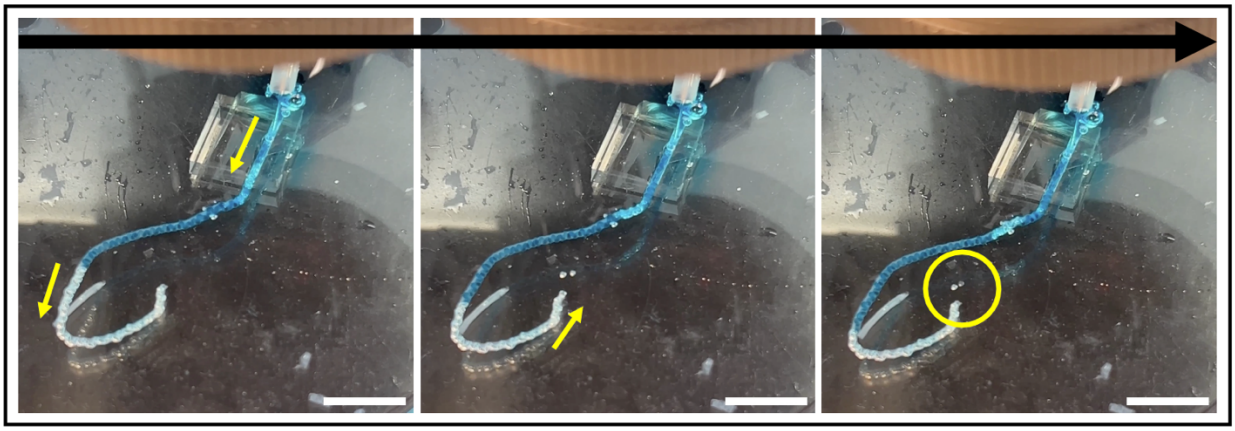


Figure 5. 3: Cannulation of a core-shell fibre. The fibre with a core size of 500 µm (±50 µm) was cannulated with a 30G needle and perfused with blue dye mixed in water. Black arrow indicates the order of images. Yellow arrows indicate the flow of dye through the fibre's core and yellow circle highlights the bubbles released from the open end of the fibre, indicating the flow of dye through the fibre. Scale: 50 mm.

5.2.2.2. Setting up channels with fibres

A hollow core-shell alginate fibre was inserted into an ibidi channel with the aim to create a microfluidic system. However, upon sticking the coverslip to the bottom of the ibidi channel, the hydrogel fibre was compressed and deformed due to limited space, as shown in **Figure 5.4**. Rather than the round morphology of the fibre, as seen from the ends sticking out from the channels, the fibre exhibited a flattened morphology upon compression between ibidi channel and coverslip. Additionally, 30 wt% Pluronic solution which was poured into the channels around the fibre was not strong enough to hold the fibre in place for cannulation with a needle.

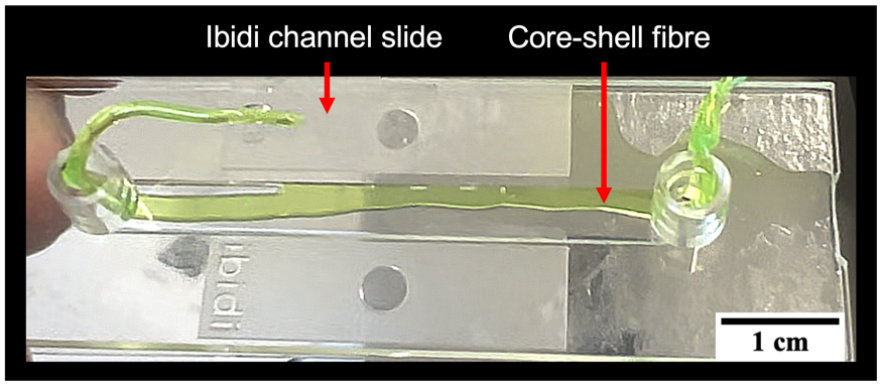


Figure 5. 4: Photographic images of fibre set up in a channel slide. A core-shell fibre was threaded through the channel of an ibidi slide with ends coming out of the two channels. The polymer coverslip stuck to the bottom-side of the ibidi slide pressed and flattened the fibre against the channel. 30 wt% Pluronic solution in the channels was not strong enough to hold the fibre in place for cannulation with a needle. Scale: 1 cm.

5.3. Discussion

5.3.1. Perfusion test

In order to confirm the hollow structure of the fibre's core and its perfusion for mimicking blood vessels, siphoning effect was used to test the movement of blue dye from one end of the fibre's core to the other.

5.3.1.1. Fibres printed using varying core flow rates

The images of fibres' perfusion in **section 5.2.1.1.** clearly demonstrate that all fibres had a continuous core present, from one end of the fibre to the other, that can be perfused without interruptions in the flow of blue dye solution. The helical and straight cores inside the fibres could be seen clearly from the transparent shells of the fibres, similar to other core-shell fibres in literature (96,154). These results emphasised the structural integrity of the fibre's core, printed using various core flow rates (125 $\mu l.min^{-1}$– 2000 $\mu l.min^{-1}$), and their ability to be perfused with a consistent flow of fluid to mimic blood flow.

5.3.1.2. Fibres printed using varying gelatine concentrations

The blue dye successfully flowed through the core-shell fibres printed with 0 wt%, 2 wt% and 6 wt% gelatine blend groups but not for 10 wt%. Images showed

that the blue dye was only leaking out from the end of the fibres and mixing into the bath solution. This is a noteworthy finding because it showed that there were no leakages in the fibre wall even if gelatine was added to the shell solution, alongside alginate. This finding means that the addition of gelatine did not have a negative effect on fibre's shell integrity during perfusion.

5.3.1.3. Future directions

The diffusion of substances from the fibres shell could be studied to see if the dye or specific molecules leak out of the shell (96,144,189). Jia et al. (2019) reported that if the cross-linking of alginate and Ca^{2+} is increased, then the fibre's wall becomes less permeable (96). However, if the cross-linking of fibres wall is increased, more permeability and leakage of perfused fibres is observed, as shown by fluorescein isothiocyanate-labelled bovine serum albumin (FITC-BSA) leakage from the fibre's wall (96). Therefore, further studies should be carried out to investigate the permeability of the fibre's shell using FITC-BSA technique. This will allow the desired manipulation of the fibre's shell according to the specific studies. For example, if the researchers want to enhance the diffusion of VEGF or drugs from the fibre's core to the cells, then the permeability of the fibre's shell can be increased by reducing the cross-linking of fibre's shell materials. Alternatively, if the researchers want to reduce the diffusion of molecules from the fibre's core to the cells seeded in ECM, then the permeability of the fibre's shell can be decreased by increasing the cross-linking of fibre's shell materials in specific areas. Additionally, SEM should be carried out on the fibre's core in a cross-section view to observe the hollow nature

and wall structure of the alginate-gelatine fibre and support the findings of perfusion tests (110,189,190).

The fibre that was outside of the fluid started to dry and shrink during perfusion (>1 minute later). Therefore, in future studies, the fibres can be prevented from drying out by perhaps coating the exposed area of the fibre with Pluronic solution which gels at room temperature and can act as a barrier between alginate fibres and the air (191).

5.3.2. Cannulation and set-up of fibre on a chip

Although siphoning effect was a sufficient method to test the perfusion, it does not provide control over the speed of fluid flowing through the fibre. Control over the perfusion rate is important because it will allow a controlled delivery of the drugs to the bone cells through the fibre in future studies. Previously, a needle has been used to cannulate and perfuse the hollow fibres with a syringe pump to control perfusion flow rate through the fibre's core (96). Therefore, a setup with cannulated fibres set in an organ-on-a-chip style could be very useful to control the perfusion and function of these hollow core-shell fibres. Furthermore, the concept behind setting up the cannulation channels is to create a multi-channel perfusion system using the core-shell fibres that can be perfused and cultured simultaneously to allow rapid prototyping in the future. In this section, the use of a needle to cannulate the fibres and ibidi channels to create a channel set-up of the core-shell fibres is discussed.

5.3.2.1. Cannulation of fibres

Having established that the fibres do have a continuous core, using the siphoning method (**section 5.2.1.**), a core-shell fibre was cannulated with a 30G needle for perfusion. The needle was attached to a syringe with blue dye in it, which was perfused through the fibre from one end to the other.

First challenge was to cannulate the fibre. When the fibre was held in hand, it was too delicate to be held with even a gentle force to insert the needle, as it would crush and block the fibre's core. Therefore, a block of PDMS cut from a spare microfluidic chip, with an ID of about 1 mm, was used to hold one end of the fibre. With delicate movements and difficult attempt, the fibre was successfully inserted and held inside the PDMS block. A needle was injected into the PDMS block where the fibre was, as shown in **Figure 5.3**. One end of the fibre was inside the PDMS block, and the other end was inside the water. Blue dye was pumped through the fibre using a syringe attached to an extrusion pump. The dye did seem to flow through the fibre's core at first, as seen by the bubbles being formed in the water. However, the fibre slipped out of the PDMS block, possibly due to pressure.

Although reproducing the results in this section were difficult and need optimisation, nonetheless this study showed that the fibres could be cannulated by holding the fibre in a PDMS block to reduce movement of the fibre during perfusion. Perhaps a transparent epoxy adhesive can be used to glue the fibre to needle, as done by Jia et al. (2019) (96). This intervention should prevent the fibre from slipping out of the PDMS block during perfusion.

5.3.2.2. Setting up channels with fibres

The aim behind set-up of fibres in ibidi channels was to have a single hollow core-shell fibre going through the channel with bone cells seeded on the sides of the fibre. Additionally, the goal was to fix the fibres in the slide to limit the movement of the fibre for cannulation and provide constant hydration to prevent the drying out of the fibre. However, when the fibre was inserted inside the channel of the ibidi slide, the fibre was crushed between the slide and the plastic cover, which was glued to bottom of the slide. In the future, this issue can be resolved by creating a custom slide with larger channel height of 2 mm, compared to the ibidi channel slide which had a channel height of 0.8 mm (192). This should allow a 1 mm fibre to be placed inside the channel with extra room for additional cells to be seeded around it. The concentration of Pluronic solution used as a glue should either be increased (perhaps to 50 wt%) or a hydrophilic adhesive can be used to fix the fibre ends in the reservoirs of the ibidi channel before cells are seeded (193). Another thing to consider when designing the custom channel in the future, is to ensure transparency of the channel, that will allow the visualisation of cell behaviour under a microscope. Finally, when making a custom channel slide, the channels should be designed at a 45° angle, rather than the 90° angle of the ibidi channel, to further ease the insertion of capillary in the fibre.

5.3.2.3. Future directions

Previously, peristaltic pumps have been used to control flow rate of media through the fibre's core by altering the pressure in chambers (194,195). Therefore, in

future studies, a variety of perfusion methods should be tested to find the best one for our hydrogel fibres. Additionally, fluorescent labelled microspheres can be used to microscopically image the flow of fluids through the fibre's core (196). Once the structural integrity of the fibres and cannulation method is optimised, the fibres should be integrated into bone tissue scaffolds to create a perfusable vascularised bone scaffold for tissue engineering.

5.4. Limitations of the study

A hollow fibre, printed using the flow rates of 2000 µl.min^{-1} for shell and 1500 µl.min^{-1} for core, was cannulated with a needle for perfusion in this study. With optimisation, fibres with smaller cores, printed using slower core flow rates, can be tested in the future too. Referring to **section 4.2.1.**, the cell-encapsulated fibres (Group B and C) were too delicate to be perfused for the perfusion test. Fibre pieces were also too small (< 3 cm long) to be held and tested using siphoning effect. However, once the structure of the fibres is optimised in future studies, cell-encapsulated fibres should be cannulated and perfused with media for prolonged cell culture (28 days). This will allow the investigation into the effect of prolonged perfusion on fibre's structure and morphology.

Notably, the results reported in this study for cannulation and set-up of fibres were preliminary studies and will require troubleshooting and optimisation in the future. Due to complexity of the fibre's cannulation and set-up, the priority was given to other studies in this project to gather enough repeats for statistical analysis. Nonetheless, siphoning method was sufficient during this project to confirm the continuous core and perfusion of the fibres to mimic blood flow.

5.5. Summary

In this section, the fibres were perfused using siphoning method to confirm the continuous hollow nature of the fibre's core. Preliminary data for cannulation and ibidi

channel set-up were also presented. However, the preliminary methods explored in this section should be further investigated and improved in future studies.

6. Conclusions

Despite the increasing cases of bone fracture incidences, as well as the limitations with current bone transplant methods, there is a shortage of bone tissue donors. This has impelled research into tissue engineering strategies for bone regeneration, which has shown some promising results. However, existing tissue engineering strategies face some drawbacks, especially in supplying physiologically relevant levels of oxygen and nutrients to cells within the bone tissue scaffolds. To resolve this issue, a novel microfluidics-based chip for 3D-printing vascular structures was developed by researchers at the School of Dentistry, University of Birmingham. The purpose of this research project was to investigate the efficacy of this novel microfluidic-based chip for fabricating hollow cell-compatible fibres, which are structurally adjustable, durable and can be perfused to mimic physiological blood flow for tissue engineering purposes.

6.1. Major outcomes

The major outcomes of this project are highlighted below, which correspond with the **objectives** in **Chapter 1, section 1.6.**:

1. This project demonstrated that a range of hollow core-shell fibres can be generated with a defined width and geometry by changing the extrusion flow rates of core solutions through the microfluidic-based chip between 125 $\mu l.min^{-1}$– 2000 $\mu l.min^{-1}$, while keeping the flow rate of shell constant at 2000 $\mu l.min^{-1}$. Straight, wavy and helical core shapes were generated that have the

potential to be used for recapitulating different flow rates found physiologically.

2. Assessment of the printing conditions for cell viability revealed that 10 wt% (100 mg/ml) $CaCl_2$ in the bath solution provides optimal cell viability (> 80%), compared to 2 wt% (20 mg/ml) and 4 wt% (40 mg/ml), as well as structural integrity of the 2 wt% (20 mg/ml) sodium alginate fibres.

3. To optimise the biocompatibility of materials used for the hollow fibre's shell, cytotoxicity, cell adhesion and cell morphology were assessed. Results revealed that, 2 wt% gelatine blended with alginate at 1:1 concentration supported cell adhesion while ensuring core-shell fibres to be printed with ease.

4. Long-term studies were carried out to learn the impact of incubation period on different fibres, to determine the areas of improvement for future studies. It was revealed that alginate fibres (whether core and gelatine present or not) degraded in cell culture media over the 28 days of culture. Although, the viability of cells embedded in core-shell fibres with gelatine added was observed to be improving for the first 7 days of culture, the variation in data meant that no clear trend could be observed at this stage.

5. To confirm that the cause behind fibre degradation was the structure of alginate and components of DMEM media, alginate core-shell fibres were incubated in DMEM (with and without FBS) and water, and stored at 37 °C and 4 °C. Results from this study and the literature review revealed that it was in fact non-gelling cations, calcium chelating compounds and tryptophan

present in DMEM media that were causing the fibre's degradation and morphological changes, such as darkening and opaqueness.

6. The hollow core-shell fibres were perfused using gravity and cannulation to confirm the structural integrity and uniformity of the fibre's core for replicating blood flow. Fibres printed using a blend of alginate and gelatine concentrations were successfully perfused, except the fibres with 10 wt% gelatine, due to a lack of core.
7. Finally, cannulation methods and loading of fibres on a chip to create a set-up that can be used for testing the efficacy of fibres in future studies were explored. Areas of improvement were identified, such as the design of the set-up channels to ensure an easy and reproducible set-up for further studies.

6.2. Future work

Key areas of improvement and suggestions for future projects are outlined below:

- Although a range of hollow core-shell fibres can be generated, temperature of the core solution needs to be regulated at 4 °C to ensure consistency in fibre and helical pitch formation for each test group. This should allow a clear relationship between flow rates of solutions and the fibre structure to be determined.

- In addition to the optimisation of printing conditions, such as temperature regulation to allow homogonous composition of materials, gelatine with higher concentrations should be tested. Higher concentrations of gelatine in the alginate-gelatine blends are hypothesised to increase cell adhesion to the material. However, care should be taken to ensure that enough alginate is present in the blend to allow crosslinking of material with Ca^{2+} ions during printing.
- Components of the DMEM media were observed to cause degradation and morphological changes, such as darkening and opaqueness, of the alginate fibre. Therefore, to avoid this, modification of the hollow fibre's shell solution needs to be carried out to enhance the structural integrity of fibres overtime. This intervention is imperative to ensure that the hydrogel fibres can withstand long-term culture and perfusion with media in future studies.
- Thermal regulation of the shell and core solution during printing is required. This is because most of the materials used for fibre generation, particularly Pluronic® F-127 and gelatine, are temperature sensitive. Therefore, during printing of the fibres, the temperature of the solutions can fluctuate and cause disparities in the core formation. Thermal regulation of the shell and core solution during printing should allow this issue to be fixed in future studies.
- For the long-term culture of hollow fibres with HUVECs and SMCs (for creating blood vessel mimics) consistent perfusion of cell culture medium through the fibre's core is required. To achieve this, cannulation method and loading of fibres in channels to create a set-up were explored. However, due

to the fragile nature of the fibre's hydrogel structure, customisation of the set-up is required to ensure perfusion of fibres in culture without any damage and disruption.

- In future studies, the current microfluidic based printing system should be refined to create hollow hydrogel fibres that are comparable to those of the microcirculation, particularly capillaries. Either capillary mimics should be 3D-printed, or larger hollow tubes should be induced to grow micro vessels through the process of angiogenesis. Such smaller vessels should allow appropriate diffusion of relevant substances such as oxygen, carbon dioxide and metabolites between the plasma and tissue parenchymal cells. Ultimately, this would allow a wide range of vasculature systems to be generated for bone tissue engineering or testing of novel therapeutics.

This research project revealed that hollow core-shell fibres with a range of core shapes, printed using the novel microfluidic-based chip, can be perfused to mimic blood flow. With some optimisation, the fibres have the potential to be used in fabricating vascularised bone tissue scaffolds, to meet the increasing demands of organ donors for bone transplantation.

7. List of References

1. Wu AM, Bisignano C, James SL, Abady GG, Abedi A, Abu-Gharbieh E, et al. Global, regional, and national burden of bone fractures in 204 countries and territories, 1990–2019: a systematic analysis from the Global Burden of Disease Study 2019. Lancet Healthy Longev. 2021 Sep 1;2(9):e580–92.

2. Guillén-Carvajal K, Valdez-Salas B, Beltrán-Partida E, Salomón-Carlos J, Cheng N. Chitosan, Gelatin, and Collagen Hydrogels for Bone Regeneration. Polymers 2023, Vol 15, Page 2762. 2023 Jun 21;15(13):2762.

3. Shen Y, Huang X, Wu J, Lin X, Zhou X, Zhu Z, et al. The Global Burden of Osteoporosis, Low Bone Mass, and Its Related Fracture in 204 Countries and Territories, 1990-2019. Front Endocrinol (Lausanne). 2022 May 20;13:1.

4. Gullberg B, Johnell O, Kanis JA. World-wide projections for hip fracture. Osteoporosis International. 1997;7(5):407–13.

5. Weatherholt AM, Fuchs RK, Warden SJ. Specialized connective tissue: bone, the structural framework of the upper extremity. Journal of Hand Therapy. 2012;25(2):123.

6. Su N, Yang J, Xie Y, Du X, Chen H, Zhou H, et al. Bone function, dysfunction and its role in diseases including critical illness. Int J Biol Sci. 2019;15(4):776.

7. Šromová V, Sobola D, Kaspar P. A Brief Review of Bone Cell Function and Importance. Cells 2023, Vol 12, Page 2576. 2023 Nov 5;12(21):2576.

8. Florencio-Silva R, Sasso GRDS, Sasso-Cerri E, Simões MJ, Cerri PS. Biology of Bone Tissue: Structure, Function, and Factors That Influence Bone Cells. Biomed Res Int. 2015;2015.

9. Office of the Surgeon General (US). The Burden of Bone Disease. In: Bone Health and Osteoporosis: A Report of the Surgeon General. Office of the Surgeon General (US); 2004.

10. Clarke B. Normal Bone Anatomy and Physiology. Clin J Am Soc Nephrol. 2008;3(Suppl 3):S131.

11. Yeung AY, Arbor TC, Garg R. Anatomy, Sesamoid Bones. In: StatPearls. StatPearls Publishing; 2023.

12. Biga LM, Bronson S, Dawson S, Harwell A, Hopkins R, Kaufmann J, et al. 6.2 Bone Classification. In: Anatomy and Physiology 2e. OpenStax/Oregon State University; 2022.

13. Lumen Learning. Types of Bone | Biology for Majors II [Internet]. [cited 2024 Oct 9]. Available from: https://courses.lumenlearning.com/wm-biology2/chapter/types-of-bone/

14. Cowan PT, Launico M V., Kahai P. Anatomy, Bones. In: StatPearls. StatPearls Publishing; 2024.

15. Denst J, Mulligan RM. THE DISTRIBUTION OF BONE MARROW IN THE HUMAN STERNUM. Am J Clin Pathol. 1950 Jul 1;20(7):610–3.

16. Altalib AA, Miao KH, Menezes RG. Anatomy, Thorax, Sternum. In: StatPearls. StatPearls Publishing; 2023.

17. National Cancer Institute. Classification of Bones | SEER Training [Internet]. [cited 2024 Oct 9]. Available from: https://training.seer.cancer.gov/anatomy/skeletal/classification.html

18. Nahian A, Chauhan PR. Histology, Periosteum And Endosteum. In: StatPearls. StatPearls Publishing; 2023.

19. Biga LM, Bronson S, Dawson S, Harwell A, Hopkins R, Kaufmann J, et al. 6.3 Bone Structure. OpenStax/Oregon State University; 2019.

20. Dwek JR. The periosteum: what is it, where is it, and what mimics it in its absence? Skeletal Radiol. 2010 Apr;39(4):319.

21. Benjamin M, Toumi H, Ralphs JR, Bydder G, Best TM, Milz S. Where tendons and ligaments meet bone: attachment sites (‘entheses’) in relation to exercise and/or mechanical load. J Anat. 2006 Apr;208(4):471.

22. Henry JP, Bordoni B. Histology, Osteoblasts. In: StatPearls. StatPearls Publishing; 2023.

23. Ansari M. Bone tissue regeneration: biology, strategies and interface studies. Prog Biomater. 2019 Dec 1;8(4):223.

24. Amirazad H, Dadashpour M, Zarghami N. Application of decellularized bone matrix as a bioscaffold in bone tissue engineering. Journal of Biological Engineering 2021 16:1. 2022 Jan 5;16(1):1–18.

25. Osterhoff G, Morgan EF, Shefelbine SJ, Karim L, McNamara LM, Augat P. Bone mechanical properties and changes with osteoporosis. Injury. 2016 Jun 1;47(Suppl 2):S11.

26. Baig MA, Bacha D. Histology, Bone. In: StatPearls. StatPearls Publishing; 2023.

27. Robey PG. Bone Matrix Proteoglycans and Glycoproteins. Principles of Bone Biology. 2002 Jan 1;225–37.

28. Hart NH, Newton RU, Tan J, Rantalainen T, Chivers P, Siafarikas A, et al. Biological basis of bone strength: anatomy, physiology and measurement. J Musculoskelet Neuronal Interact. 2020 Sep 1;20(3):347.

29. Schaffler MB, Kennedy OD. Osteocyte Signaling in Bone. Curr Osteoporos Rep. 2012 Jun;10(2):118.

30. Che Z, Sun Y, Luo W, Zhu L, Li Y, Zhu C, et al. Bifunctionalized hydrogels promote angiogenesis and osseointegration at the interface of three-dimensionally printed porous titanium scaffolds. Mater Des. 2022 Nov 1;223:111118.

31. Yi H, Ur Rehman F, Zhao C, Liu B, He N. Recent advances in nano scaffolds for bone repair. Bone Res. 2016 Dec 13;4:16050.

32. Saul D, Menger MM, Ehnert S, Nüssler AK, Histing T, Laschke MW. Bone Healing Gone Wrong: Pathological Fracture Healing and Non-Unions—Overview of Basic and Clinical Aspects and Systematic Review of Risk Factors. Bioengineering 2023, Vol 10, Page 85. 2023 Jan 9;10(1):85.

33. Holmes D. Non-union bone fracture: a quicker fix. Nature 2017 550:7677. 2017 Oct 26;550(7677):S193–S193.

34. Perez JR, Kouroupis D, Li DJ, Best TM, Kaplan L, Correa D. Tissue Engineering and Cell-Based Therapies for Fractures and Bone Defects. Front Bioeng Biotechnol. 2018 Jul 31;6:105.

35. Schlundt C, Bucher CH, Tsitsilonis S, Schell H, Duda GN, Schmidt-Bleek K. Clinical and Research Approaches to Treat Non-union Fracture. Curr Osteoporos Rep. 2018 Apr 1;16(2):155–68.

36. Jimi E, Hirata S, Osawa K, Terashita M, Kitamura C, Fukushima H. The current and future therapies of bone regeneration to repair bone defects. Int J Dent. 2012;

37. Chen EP, Toksoy Z, Davis BA, Geibel JP. 3D Bioprinting of Vascularized Tissues for in vitro and in vivo Applications. Front Bioeng Biotechnol. 2021;9:326.

38. DEPLAIGNE V, ROCHEFORT GY. Bone tissue engineering at a glance. AIMS Bioengineering 2022 1:22. 2021;9(1):22–5.

39. Rademakers T, Horvath JM, van Blitterswijk CA, LaPointe VLS. Oxygen and nutrient delivery in tissue engineering: Approaches to graft vascularization. J Tissue Eng Regen Med. 2019 Oct 1;13(10):1815–29.

40. Aitken G, Hill G. Benefits and associated risks of using allograft, autograft and synthetic bone fusion material for patients and service providers - A Systematic Review. JBI Libr Syst Rev. 2010;8(Supplement):1–13.

41. Lee JH, Parthiban P, Jin GZ, Knowles JC, Kim HW. Materials roles for promoting angiogenesis in tissue regeneration. Prog Mater Sci. 2021 Apr 1;117:100732.

42. Li Y, Liu Y, Bai H, Li R, Shang J, Zhu Z, et al. Sustained Release of VEGF to Promote Angiogenesis and Osteointegration of Three-Dimensional Printed Biomimetic Titanium Alloy Implants. Front Bioeng Biotechnol. 2021 Nov 15;9:757767.

43. Chen Y, Chen S, Kawazoe N, Chen G. Promoted Angiogenesis and Osteogenesis by Dexamethasone-loaded Calcium Phosphate Nanoparticles/Collagen Composite Scaffolds with Microgroove Networks. Scientific Reports 2018 8:1. 2018 Sep 20;8(1):1–12.

44. Amini AR, Laurencin CT, Nukavarapu SP. Bone Tissue Engineering: Recent Advances and Challenges. Crit Rev Biomed Eng. 2012;40(5):363.

45. Krishani M, Shin WY, Suhaimi H, Sambudi NS. Development of Scaffolds from Bio-Based Natural Materials for Tissue Regeneration Applications: A Review. Gels 2023, Vol 9, Page 100. 2023 Jan 23;9(2):100.

46. Shang F, Yu Y, Liu S, Ming L, Zhang Y, Zhou Z, et al. Advancing application of mesenchymal stem cell-based bone tissue regeneration. Bioact Mater. 2021 Mar 1;6(3):666–83.

47. Bose S, Vahabzadeh S, Bandyopadhyay A. Bone tissue engineering using 3D printing. Materials Today. 2013 Dec 1;16(12):496–504.

48. Dec P, Modrzejewski A, Pawlik A. Existing and Novel Biomaterials for Bone Tissue Engineering. International Journal of Molecular Sciences 2023, Vol 24, Page 529. 2022 Dec 28;24(1):529.

49. Duong VT, Dang TT, Lee Y, Nguyen CT, Phan HL, Shin D, et al. Cell Attachment on Inside-Outside Surface and Cell Encapsulation in Wall of Microscopic Tubular Scaffolds for Vascular Tissue-Like Formation. Proceedings of the Annual International Conference of the IEEE Engineering in Medicine and Biology Society, EMBS. 2018 Oct 26;2018-July:4198–201.

50. Hauser PV, Chang HM, Nishikawa M, Kimura H, Yanagawa N, Hamon M. Bioprinting Scaffolds for Vascular Tissues and Tissue Vascularization. Bioengineering 2021, Vol 8, Page 178. 2021 Nov 6;8(11):178.

51. Di Francesco D, Pigliafreddo A, Casarella S, Di Nunno L, Mantovani D, Boccafoschi F. Biological Materials for Tissue-Engineered Vascular Grafts: Overview of Recent Advancements. Biomolecules. 2023 Sep 1;13(9).

52. Jafarkhani M, Salehi Z, Aidun A, Shokrgozar MA. Bioprinting in Vascularization Strategies. Iran Biomed J. 2019;23(1):9.

53. Liu N, Zhang X, Guo Q, Wu T, Wang Y. 3D Bioprinted Scaffolds for Tissue Repair and Regeneration. FrMat. 2022 Jul 7;9:925321.

54. Gold KA, Saha B, Rajeeva Pandian NK, Walther BK, Palma JA, Jo J, et al. 3D Bioprinted Multicellular Vascular Models. Adv Healthc Mater. 2021 Nov 1;10(21):2101141.

55. Mandrycky C, Hadland B, Zheng Y. 3D curvature-instructed endothelial flow response and tissue vascularization. Sci Adv. 2020;6(38):3629–45.

56. WD T, Y A, K M. Anatomy, Blood Vessels. In: StatPearls. 2017.

57. Place TL, Domann FE, Case AJ. Limitations of Oxygen Delivery to Cells in Culture: An Underappreciated Problem in Basic and Translational Research. Free Radic Biol Med. 2017 Dec 1;113:311.

58. Sarveswaran K, Kurz V, Dong Z, Tanaka T, Penny S, Timp G. Synthetic Capillaries to Control Microscopic Blood Flow. Scientific Reports 2016 6:1. 2016 Feb 24;6(1):1–18.

59. Rhonda D. Prisby. Mechanical, hormonal and metabolic influences on blood vessels, blood flow and bone. J Endocrinol. 2017 Dec 1;235(3):R77.

60. Kinstlinger IS, Miller JS. 3D-printed fluidic networks as vasculature for engineered tissue. Lab Chip. 2016 May 24;16(11):2025–43.

61. Masson-Meyers DS, Tayebi L. Vascularization strategies in tissue engineering approaches for soft tissue repair. J Tissue Eng Regen Med. 2021 Sep 1;15(9):747.

62. Simitian G, Virumbrales-Muñoz M, Sánchez-De-Diego C, Beebe DJ, Kosoff D. Lab on a Chip CRITICAL REVIEW Microfluidics in vascular biology research: a critical review for engineers, biologists, and clinicians. 2022;22:3618.

63. Bogseth A, Ramirez A, Vaughan E, Maisel K. In Vitro Models of Blood and Lymphatic Vessels—Connecting Tissues and Immunity. Adv Biol. 2023 May 1;7(5):2200041.

64. Goel S, Duda DG, Xu L, Munn LL, Boucher Y, Fukumura D, et al. NORMALIZATION OF THE VASCULATURE FOR TREATMENT OF CANCER AND OTHER DISEASES. Physiol Rev. 2011;91(3):1071.

65. Wong KHK, Chan JM, Kamm RD, Tien J. Microfluidic Models of Vascular Functions. Annu Rev Biomed Eng. 2012;14(Volume 14, 2012):205–30.

66. Auerbach R, Lewis R, Shinners B, Kubai L, Akhtar N. Angiogenesis Assays: A Critical Overview. Clin Chem. 2003 Jan 1;49(1):32–40.

67. Kähler CM, Kirchmair R, Kaufmann G, Kähler ST, Reinisch N, Fischer-Colbrie R, et al. Inhibition of Proliferation and Stimulation of Migration of Endothelial Cells by Secretoneurin In Vitro. Arterioscler Thromb Vasc Biol. 1997;17(5):932–9.

68. Duong VT, Dang TT, Hwang CH, Back SH, Koo KI. Coaxial printing of double-layered and free-standing blood vessel analogues without ultraviolet illumination for high-volume vascularised tissue. Biofabrication. 2020 Sep 23;12(4):045033.

69. Suzuki S. Oxygen administration for postoperative surgical patients: a narrative review. J Intensive Care. 2020 Dec 1;8(1).

70. Pizzino G, Irrera N, Cucinotta M, Pallio G, Mannino F, Arcoraci V, et al. Oxidative Stress: Harms and Benefits for Human Health. Oxid Med Cell Longev. 2017;2017.

71. Ramakrishnan S, Anand V, Roy S. Vascular Endothelial growth factor signaling in hypoxia and Inflammation. J Neuroimmune Pharmacol. 2014;9(2):142.

72. Lee HW, Shin JH, Simons M. Flow goes forward and cells step backward: endothelial migration. Experimental & Molecular Medicine 2022 54:6. 2022 Jun 14;54(6):711–9.

73. Amar DN, Epshtein M, Korin N. Endothelial Cell Activation in an Embolic Ischemia-Reperfusion Injury Microfluidic Model. Micromachines 2019, Vol 10, Page 857. 2019 Dec 6;10(12):857.

74. Zamorano M, Castillo RL, Beltran JF, Herrera L, Farias JA, Antileo C, et al. Tackling Ischemic Reperfusion Injury With the Aid of Stem Cells and Tissue Engineering. Front Physiol. 2021 Sep 17;12:705256.

75. Cao X, Maharjan S, Ashfaq R, Shin J, Zhang YS. Bioprinting of Small-Diameter Blood Vessels. Engineering. 2021;7(6):832–44.

76. Schöneberg J, De Lorenzi F, Theek B, Blaeser A, Rommel D, Kuehne AJC, et al. Engineering biofunctional in vitro vessel models using a multilayer bioprinting technique. Scientific Reports 2018 8:1. 2018 Jul 11;8(1):1–13.

77. White HJ, Bordes SJ, Borger J. Anatomy, Abdomen and Pelvis: Aorta. In: StatPearls. StatPearls Publishing; 2023.

78. White HJ, Soos MP. Anatomy, Thorax, Superior Vena Cava. In: StatPearls. StatPearls Publishing; 2023.

79. Burton AC. On the Physical Equilibrium of Small Blood Vessels. Am J Physiol. 1951;164(2):319–29.

80. Wenceslau CF, McCarthy CG, Earley S, England SK, Filosa JA, Goulopoulou S, et al. Guidelines in Cardiovascular Research: Guidelines for the measurement of vascular function and structure in isolated arteries and veins. Am J Physiol Heart Circ Physiol. 2021 Jul 7;321(1):H77.

81. Cleveland Clinic. Arterioles: Anatomy and Function [Internet]. 2022 [cited 2024 Oct 8]. Available from: https://my.clevelandclinic.org/health/body/23377-arterioles

82. Taylor AM, Bordoni B. Histology, Blood Vascular System. In: StatPearls. StatPearls Publishing; 2023.

83. Taylor AM, Bordoni B. Histology, Blood Vascular System. In: StatPearls. 2020.

84. Mercadante AA, Raja A. Anatomy, Arteries. In: StatPearls. StatPearls Publishing; 2023.

85. Vekilov DP, Grande-Allen KJ. Mechanical Properties of Diseased Veins. Methodist Debakey Cardiovasc J. 2018 Jul 1;14(3):182.

86. Jian FG, Chu H bo, Liu GZ, Zhao JH, Xu YB, Wang T, et al. Morphological characteristics of the walls of thrombophlebitic saphenous vein. Phlebology. 2014 Apr 1;29(3):164–70.

87. Wang D, Maharjan S, Kuang X, Wang Z, Mille LS, Tao M, et al. Microfluidic bioprinting of tough hydrogel-based vascular conduits for functional blood vessels. Sci Adv. 2022 Oct 28;8(43).

88. Caggiati A, Phillips M, Lametschwandtner A, Allegra C. Valves in Small Veins and Venules. European Journal of Vascular and Endovascular Surgery. 2006 Oct 1;32(4):447–52.

89. Chaudhry R, Miao JH, Rehman A. Physiology, Cardiovascular. In: StatPearls. StatPearls Publishing; 2022.

90. Sumagin R, Sarelius IH. Emerging Understanding of Roles for Arterioles in Inflammation. Microcirculation. 2013 Nov;20(8):679.

91. Yang GH, Kang D, An SH, Ryu JY, Lee KH, Kim JS, et al. Advances in the development of tubular structures using extrusion-based 3D cell-printing technology for vascular tissue regenerative applications. Biomaterials Research 2022 26:1. 2022 Dec 5;26(1):1–13.

92. Sukriti S, Tauseef M, Yazbeck P, Mehta D. Mechanisms regulating endothelial permeability. Pulm Circ. 2014 Dec 1;4(4):535.

93. Jung B, Obinata H, Galvani S, Mendelson K, Ding B Sen, Skoura A, et al. Flow-Regulated Endothelial S1P Receptor-1 Signaling Sustains Vascular Development. Dev Cell. 2012 Sep 11;23(3):600–10.

94. Chiu JJ, Chien S. Effects of Disturbed Flow on Vascular Endothelium: Pathophysiological Basis and Clinical Perspectives. Physiol Rev. 2011 Jan;91(1):327–87.

95. Harding IC, Mitra R, Mensah SA, Herman IM, Ebong EE. Pro-atherosclerotic disturbed flow disrupts caveolin-1 expression, localization, and function via glycocalyx degradation. J Transl Med. 2018 Dec 18;16(1):1–20.

96. Jia L, Han F, Yang H, Turnbull G, Wang J, Clarke J, et al. Microfluidic Fabrication of Biomimetic Helical Hydrogel Microfibers for Blood-Vessel-on-a-Chip Applications. Adv Healthc Mater. 2019 Jul 1;8(13):1900435.

97. Melchiorri AJ, Hibino N, Best CA, Yi T, Lee YU, Kraynak CA, et al. 3D-Printed Biodegradable Polymeric Vascular Grafts. Adv Healthc Mater. 2016 Feb 4;5(3):319–25.

98. Gao Q, Liu Z, Lin Z, Qiu J, Liu Y, Liu A, et al. 3D Bioprinting of Vessel-like Structures with Multilevel Fluidic Channels. ACS Biomater Sci Eng. 2017 Mar 13;3(3):399–408.

99. Song J, Chen Z, Murillo LL, Tang D, Meng C, Zhong X, et al. Hierarchical porous silk fibroin/poly(L-lactic acid) fibrous membranes towards vascular scaffolds. Int J Biol Macromol. 2021 Jan 1;166:1111–20.

100. Zhao N, Pessell AF, Zhu N, Searson PC. Tissue-Engineered Microvessels: A Review of Current Engineering Strategies and Applications. Adv Healthc Mater. 2024 Aug 1;13(21):2303419.

101. Yang X, Forouzan O, Burns JM, Shevkoplyas SS. Traffic of leukocytes in microfluidic channels with rectangular and rounded cross-sections. Lab Chip. 2011 Sep 5;11(19):3231–40.

102. Mobarak MH, Islam MA, Hossain N, Al Mahmud MZ, Rayhan MT, Nishi NJ, et al. Recent advances of additive manufacturing in implant fabrication – A review. Applied Surface Science Advances. 2023 Dec 1;18:100462.

103. Prakash KS, Nancharaih T, Rao VVS. Additive Manufacturing Techniques in Manufacturing -An Overview. Mater Today Proc. 2018 Jan 1;5(2):3873–82.

104. Wasti S, Adhikari S. Use of Biomaterials for 3D Printing by Fused Deposition Modeling Technique: A Review. Front Chem. 2020 May 7;8:532815.

105. Jones JB. The American Society of Mechanical Engineers. AM Basics - Additive Manufacturing (AM).

106. Hou YC, Cui X, Qin Z, Su C, Zhang G, Tang JN, et al. Three-dimensional bioprinting of artificial blood vessel: Process, bioinks, and challenges. Int J Bioprint. 2023;9(4).

107. Li N, Guo R, Zhang ZJ. Bioink Formulations for Bone Tissue Regeneration. Front Bioeng Biotechnol. 2021 Feb 5;9:630488.

108. Vijayavenkataraman S, Lu WF, Fuh JYH. 3D bioprinting of skin: a state-of-the-art review on modelling, materials, and processes. Biofabrication. 2016 Sep 7;8(3):032001.

109. Gleadall A, Visscher D, Yang J, Thomas D, Segal J. Review of additive manufactured tissue engineering scaffolds: relationship between geometry and performance. Burns Trauma. 2018 Dec 1;6.

110. Moetazedian A, Candeo A, Liu S, Hughes A, Nasrollahi V, Saadat M, et al. Versatile Microfluidics for Biofabrication Platforms Enabled by an Agile and Inexpensive Fabrication Pipeline. Adv Healthc Mater. 2023;12(26).

111. Ma PX. Scaffolds for tissue fabrication. Materials Today. 2004 May 1;7(5):30–40.

112. Crawford L, Wyatt M, Bryers J, Ratner B. Biocompatibility Evolves: Phenomenology to Toxicology to Regeneration. Adv Healthc Mater. 2021 Jun 1;10(11):e2002153.

113. Chan BP, Leong KW. Scaffolding in tissue engineering: general approaches and tissue-specific considerations. European Spine Journal. 2008 Dec;17(Suppl 4):467.

114. Saberianpour S, Heidarzadeh M, Geranmayeh MH, Hosseinkhani H, Rahbarghazi R, Nouri M. Tissue engineering strategies for the induction of angiogenesis using biomaterials. J Biol Eng. 2018 Dec 27;12(1).

115. Dixon DT, Gomillion CT. Conductive Scaffolds for Bone Tissue Engineering: Current State and Future Outlook. Journal of Functional Biomaterials 2022, Vol 13, Page 1. 2021 Dec 21;13(1):1.

116. Neves MI, Moroni L, Barrias CC. Modulating Alginate Hydrogels for Improved Biological Performance as Cellular 3D Microenvironments. Front Bioeng Biotechnol. 2020;8:665.

117. Parreidt TS, Müller K, Schmid M. Alginate-Based Edible Films and Coatings for Food Packaging Applications. Foods. 2018 Oct 1;7(10).

118. Ahmad Raus R, Wan Nawawi WMF, Nasaruddin RR. Alginate and alginate composites for biomedical applications. Asian J Pharm Sci. 2021 May 1;16(3):280–306.

119. Preetam S, Nahak BK, Patra S, Toncu DC, Park S, Syväjärvi M, et al. Emergence of microfluidics for next generation biomedical devices. Biosens Bioelectron X. 2022 May 1;10:100106.

120. Inamdar NK, Borenstein JT. Microfluidic cell culture models for tissue engineering. Curr Opin Biotechnol. 2011 Oct 1;22(5):681–9.

121. Zhang Y. Three-dimensional-printing for microfluidics or the other way around? Int J Bioprint. 2019;5(2):61–73.

122. Ji Z, Jiang D, Zhang X, Guo Y, Wang X, Ji Z, et al. Facile Photo and Thermal Two-Stage Curing for High-Performance 3D Printing of Poly(Dimethylsiloxane). Macromol Rapid Commun. 2020 May 1;41(10):2000064.

123. Duong VT. Twelve-day medium pumping into tubular cell-laden scaffold using a lab-made PDMS connector.

124. Niculescu AG, Chircov C, Bîrcă AC, Grumezescu AM. Fabrication and Applications of Microfluidic Devices: A Review. Int J Mol Sci. 2021 Feb 2;22(4):1–26.

125. Kjar A, McFarland B, Mecham K, Harward N, Huang Y. Engineering of tissue constructs using coaxial bioprinting. Bioact Mater. 2021 Feb 1;6(2):460–71.

126. Dai X, Liu L, Ouyang J, Li X, Zhang X, Lan Q, et al. Coaxial 3D bioprinting of self-assembled multicellular heterogeneous tumor fibers. Scientific Reports 2017 7:1. 2017 May 3;7(1):1–11.

127. Jia W, Gungor-Ozkerim PS, Zhang YS, Yue K, Zhu K, Liu W, et al. Direct 3D bioprinting of perfusable vascular constructs using a blend bioink. Biomaterials. 2016 Nov 1;106:58–68.

128. Liu W, Zhong Z, Hu N, Zhou Y, Maggio L, Miri AK, et al. Coaxial extrusion bioprinting of 3D microfibrous constructs with cell-favorable gelatin methacryloyl microenvironments. Biofabrication. 2018 Jan 12;10(2):024102.

129. Yu Y, Xie R, He Y, Zhao F, Zhang Q, Wang W, et al. Dual-core coaxial bioprinting of double-channel constructs with a potential for perfusion and interaction of cells. Biofabrication. 2022 May 26;14(3):035012.

130. Mao M, Liang H, He J, Kasimu A, Zhang Y, Wang L, et al. Coaxial Electrohydrodynamic Bioprinting of Pre-vascularized Cell-laden Constructs for Tissue Engineering. Int J Bioprint. 2021;7(3):1–11.

131. Gao G, Park JY, Kim BS, Jang J, Cho DW. Coaxial Cell Printing of Freestanding, Perfusable, and Functional In Vitro Vascular Models for Recapitulation of Native Vascular Endothelium Pathophysiology. Adv Healthc Mater. 2018 Dec 1;7(23):1801102.

132. Li F, Macdonald NP, Guijt RM, Breadmore MC. Using Printing Orientation for Tuning Fluidic Behavior in Microfluidic Chips Made by Fused Deposition Modeling 3D Printing. Anal Chem. 2017 Dec 5;89(23):12805–11.

133. O'Connor C, Brady E, Zheng Y, Moore E, Stevens KR. Engineering the multiscale complexity of vascular networks. Nature Reviews Materials 2022 7:9. 2022 May 31;7(9):702–16.

134. Schindelin J, Arganda-Carreras I, Frise E, Kaynig V, Longair M, Pietzsch T, et al. Fiji: an open-source platform for biological-image analysis. Nature Methods 2012 9:7. 2012 Jun 28;9(7):676–82.

135. Samuel R, Daheron L, Liao S, Vardam T, Kamoun WS, Batista A, et al. Generation of functionally competent and durable engineered blood vessels from human induced pluripotent stem cells. Proc Natl Acad Sci U S A. 2013 Jul 30;110(31):12774–9.

136. Shi J, Wei F, Chouraki B, Sun X, Wei J, Zhu L. Study on Performance Simulation of Vascular-like Flow Channel Model Based on TPMS Structure. Biomimetics. 2023 Mar 1;8(1).

137. Tfelt-Hansen J, Brown EM. THE CALCIUM-SENSING RECEPTOR IN NORMAL PHYSIOLOGY AND PATHOPHYSIOLOGY: A Review. Crit Rev Clin Lab Sci. 2005 Jan;42(1):35–70.

138. Tanaka T, Matsushita T, Nishida K, Takayama K, Nagai K, Araki D, et al. Attenuation of osteoarthritis progression in mice following intra-articular administration of simvastatin-conjugated gelatin hydrogel. J Tissue Eng Regen Med. 2019 Mar 1;13(3):423–32.

139. Wang X, Ao Q, Tian X, Fan J, Tong H, Hou W, et al. Gelatin-Based Hydrogels for Organ 3D Bioprinting. Polymers (Basel). 2017 Aug 30;9(9).

140. Zhou X, Gao Q, Yu D, Shao Y, Wang Z, Liu X, et al. 3D-bioprinted vascular scaffold with tunable mechanical properties for simulating and promoting neo-vascularization. Smart Mater Med. 2022 Jan 1;3:199–208.

141. Ketabat F, Maris T, Duan X, Yazdanpanah Z, Kelly ME, Badea I, et al. Optimization of 3D printing and in vitro characterization of alginate/gelatin lattice and angular scaffolds for potential cardiac tissue engineering. Front Bioeng Biotechnol. 2023 May 25;11:1161804.

142. Wang QQ, Liu Y, Zhang CJ, Zhang C, Zhu P. Alginate/gelatin blended hydrogel fibers cross-linked by Ca2+ and oxidized starch: Preparation and properties. Materials Science and Engineering: C. 2019 Jun 1;99:1469–76.

143. Du J, Hu X, Su Y, Wei T, Jiao Z, Liu T, et al. Gelatin/sodium alginate hydrogel-coated decellularized porcine coronary artery to construct bilayer tissue engineered blood vessels. Int J Biol Macromol. 2022;209:2070–83.

144. Hu C, Sun H, Liu Z, Chen Y, Chen Y, Wu H, et al. Freestanding 3-D microvascular networks made of alginate hydrogel as a universal tool to create microchannels inside hydrogels. Biomicrofluidics. 2016 Jul 1;10(4).

145. Chen AI, Balter ML, Chen MI, Gross D, Alam SK, Maguire TJ, et al. Multilayered tissue mimicking skin and vessel phantoms with tunable mechanical, optical, and acoustic properties. Med Phys. 2016 Jun 1;43(6Part1):3117–31.

146. Sonaye SY, Ertugral EG, Kothapalli CR, Sikder P. Extrusion 3D (Bio)Printing of Alginate-Gelatin-Based Composite Scaffolds for Skeletal Muscle Tissue Engineering. Materials 2022, Vol 15, Page 7945. 2022 Nov 10;15(22):7945.

147. Ahmadi Soufivand A, Faber J, Hinrichsen J, Budday S. Multilayer 3D bioprinting and complex mechanical properties of alginate-gelatin mesostructures. Scientific Reports 2023 13:1. 2023 Jul 12;13(1):1–14.

148. Lee VK, Kim DY, Ngo H, Lee Y, Seo L, Yoo SS, et al. Creating Perfused Functional Vascular Channels Using 3D Bio-Printing Technology. Biomaterials. 2014;35(28):8092.

149. Medicines Containing or Derived from Animal Products Background. Dorset County Hospital NHS Foundation Trust. 2020.

150. Uddin SMK, Hossain MAM, Sagadevan S, Al Amin M, Johan MR. Halal and Kosher gelatin: Applications as well as detection approaches with challenges and prospects. Food Biosci. 2021 Dec 1;44:101422.

151. Herdiana Y, Ferdiansyah Sofian F, Shamsuddin S, Rusdiana T. Towards halal pharmaceutical: Exploring alternatives to animal-based ingredients. Heliyon. 2024;10:e23624.

152. Lan D, Shang Y, Su H, Liang M, Liu Y, Li H, et al. Facile Fabrication of Hollow Hydrogel Microfiber via 3D Printing-Assisted Microfluidics and Its Application as a Biomimetic Blood Capillary. ACS Biomater Sci Eng. 2021 Oct 11;7(10):4971–81.

153. Bosch-Rué E, Delgado LM, Javier Gil F, Perez RA. Direct extrusion of individually encapsulated endothelial and smooth muscle cells mimicking blood vessel structures and vascular native cell alignment. Biofabrication. 2020 Oct 16;13(1):015003.

154. Xu P, Xie R, Liu Y, Luo G, Ding M, Liang Q, et al. Bioinspired Microfibers with Embedded Perfusable Helical Channels. Advanced Materials. 2017 Sep 1;29(34):1701664.

155. Yu Y, Fu F, Shang L, Cheng Y, Gu Z, Zhao Y, et al. Bioinspired Helical Microfibers from Microfluidics. Advanced Materials. 2017;29(18):1605765.

156. Nilsson DPG, Holmgren M, Holmlund P, Wåhlin A, Eklund A, Dahlberg T, et al. Patient-specific brain arteries molded as a flexible phantom model using 3D printed water-soluble resin. Scientific Reports 2022 12:1. 2022 Jun 17;12(1):1–9.

157. Massa S, Sakr MA, Seo J, Bandaru P, Arneri A, Bersini S, et al. Bioprinted 3D vascularized tissue model for drug toxicity analysis. Biomicrofluidics. 2017 Jul 1;11(4).

158. Yoshida K, Onoe H. Functionalized core-shell hydrogel microsprings by anisotropic gelation with bevel-tip capillary. Scientific Reports 2017 7:1. 2017 Apr 5;7(1):1–9.

159. Tsai CHD, Lin XY. Experimental Study on Microfluidic Mixing with Different Zigzag Angles. Micromachines 2019, Vol 10, Page 583. 2019 Aug 31;10(9):583.

160. Bennacef C, Desobry S, Jasniewski J, Leclerc S, Probst L, Desobry-Banon S. Influence of Alginate Properties and Calcium Chloride Concentration on Alginate Bead Reticulation and Size: A Phenomenological Approach. Polymers (Basel). 2023 Oct 1;15(20).

161. Rasheed A, Azizi L, Turkki P, Janka M, Hytönen VP, Tuukkanen S. Extrusion-based bioprinting of multilayered nanocellulose constructs for cell cultivation using in situ freezing and preprint CaCl2 cross-linking. ACS Omega. 2021;6(1):569–78.

162. Lai TY, Cao J, Ou-Yang P, Tsai CY, Lin CW, Chen CC, et al. Different methods of detaching adherent cells and their effects on the cell surface expression of Fas receptor and Fas ligand. Scientific Reports 2022 12:1. 2022 Apr 5;12(1):1–8.

163. Calcium in Cell Culture [Internet]. [cited 2024 Mar 27]. Available from: https://www.sigmaaldrich.com/GB/en/technical-documents/technical-article/cell-culture-and-cell-culture-analysis/mammalian-cell-culture/calcium-in-cell-culture

164. ISO 10993-5:2009 - Biological evaluation of medical devices — Part 5: Tests for in vitro cytotoxicity [Internet]. [cited 2024 Mar 27]. Available from: https://www.iso.org/standard/36406.html

165. Caliari SR, Burdick JA. A practical guide to hydrogels for cell culture. Nature Methods 2016 13:5. 2016 Apr 28;13(5):405–14.

166. Andersen T, Auk-Emblem P, Dornish M. 3D Cell Culture in Alginate Hydrogels. Microarrays. 2015 Mar 24;4(2):133.

167. Mehdizadeh Omrani M, Kumar H, Mohamed MGA, Golovin K, S. Milani A, Hadjizadeh A, et al. Polyether ether ketone surface modification with plasma and gelatin for enhancing cell attachment. J Biomed Mater Res B Appl Biomater. 2021 May 1;109(5):622–9.

168. Andersen T, Markussen C, Dornish M, Heier-Baardson H, Melvik JE, Alsberg E, et al. In Situ Gelation for Cell Immobilization and Culture in Alginate Foam Scaffolds. Tissue Eng Part A. 2014 Feb 2;20(3–4):600.

169. Weng YJ, Ren JR, Huang N, Wang J, Chen JY, Leng YX, et al. Surface engineering of Ti–O films by photochemical immobilization of gelatin. Materials Science and Engineering: C. 2008 Dec 1;28(8):1495–500.

170. ReadyProbes Cell Viability Imaging Kit, Blue/Green | Thermo Fisher Scientific - UK [Internet]. [cited 2024 Oct 22]. Available from: https://www.thermofisher.com/uk/en/home/references/protocols/cell-and-tissue-analysis/protocols/readyprobes-cell-viability-imaging-kit-blue-green.html

171. Eslami Amirabadi H, SahebAli S, Frimat JP, Luttge R, den Toonder JMJ. A novel method to understand tumor cell invasion: integrating extracellular matrix mimicking layers in microfluidic chips by “selective curing.” Biomed Microdevices. 2017 Dec 1;19(4):1–11.

172. Pezeshki-Modaress M, Zandi M, Rajabi S. Tailoring the gelatin/chitosan electrospun scaffold for application in skin tissue engineering: an in vitro study. Prog Biomater. 2018 Sep 1;7(3):207–18.

173. Scholz B, Kinzelmann C, Benz K, Mollenhauer J, Wurst H, Schlosshauer B. Suppression of adverse angiogenesis in an albumin-based hydrogel for articular cartilage and intervertebral disc regeneration. Eur Cell Mater. 2010;20:24–37.

174. Tang-Quan KR, Xi Y, Hochman-Mendez C, Xiang Q, Lee PF, Sampaio LC, et al. Gelatin Promotes Cell Retention Within Decellularized Heart Extracellular Matrix Vasculature and Parenchyma. Cell Mol Bioeng. 2020 Dec 1;13(6):633.

175. Li S, Wang K, Jiang X, Hu Q, Zhang C, Wang B. Rapid Fabrication of Ready-to-Use Gelatin Scaffolds with Prevascular Networks Using Alginate Hollow Fibers as Sacrificial Templates. ACS Biomater Sci Eng. 2020 Apr 13;6(4):2297–311.

176. Kogler S, Aizenshtadt A, Harrison S, Skottvoll FS, Berg HE, Abadpour S, et al. “organ-in-a-Column” Coupled On-line with Liquid Chromatography-Mass Spectrometry. Anal Chem. 2022 Dec 20;94(50):17677–84.

177. Behroodi E, Latifi H, Bagheri Z, Ermis E, Roshani S, Salehi Moghaddam M. A combined 3D printing/CNC micro-milling method to fabricate a large-scale microfluidic device with the small size 3D architectures: an application for tumor spheroid production. Scientific Reports 2020 10:1. 2020 Dec 17;10(1):1–14.

178. Fan R, Piou M, Darling E, Cormier D, Sun J, Wan J. Bio-printing cell-laden Matrigel–agarose constructs. J Biomater Appl. 2016 Nov 1;31(5):684.

179. Thermo Fisher Scientific. CellMask Green Actin Tracking Stain 1 x 60 Assays:Cell Analysis Products, | Fisher Scientific.

180. Fannon OM, Bithell A, Whalley BJ, Delivopoulos E. A Fiber Alginate Co-culture Platform for the Differentiation of mESC and Modeling of the Neural Tube. Front Neurosci. 2021 Jan 12;14.

181. Rowley JA, Madlambayan G, Mooney DJ. Alginate hydrogels as synthetic extracellular matrix materials. Biomaterials. 1999 Jan;20(1):45–53.

182. Pries AR, Reglin B, Secomb TW. Remodeling of Blood Vessels. Hypertension. 2005 Oct 1;46(4):725–31.

183. Dulbecco s Modified Eagle s Medium - high glucose (DMEM-High) without Sodium pyruvate sterile-filtered [Internet]. [cited 2024 Mar 13]. Available from: https://www.sigmaaldrich.com/GB/en/product/sigma/d5796

184. Schnellbaecher A, Lindig A, Le Mignon M, Hofmann T, Pardon B, Bellmaine S, et al. Degradation products of tryptophan in cell culture media: Contribution to color and toxicity. Int J Mol Sci. 2021 Jun 2;22(12):6221.

185. Lee KY, Mooney DJ. Alginate: Properties and biomedical applications. Prog Polym Sci. 2012 Jan 1;37(1):106–26.

186. Golunova A, Velychkivska N, Mikšovská Z, Chochola V, Jaroš J, Hampl A, et al. Direct and Indirect Biomimetic Peptide Modification of Alginate: Efficiency, Side Reactions, and Cell Response. International Journal of Molecular Sciences 2021, Vol 22, Page 5731. 2021 May 27;22(11):5731.

187. Vacharathit V, Silva EA, Mooney DJ. Viability and functionality of cells delivered from peptide conjugated scaffolds. Biomaterials. 2011 May 1;32(15):3721–8.

188. Ye H, Xia Z, Ferguson DJP, Triffitt JT, Cui Z. Studies on the use of hollow fibre membrane bioreactors for tissue generation by using rat bone marrow fibroblastic cells and a composite scaffold. J Mater Sci Mater Med. 2007 Apr;18(4):641–8.

189. Mercado-Pagán ÁE, Kang Y, Findlay MW, Yang Y. Development and evaluation of elastomeric hollow fiber membranes as small diameter vascular graft substitutes. Materials Science and Engineering: C. 2015 Apr 1;49:541–8.

190. Maleki S, Shamloo A, Kalantarnia F. Tubular TPU/SF nanofibers covered with chitosan-based hydrogels as small-diameter vascular grafts with enhanced mechanical properties. Scientific Reports 2022 12:1. 2022 Apr 13;12(1):1–15.

191. Francisco P, Neves Amaral M, Neves A, Ferreira-Gonçalves T, Viana AS, Catarino J, et al. Pluronic® F127 Hydrogel Containing Silver Nanoparticles in Skin Burn Regeneration: An Experimental Approach from Fundamental to Translational Research. Gels 2023, Vol 9, Page 200. 2023 Mar 6;9(3):200.

192. sticky-Slide I Luer | Self-Adhesive Underside | ibidi [Internet]. [cited 2024 Mar 25]. Available from: https://ibidi.com/sticky-slides/63-sticky-slide-i-luer.html

193. Liu Y, Li K, Tian J, Gao A, Tian L, Su H, et al. Synthesis of robust underwater glues from common proteins via unfolding-aggregating strategy. Nature Communications 2023 14:1. 2023 Aug 24;14(1):1–15.

194. Takei T, Kitazono Z, Ozuno Y, Yoshinaga T, Nishimata H, Yoshida M. Vascular-like network prepared using hollow hydrogel microfibers. J Biosci Bioeng. 2016 Mar 1;121(3):336–40.

195. Satoh T, Narazaki G, Sugita R, Kobayashi H, Sugiura S, Kanamori T. A pneumatic pressure-driven multi-throughput microfluidic circulation culture system. Lab Chip. 2016 Jun 7;16(12):2339–48.

196. Tocchio A, Tamplenizza M, Martello F, Gerges I, Rossi E, Argentiere S, et al. Versatile fabrication of vascularizable scaffolds for large tissue engineering in bioreactor. 2015;

8. Appendices

Appendix A:

Measuring the width of fibre's shell and core using Fiji Software:

In the software, scale was set up by measuring the distance in pixels (448.9375) for the known scale of 500 µm (distance: 500) already present on the image. This information along with the unit of length (µm) was put into the 'Set scale' tool (under Analyze) in the Fiji software, and 'Global' was selected. This resulted in a Scale of 0.8979 pixels/µm, which was used in measurements for all of the images acquired through the Carl Zeiss Primo Star microscope.

In an open image file, straight segmented or freehand lines from the Fiji software were used to draw a line across the diameter of the fibre. Then on a keyboard, Command+M (on a macOS device) or Ctrl+M (on a Windows device) keys were pressed simultaneously to measure the length of the segmented line. This step was repeated five times in multiple locations on a fibre. From the 'Results' pop-up window, Length data were saved and processed.

Appendix B:

Automated Fiji macro used for counting the number of green and red labelled cells for viability calculations.

For Green channel:

// Clear any previous selections and images

```
run("Close All");
```

```
setBatchMode(true);


Dialog.create("Cell Viability Checker");
        Dialog.addMessage(" This macro processes fluorescence images of cells to count the number of green cells in each image. \n First put your image(s) to be processed in a separate input folder. ");
        Dialog.addString("Add image file type suffix: ", ".tif", 5);
        Dialog.addMessage("Click OK to choose your input and output directories. \n After processing you will be able to save the the number of green cells in each image.");
Dialog.show();
suffix = Dialog.getString();


input = getDirectory("Input directory");
output = getDirectory("Output directory");


processFolder(input);


function processFolder(input) {
        list = getFileList(input);
        for (i = 0; i < list.length; i++) {
                if(File.isDirectory(input + list[i]))
                        processFolder("" + input + list[i]);
```

```
                if(endsWith(list[i], suffix))
                        processFile(input, output, list[i]);
        }
}

function processFile(input, output, file) {
open(input + File.separator + file);

//renames channels to generic names that the code can understand
title = getTitle();
run("Enhance Contrast", "saturated=0.35");
run("RGB Color");
rename("Image");
run("Split Channels");
selectWindow("Image (red)");
rename("red");
selectWindow("Image (green)");
rename("green");
//closes blue channel
selectWindow("Image (blue)");
close();

selectWindow("green");
```

```
run("3D Objects Counter", "threshold=35 slice=1 min.=4 max.=262144
exclude_objects_on_edges centres_of_masses summary");


 //macro "Close All Windows" {
     while (nImages>0) {
         selectImage(nImages);
         close();
     }
 }
```

For Red channel:

```
//Clear any previous selections and images
run("Close All");


setBatchMode(true);


Dialog.create("Cell Viability Checker");
        Dialog.addMessage(" This macro processes fluorescence images of cells to count the number of red cells in each image. \n \n First put your image(s) to be processed in a separate input folder. ");
        Dialog.addString("Add image file type suffix: ", ".tif", 5);
        Dialog.addMessage("Click OK to choose your input and output directories. \n After processing you will be able to save the log file containing the number of red cells in each image.");
Dialog.show();
```

```
suffix = Dialog.getString();


input = getDirectory("Input directory");
output = getDirectory("Output directory");

processFolder(input);

function processFolder(input) {
	list = getFileList(input);
	for (i = 0; i < list.length; i++) {
		if(File.isDirectory(input + list[i]))
			processFolder("" + input + list[i]);
		if(endsWith(list[i], suffix))
			processFile(input, output, list[i]);
	}
}


function processFile(input, output, file) {
open(input + File.separator + file);

//renames channels to generic names that the code can understand
```

```
title = getTitle();
run("Enhance Contrast", "saturated=0.35");
run("RGB Color");
rename("Image");
run("Split Channels");
selectWindow("Image (red)");
rename("red");
selectWindow("Image (green)");
rename("green");
//closes blue channel
selectWindow("Image (blue)");
close();



selectWindow("red");
//value between 1.5 and 5 depending on the quality of image
run("Gamma...", "value=5");
//radius between 0.05 and 1 depending on the quality of image
run("Median...", "radius=0.25");


run("3D Objects Counter", "threshold=34 slice=1 min.=4 max.=262144
exclude_objects_on_edges centres_of_masses summary");


 //macro "Close All Windows" {
```

```
    while (nImages>0) {
        selectImage(nImages);
        close();
    }
}
```

Appendix C:

Automated Fiji macro used for measuring the area of cells on florescent confocal images.

```
// Clear any previous selections and images
run("Close All");

path = File.openDialog("Select a File");
  //open(path); // open the file
  dir = File.getParent(path);
  name = File.getName(path);
  print("Path:", path);
  print("Name:", name);

  list = getFileList(dir);
```

```
open(path);

//renames channels to generic names that the code can understand
title = getTitle();

run("RGB Color");
rename("Image");
run("Split Channels");
selectWindow("Image (red)");
rename("red");
selectWindow("Image (green)");
rename("green");
//closes blue channel
selectWindow("Image (blue)");
close();

selectWindow("green");

setAutoThreshold("Default dark no-reset");
//Adjust threshold to cover most of the cells.
waitForUser
```

```
run("Convert to Mask");

run("Watershed");

run("Analyze Particles...", "  show=[Count Masks] display exclude include summarize
overlay composite");
```

Appendix D:

Live and dead cells in solid alginate-only fibres (24 hours culture), before (i) and after (ii) washing with water, following bathing in 10 wt% $CaCl_2$ bath.

